

UNIVERSITY OF OKLAHOMA  
GRADUATE COLLEGE

A DISLOCATION-BASED BOUNDARY ELEMENT METHOD TO  
MODEL PRESSURIZED FRACTURES

A THESIS

SUBMITTED TO THE GRADUATE FACULTY

in partial fulfillment of the requirements for the

Degree of

MASTER OF SCIENCE

By

FARZIN PAKNIA  
Norman, Oklahoma  
2019

A DISLOCATION-BASED BOUNDARY ELEMENT METHOD TO  
MODEL PRESSURIZED FRACTURES

A THESIS APPROVED FOR THE  
MEWBOURNE SCHOOL OF PETROLEUM AND GEOLOGICAL  
ENGINEERING

BY THE COMMITTEE CONSISTING OF

Dr. Ahmad Ghassemi, Chair

Dr. Xingru Wu

Dr. Mashhad Fahes



## **DEDICATION**

First of all, I would like to devote this little work to the United States of America for granting my family and I an opportunity to choose it as our new home and to begin a new chapter in our life. I, also, would like to dedicate this thesis to my beloved wife, Maryam. Her heart-warming advices have had tremendous influence on me during ups and downs of this long way to tackle hardships and discouragements. And would like to dedicate this thesis to my wonderful son, Radvin, whose presence next to me during sleepless nights was so comforting. And my mother, Zahedeh, whose persuasions was so motivating. Her financial supports were so much for me. Finally, I would like to appreciate some other people for knowing that my perseverance is untouchable!

## ACKNOWLEDGEMENTS

First off, I would like to express my special sincere gratitude to my advisor Dr. Ahmad Ghassemi for his continuous support of my research to fulfill my program. My research topic is one-of-a-kind in its subject and picking this topic could be impossible for me alone. His advices have been so motivating to me to overcome difficulties of getting the research done. Also, his guidance, patience and enthusiasm have been so influential that I could not have envisaged of having a better advisor and mentor. It needs to be mentioned that my former advisor Dr. Maysam PourNik and his guidance was so influential in the beginning of study program. I am and will be so grateful of him for his inspirational advices.

In addition to my advisor, I would like to appreciate committee members Dr. Xingru Wu and Dr. Mashhad Fahes for invaluable suggestions and comments to improve the context of thesis.

Furthermore, I would like to recognize and thank the Mewbourne School of Petroleum and Geological Engineering staff for their worthwhile assistance and support.

And Finally, I would like to mention my friends Jianrong Lu and Qian Gao for suggesting me helpful materials such as research papers and relevant past-defended theses and dissertations.

## TABLE OF CONTENTS

<b>DEDICATION .....</b>	<b>iv</b>
<b>ACKNOWLEDGEMENTS .....</b>	<b>v</b>
<b>TABLE OF CONTENTS .....</b>	<b>vi</b>
<b>LIST OF TABLES .....</b>	<b>x</b>
<b>LIST OF FIGURES .....</b>	<b>xii</b>
<b>ABSTRACT .....</b>	<b>xviii</b>
<b>CHAPTER 1. Introduction .....</b>	<b>1</b>
1.1. Motivation, Problem Statement and Objectives .....	4
1.1.1. Okada Solution.....	5
1.2. Thesis Organization .....	6
<b>CHAPTER 2. Theory of Dislocation .....</b>	<b>8</b>
2.1. Description of Okada Solution.....	11
2.2. Kinematic Equations for the Case of Finite Rectangular Source .....	16
2.3. The Case of Multiple Discontinuities in an Elastic Half-Space Medium .....	24
2.4. Model Development.....	24
2.5. Locus of Singularities .....	26
<b>CHAPTER 3. Boundary Element Procedure to Model and Simulate a Hydraulic Fracture.....</b>	<b>27</b>

<b>3.1. Two-Dimensional Elastic Plane-Strain Problem (Katsikadelis 2016)</b> .....	27
<b>3.1.1. Transformation to a Boundary Integral Equation (Katsikadelis 2016; Youn 1993)</b> .....	30
<b>3.1.1.1. Displacement Field Components due to a Unit Concentrated Force</b> ..	32
<b>3.1.1.2. Stress Field components Due to a Unit Concentrated Force</b> .....	33
<b>3.1.1.3. Boundary Traction components Due to a Unit Concentrated Force</b> ..	34
<b>3.1.1.4. Final Step to express Integral form of the Solution</b> .....	35
<b>3.1.1.5. Integral Equations of the Stress Components</b> .....	37
<b>3.1.2. Discretization of the Boundary Integral Equations</b> .....	38
<b>3.1.3. Calculation of displacement Field Components at Interior Field Points</b> ...	40
<b>3.1.4. Calculation of Stress Components at Interior Field Points</b> .....	41
<b>3.1.5. Converting domain integrals to boundary integrals</b> .....	41
<b>3.2. Boundary Element Method Based on Okada Formulation</b> .....	42
<b>3.2.1. Philosophy of the Method</b> .....	43
<b>3.2.2. Description of the Method</b> .....	44
<b>3.2.3. Representation of System of Equilibrium Equation</b> .....	46
<b>3.2.4. Analysis of Displacement and Displacement Derivative Fields</b> .....	50
<b>3.2.5. Analysis of Strain and Stress</b> .....	50
<b>3.2.6. Analysis of Principal Strains, Principal Stresses, and their directions</b> .....	50
<b>3.2.7. Analysis of Maximum Shearing Strain and Stress and their corresponding directions</b> .....	51

3.3. Comparison of the classical BEM to Our Proposed BEM.....	52
<b>CHAPTER 4. Implementation of the BEM in a Computer Code .....</b>	<b>55</b>
4.1. Discretization of a Fracture.....	55
4.2. Generation of Field Points in a HF Domain .....	57
4.3. Comparison of the Method and Finite Element Method .....	61
4.4. Verification of the Method.....	62
4.5. Comparison with Okada Example (Okada 1992) .....	63
4.6. Verification by Fialko’s Solution.....	65
4.7. Verification by Pollard Solution .....	67
4.8. Verification of Displacement Derivatives .....	78
<b>CHAPTER 5. Conclusion and Recommendations.....</b>	<b>84</b>
5.1. Conclusion	84
5.2. Findings During Simulator Development.....	86
5.3. Some Recommendations for Future Developments .....	87
<b>Nomenclature (English).....</b>	<b>88</b>
<b>Nomenclature (Greek).....</b>	<b>89</b>
<b>Abbreviations .....</b>	<b>90</b>
<b>References .....</b>	<b>92</b>
<b>Appendix A: Explanation of Parameters and Variables Involved in Equations Which Are Given in Table 2.3 to Table 2.6.....</b>	<b>96</b>



<b>Appendix B: Capabilities of HiFrac 3D .....</b>	<b>101</b>
<b>B.1. Discretization of Fracture(s) .....</b>	<b>101</b>
<b>B.2. Grid Generation in the Model Domain .....</b>	<b>102</b>
<b>B.3. Analysis of Dislocations .....</b>	<b>102</b>
<b>B.4. Analysis of Displacement/Displacement Derivative Fields.....</b>	<b>102</b>
<b>B.5. Strain and Stress Analysis .....</b>	<b>103</b>
<b>B.6. Principal Strains, Principal Stresses, and Maximum Shear Strain/Stress .....</b>	<b>103</b>
<b>B.7. Use of Tools .....</b>	<b>103</b>
<b>B.8. An Example of a Single-Fracture Model.....</b>	<b>105</b>
<b>B.9. An Example of a Multiple Hydraulic Fractures in Two Separate Stages.....</b>	<b>113</b>

## LIST OF TABLES

Table 1.1—Characteristics of Some Traditional HF Models (Xiang 2011).....	2
Table 2.1—Brief History of Published Closed Form Analytical Solutions for the Case of <b>Point Source</b> .....	12
Table 2.2—Brief History of Published Closed Form Analytical Solutions for the Case of <b>Finite Rectangular Source</b> .....	12
Table 2.3—All required functions to analyze displacement field components due to a rectangular source dislocation in a half-space (Okada-1992, with some modifications).....	17
Table 2.4—All required functions to analyze $x_1$ -derivative of displacement field components due to a rectangular source dislocation in a half-space (Okada- 1992, with some modifications) .....	18
Table 2.5—All required functions to analyze $x_2$ -derivative of displacement field components due to a rectangular source dislocation in a half-space (Okada- 1992, with some modifications) .....	19
Table 2.6—All required functions to analyze $x_3$ -derivative of displacement field components due to a rectangular source dislocation in a half-space (Okada- 1992, with some modifications) .....	20
Table 2.7—Input Variables and Their Descriptions .....	25

Table 4.1—Fault Specification in Okada (1992).....	64
Table 4.2— Initial Values and Properties Simulate Pollard-Fu Problem.....	69
Table 4.3— General Information About a Single-Fracture Pollard’s Solution Model - Case 1: Mesh Size $35 \times 5$ .....	75
Table 4.4— General Information About a Single-Fracture Pollard-Fu Model - Case 2: Mesh Size $105 \times 15$ .....	75
Table 4.5— Initial Values and Properties for a Single-Stage Multi-HF Model .....	79
Table B. 1— Initial Values and Properties for a Single HF Model.....	105
Table B. 2— General Information About a Single-Fracture Model.....	112
Table B. 3— Initial Values and Properties for a Two-Stage Multi-HF Model .....	114
Table B. 4— General Information About a Two-Stage Multi-Fracture Model.....	122

## LIST OF FIGURES

Figure 1.1—A Schematic of Hydraulic Fracturing Development in a Gas Shale Reservoir (Hussain et al. 2017).....	1
Figure 2.1—A Discontinuous Source in an Elastic Medium.....	9
Figure 2.2—A Schematic of a Cartesian frame containing an Observation Point, a Point Force, and an Imagery Point Force.....	13
Figure 2.3—A rectangular source with three types of dislocations. Any dislocation at this source can be decomposed to these three dislocation types. ....	14
Figure 2.4—Side view of A finite rectangular source with its image pair. Axes $x_1$ , $\xi$ , and $\xi'$ are perpendicular to the page. Axes $x_1$ and $\xi'$ are outward, but axis $\xi$ at observation point is inward. ....	16
Figure 2.5—Input Variables to Define RABE. Parameters $iAW_1$ and $iAW_2$ are measured Assuming $iDip = 0^\circ$ . ....	25
Figure 3.1—A Schematic of a 2D Elastic Body Subjected to a Force $\mathbf{F}$ Exerted at Point $Q$ .....	28
Figure 3.2—Workflow of the BEM Simulation .....	46
Figure 3.3—A Schematic of a discretized HF. In this figure, $m$ th RABE undergoes a unit TL dislocation. It generates stress in the same RABE and $n$ th RABE.....	47
Figure 3.4—Comparison of Boundary Element Shapes.....	53

Figure 4.1—Radial and Sequential BE Mesh Generation in a Penny-Shaped Fracture...	55
Figure 4.2—Radial and Sequential BE Mesh Generation in a Rectangular Fracture.....	57
Figure 4.3—An Example of a $15 \times 15$ Penny-Shaped Fracture and its corresponding grid of field-points. Upper-Left is Top View, Upper-Right is Side View, and the Lower One is Front View. Grid Spacing Outside of the Fracture is Uniform.	58
Figure 4.4—The Same $15 \times 15$ Penny-Shaped Fracture and its corresponding grid of field-points. Grid Spacing Outside of the Fracture Varies Exponential/Logarithmic.....	59
Figure 4.5—A $15 \times 3$ Rectangular Fracture and its corresponding grid of field-points. Grid Spacing Outside of the Fracture is uniform for Top Figure and Exponential/ Logarithmic for Bottom Figure. and Validation of the Method	60
Figure 4.6—A Schematic of Stiffness Matrices Obtained from FEM and BEM. ....	62
Figure 4.7—Comparison of Field Measurements and Model Results.....	64
Figure 4.8—A Cross-Sectional View of a Penny-Shaped Horizontal Fracture in an Elastic Half-Space (Fialko et al. 2001) .....	65
Figure 4.9—Left side shows our horizontal circular fracture at depth 1.2 and radius 1.0. Right side shows Horizontal Displacement Field at Free Surface of an Elastic Half-space.....	66
Figure 4.10—Vertical Displacement Field at Free Surface of an Elastic Half-space .....	67

Figure 4.11—A Rectangular Fracture in a Linear Elastic Half-Space. Axes  $x_1$  and  $x$  Are Perpendicular to Fracture Surface. Fracture Length along  $x$ -Axis Is Long Enough to Simulate a 2D Plane-Strain Problem. ....68

Figure 4.12—Geometry of the Simulation Model for Case 1. Mesh Size is  $35 \times 5$  and  $\beta = 0^\circ$  .....70

Figure 4.13—Geometry of the Simulation Model for Case 2. Mesh Size is  $105 \times 15$  and  $\beta = 0^\circ$  .....70

Figure 4.14—Geometry of the Simulation Model for Case 1. Mesh Size is  $35 \times 5$  and  $\beta = 90^\circ$  .....71

Figure 4.15—Geometry of the Simulation Model for Case 2. Mesh Size is  $105 \times 15$  and  $\beta = 90^\circ$  .....71

Figure 4.16—Comparison of Normalized Vertical Displacement  $u_3$  Results at Horizontal Free Surface, Obtained from HiFrac 3D to Those of Fu-2014 and Pollard-1979. Black Curves Are Corresponding to Case 1 with the Mesh size of  $35 \times 5$  .....72

Figure 4.17—Comparison of Normalized Horizontal Stress  $\sigma_{22}$  Results Near Horizontal Free Surface, Obtained from HiFrac 3D to Those of Pollard-1979. Black Curves Are Corresponding to Case 1 with the Mesh size of  $35 \times 5$ . .....72

Figure 4.18—Comparison of Normalized Vertical Displacement  $u_3$  Results at Horizontal Free Surface, Obtained from HiFrac 3D to Those of Fu-2014 and Pollard-1979. Black Curves Are Corresponding to Case 2 with the Mesh size of  $105 \times 15$  .....73

Figure 4.19—Comparison of Normalized Horizontal Stress  $\sigma_{22}$  Results Near Horizontal Free Surface, Obtained from HiFrac 3D to Those of Pollard-1979. Black Curves Are Corresponding to Case 2 with the Mesh size of  $105 \times 15$ . .....74

Figure 4.20—Comparison of Vertical Displacement  $u_3$  Results at Horizontal Free Surface, Obtained from HiFrac 3D (Left) to That of Huang-2015 (Right). Dip Angle is  $0^\circ$  and Mesh size is  $105 \times 15$  .....76

Figure 4.21—Comparison of Vertical Stress  $\sigma_{33}$  Results Near Horizontal Free Surface, Obtained from HiFrac 3D (Left) to That of Huang-2015 (Right). Dip Angle is  $0^\circ$  and Mesh size is  $105 \times 15$  .....76

Figure 4.22—Comparison of Vertical Displacement  $u_3$  Results at Horizontal Free Surface, Obtained from HiFrac 3D (Left) to That of Huang-2015 (Right). Dip Angle is  $90^\circ$  and Mesh size is  $105 \times 15$ . .....77

Figure 4.23—Comparison of Vertical Stress  $\sigma_{33}$  Results Near Horizontal Free Surface, Obtained from HiFrac 3D (Left) to That of Huang-2015 (Right). Dip Angle is  $90^\circ$  and Mesh size is  $105 \times 15$ . .....77

Figure 4.24— 3D (Left) and Top (Right) View Geometries of an Arbitrary Multi-Cluster Hydraulic Fracture After Fluid Injection.....80

Figure 4.25— Gradient Vectors of Displacement Field Component  $u_1$  .....80

Figure 4.26— Gradient Vectors of Displacement Field Component  $u_2$  .....81

Figure 4.27— Gradient Vectors of Displacement Field Component  $u_3$  .....82

Figure A. 1—Side view of A finite rectangular source with its image pair. Axes $x_1$ , $\xi$ , and $\xi'$ are perpendicular to the page. Axes $x_1$ and $\xi'$ are outward, but axis $\xi$ at observation point is inward. ....	96
Figure B. 1—Geometry of the Fracture After Fluid Injection.....	106
Figure B. 2—Displacement Field $u_1$ in Model Domain and Its Gradient .....	106
Figure B. 3—Displacement Field $u_2$ in Model Domain and Its Gradient .....	106
Figure B. 4—Displacement Field $u_3$ in Model Domain and Its Gradient .....	107
Figure B. 5— Normal Stress Field $\sigma_{11}$ in Model Domain .....	107
Figure B. 6— Normal Stress Field $\sigma_{22}$ in Model Domain.....	107
Figure B. 7—Normal Stress Field $\sigma_{33}$ in Model Domain .....	108
Figure B. 8—Shear Stress Fields $\sigma_{12}$ , $\sigma_{23}$ in Model Domain .....	108
Figure B. 9—Shear Stress Fields $\sigma_{13}$ in Model Domain.....	109
Figure B. 10—Principal Stress Field $\sigma_{p1}$ in Model Domain.....	109
Figure B. 11—Principal Stress Field $\sigma_{p2}$ in Model Domain.....	110
Figure B. 12—Principal Stress Field $\sigma_{p3}$ in Model Domain.....	110
Figure B. 13—Maximum Shearing Stress Field $\tau_{Max}$ in Model Domain and Its Orientation .....	111
Figure B. 14—A Schematic to Two Types of Hydraulic Fracture Configurations. ....	113



Figure B. 15— 3D View Geometry of Two-Stage Multi-Fracture Problem After Fluid Injection. Top Figure is Based on BE Dislocations. Bottom Figure is Based on Displacement Field Near BE Faces. ....	115
Figure B. 16— Top View Geometry of Two-Stage Multi-Fracture Problem After Fluid Injection. Left Figure is Based on BE Dislocations. Right Figure is Based on Displacement Field Near BE Faces. ....	116
Figure B. 17—Mid-Planes of fractures after Deformation.....	116
Figure B. 18—Displacement Field $u_2$ and its gradient.....	117
Figure B. 19—Stress Field Components $\sigma_{11}$ , and $\sigma_{22}$ . Sample grid-nodes are selected for verification purposes. ....	119
Figure B. 20—Principal Stress Components and Their Corresponding Vectors Around Fractures. ....	120
Figure B. 21—Maximum Shearing Stress Field and Its Orientation.....	121

## ABSTRACT

A significant portion of hydrocarbon and geothermal resources in the world, and especially in the United States, is unconventional. Some of the unconventional resources have special geological structures so that their pores are either very small or very limited and unconnected making them nearly impermeable in comparison to traditional hydrocarbon resources. Hydraulic fracturing is one of the prominent stimulation techniques to improve and enhance unconventional reservoir matrix permeability. The major goal in this research is to develop a semi-analytical method to model/simulate hydraulic fracturing based on closed-form solution of an elastic dislocation problem. Our approach is essentially a simplified form of the Boundary Element Method (BEM). The solution is then used to treat the problems of single and multiple -fractures in infinite and semi-infinite reservoirs. The formulation computes displacements and displacement derivatives caused by a dislocation in a finite rectangular source. The results are compared to benchmark solutions previously published. The model is used to analyze pressurized penny-shaped fractures, stress, and displacement distributions around them. This is done using the stress and displacement derivatives at specified grid nodes (field points) in the domain to calculate Cauchy strains and stresses. The stress components at grid nodes are used to calculate principal stress values and directions. The model is verified by comparison with well-known solutions including the pressurized penny-shaped horizontal fracture.

# CHAPTER 1.

## Introduction

Hydraulic fracturing (HF) technology in horizontal well completions can be helpful in developing low-permeability hydrocarbon and geothermal reservoirs (see Figure 1.1). HF is critical to enhance the productivity of geothermal reservoirs. Exploration and production in low-permeability reservoirs such as shale or tight formations has attracted many companies and investors in recent decades. Increasing interest to develop these kinds of reservoirs have brought many challenges for designers, evaluators and researchers (Sesetty and Ghassemi 2015).

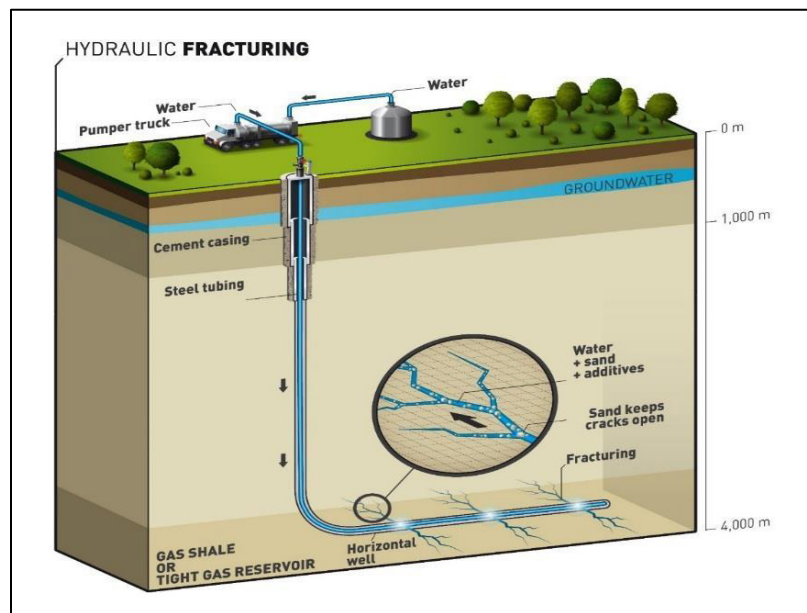


Figure 1.1—A Schematic of Hydraulic Fracturing Development in a Gas Shale Reservoir (Hussain et al. 2017)

The main purpose of HF technique is to enhance the connectivity between the hydrocarbon-bearing rock formation and the well which leads to improved production performance. Historically, the attempt to model HF comes back to Grebe and Stoesser in 1935.

Early investigations of hydraulic fracturing considered 2D geometries (Khristianovich and Zheltov, 1955; Geertsma and de Klerk, 1969 (KGD Model) and then Perkins and Kern, 1961; Nordgren, 1972 (PKN Model). The leak-off and storage effects, then, were added to PKN model in 1972 by Nordgren (Economides Michael J. and Nolte 2000). As mentioned, these classic methods are limited to 2D separate fractures and do not include 3D effects and interactions between multiple HFs. Moreover, the state of stress is absent in these models. When it comes to effect of natural fractures in HF modeling and design, the classical models are invalid. For simplicity, characteristics of some traditional HF models is shown in Table 1.1.

Table 1.1—Characteristics of Some Traditional HF Models (Xiang 2011)

<b>Model</b>	<b>Assumptions</b>	<b>Shape</b>	<b>Application</b>
PKN	Fixed Height, Plain Strain in Vertical Direction	Elliptical Cross Section	Length $\gg$ Height
KGD	Fixed Height, Plain Strain in Horizontal Direction	Rectangle Cross Section	Length $\ll$ Height
Radial	Propagate in a Given Plane, Symmetrical to The Wellbore	Circular Cross Section	Radial

Exerting forces to any solid (such as reservoir rock) leads to deformation and, hence, strains and stresses. External forces may be fluid-driven such as injecting or extracting fluid, or heat-driven which can create temperature gradient. Change in state of stress has several influences in a reservoir. It may lead to rock failure, disturb the field of in-site principal stresses, activate existing faults and fractures, and even change permeability. These are some of the most important factors to plan a successful stimulation strategy. The need to model stress changes and natural fractures' interactions between HFs is essential to predicting "Frac Hits" and helping optimize stimulation. Stress analysis is also very important to predicting rock failure and fracture propagation (for instance, stress intensity factor).

Many other analytical methods have been proposed to assess different aspects of HF process but all of them lack the capability or flexibility to involve different changing factors. Therefore, researchers and engineers have been more interested in robust numerical methods that are able to accurately include the effect of all involving factors such as geometries and physical parameters. One of the most popular numerical approach to model HF process is Finite Element Method (FEM) which for first time was, probably, introduced by Courant in 1942, Argyris in 1956, and Clough in 1956 (Gupta and Meek 1996). It allows a HF modeler to include and consider all involving parameters and their ranges so easily. Moreover, this method is capable to capture any irregularity in the model such as anisotropy and inhomogeneity. To satisfy boundary conditions, discontinuities and singularities at fracture faces and tips other variations of FEM such as Extended FEM (XFEM) have been proposed by defining Enrichment Functions to avoid high mesh density at the boundaries (Moës et al. 1999). Higher mesh density increases the number of degrees

of freedom (DOF) in the model which leads to a larger system of simultaneous equations. In methods such as FEM and XFEM, both the domain (reservoir) and boundaries (fractures) must be discretized appropriately to yield acceptable results. Moreover, domain and boundary mesh must be conformable. The other well-known numerical method is Boundary Element Method (BEM) which was, likely, introduced by Tottenham in 1960s (Brebbia 2017). Unlike FEM, which approximates differential equations solution, BEM deals with integral Equations form of the same differential equations (Ghassemi et al. 2013), (Kumar and Ghassemi 2016). In terms of computer performance, it is an efficient numerical method when surface-to-volume ratio in a model is relatively small (Katsikadelis 2016). Some popular BEM methods are Displacement Discontinuity Method (DD), which is an indirect type of BEM ( Crouch and Starfield, 1980; Verde and Ghassemi 2015), and Fictitious Stress Method (FSM). The DDM is particularly good for modeling fractures (Crouch and Starfield, 1980).

## **1.1. Motivation, Problem Statement and Objectives**

Almost all of the numerical methods mentioned above end up with very large number of DOFs, since the size of elements ought to be reasonably small to obtain acceptable results. In most cases, simulation time for mid-sized models takes days to weeks even with computers with powerful resources (hours for the DD method). This is the motivation for use a semi-analytical method to reduce the volume of numerical computations and mostly the number of DOFs. The proposed method in this research utilizes a closed-form solution of a theory of elasticity problem, namely, a rectangular dislocation in a semi-infinite medium (Volterra 1907), further developed by (Steketee 1958), (Chinnery 1961), (Okada 1985), (Okada 1992). Okada solution provides a set of

closed-form analytical formula to compute displacement field components and their derivatives due to a dislocation (such as SSL, DSL, TL) in a finite/semi-infinite space. Our proposed method just discretizes the boundaries (fractures) and does not require domain (reservoir) discretization. Our method is similar to Displacement Discontinuity Method. DDM which represents the crack as a series of dislocation dipoles whose densities represent the displacement jump across the crack surfaces. Our method, however, uses the analytical solution to a simplified problem (Volterra type dislocation which will be discussed in CHAPTER 2). The dislocation density represents the displacement discontinuity gradient. Our method, then, applies Okada solution to each and every RABEs and uses superposition rule to analyze displacements and displacement derivatives due to fracture(s) dislocation(s) at any field point. However, this method has some limitations. For example, shape of boundary elements must be rectangular, because Okada solution is based for a rectangular fault in a half-space (Okada 1985), (Okada 1992). Therefore, some trade-offs have to be made between the modeling accuracy and efficiency.

### 1.1.1. Okada Solution

Okada solution for a pressurized rectangular dislocation provides the displacement field components,  $u_i$ , and their derivatives  $u_{i,j} = \partial u_i / \partial x_j$ . It assumes that:

- The model domain (reservoir) is a linear elastic homogeneous and isotropic half-space with the stress-free boundary parallel to datum (Ground Surface).
- The BEs are rectangular and regardless of the number of fractures in the model.
- Pressure due to injection throughout the BE surface is constant.

- One of the axes in local coordinate system of BEs (let say  $\xi$ ) must be parallel to that of global coordinate system (let say  $x_1$ ). If not, coordinate system conversion is required (See Figure 2.3).
- The stress convention used in this research is positive sign for compression and negative sign for tension.

## 1.2. Thesis Organization

**Chapter 1** (current chapter) briefly introduces hydraulic fracturing technique and its application and importance to develop hydrocarbon or geothermal reservoirs. Further, it expresses some traditional methods and their disadvantages to model a HF. Then, it mentions more advanced methods of HF modeling, simulation and their advantages or disadvantages. It finally mentions the motivation to carry out current research to overcome a shortcoming of advanced methods. A brief explanation of the methodology is also provided in this chapter.

**Chapter 2** presents Theory of Dislocation and introduces Volterra-type dislocation, its assumptions and the theory behind it. Then, Okada formulation which is the most comprehensive solution to a Volterra-type dislocation is discussed. It consequently provides all the required mathematical equations to derive and compute all the components of displacements' and displacement derivatives' fields. All the involved variables and parameters to compute components are given in **Appendix A**.

**Chapter 3** presents classical and widely-recognized type of Boundary Element Method.



**Chapter 4** briefly presents how to implement the methodology in a computer code. It also addresses some of the findings during computer code development and shortcomings of our method. Further, this chapter compares our method to the Finite Element Method to provide some tips and recommendations to overcome weaknesses and improve numerical performance, especially when the number of DOFs is too high. That said, our proposed method and its corresponding computer code is compared and verified by several well-recognized problems and solutions which may be found in published papers.

**Chapter 5** summarizes the research process conducted in this thesis and addresses some of the findings during research and computer code development. It finally gives some idea and recommendations for improvements in future studies.

**Appendix A** introduces and defines all auxiliary variables and parameters involved in proposed formulation.

**Appendix B**, finally, shows capabilities of the developed computer code and simulator (HiFrac 3D) based on our proposed formulation and method.

## CHAPTER 2.

### Theory of Dislocation

Dislocation theory in the field of Theory of Elasticity was, for first time, introduced by *Vito Volterra* (Volterra 1907). The main goal was to solve elasticity problems which had different types of defects in the body or boundaries of an elastic domain. For this sake, he defines a Dislocation Function as Equation (2.1) to include a surface in a continuous elastic domain that shows discontinuity in displacement components across it (Steketee 1958):

$$\left\{ \begin{array}{l} \Delta \mathbf{u} = \mathbf{U} + \boldsymbol{\Omega} \times \mathbf{r} \\ \boldsymbol{\Omega}^T = -\boldsymbol{\Omega} \\ r = \sqrt{(\xi_i - x_i)^2 + (\xi_j - x_j)^2 + (\xi_k - x_k)^2} \end{array} \right. \quad (2.1)$$

Equation (2.1) represents a rigid body displacement which means both surfaces of the discontinuity remain straight before and after domain deformation (i.e., no curvature on fracture faces). Let  $Ox_1x_2x_3$  be a Cartesian coordinate system with unit vectors  $\mathbf{e}_1$ ,  $\mathbf{e}_2$ , and  $\mathbf{e}_3$  along positive  $x_1$ ,  $x_2$ , and  $x_3$  axes, respectively. The displacement field at point  $Q(x_1, x_2, x_3)$  in an infinite elastic medium due to a Unit Force  $\mathbf{F} = 1 \cdot \mathbf{e}_k$  at the same point in presence of a discontinuous surface,  $\Sigma$ , can be obtained by Volterra Equation (2.2).

$$u_k(x_1, x_2, x_3) = \frac{1}{8\pi\mu} \iint_{\Sigma} \Delta \mathbf{u} \mathbf{T}^k d\Sigma \quad (2.2)$$

Equation (2.2) is valid in an infinite elastic medium. Static equilibrium dictates that the unit force  $\mathbf{F}$  must be compensated by uniformly distributed forces at infinity. In this equation,  $\mathbf{T}^k$  is a traction vector at point  $P(\xi_1, \xi_2, \xi_3)$  which belongs to discontinuous surface,  $\Sigma$ . In other words,  $T_i^k$  is  $i$ th component of the force per unit area on a differential element  $d\Sigma$  due to a unit force in  $k$ th direction at point  $Q(x_1, x_2, x_3)$ . And  $u_k(x_1, x_2, x_3)$  is  $k$ th component of displacement field at point  $Q(x_1, x_2, x_3)$ . Moreover,  $\Delta \mathbf{u} = \Delta \mathbf{u}^+ - \Delta \mathbf{u}^-$  is Dislocation Vector which is assumed known.

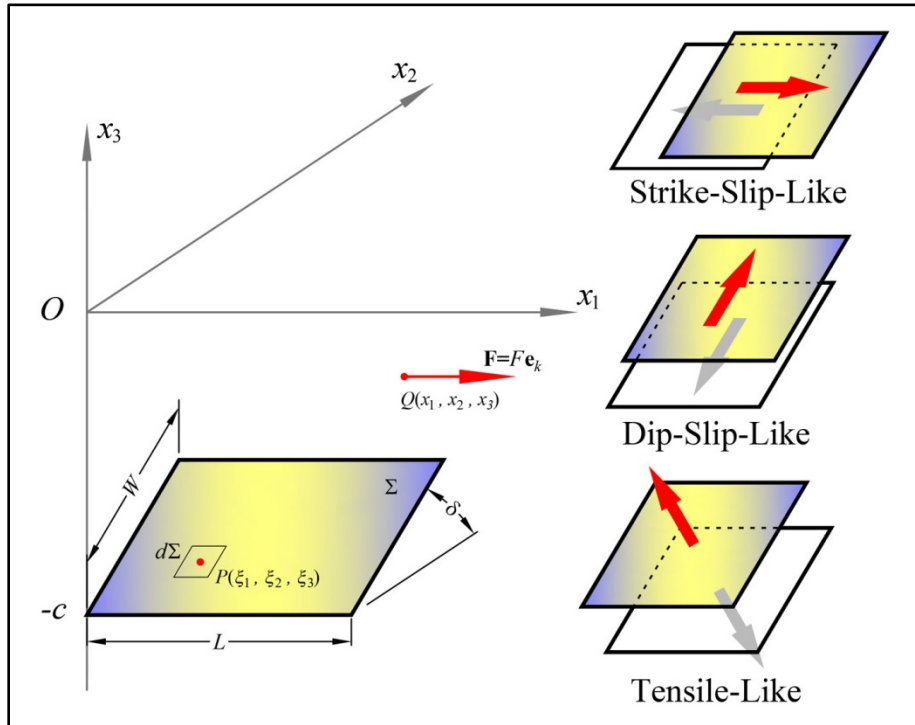


Figure 2.1—A Discontinuous Source in an Elastic Medium

To obtain  $\mathbf{T}^k$ , we use:

$$\left\{ \begin{array}{l} \mathbf{T}^k = \boldsymbol{\sigma}^k \cdot \mathbf{v} \\ \sigma_{ij}^k(\xi_1, \xi_2, \xi_3; x_1, x_2, x_3) = \\ 2\mu(1-\alpha) \left( \delta_{ij} \frac{(\xi_k - x_k)}{r^3} - \delta_{jk} \frac{(\xi_i - x_i)}{r^3} - \delta_{ik} \frac{(\xi_j - x_j)}{r^3} \right) \\ - 6\alpha\mu \frac{(\xi_i - x_i)(\xi_j - x_j)(\xi_k - x_k)}{r^5} \end{array} \right. \quad (2.3)$$

In Equation (2.3),  $\alpha = \frac{\lambda + \mu}{\lambda + 2\mu} = 1 - \left( \frac{v_s}{v_p} \right)^2$  and  $r = \sqrt{(\xi_i - x_i)^2 + (\xi_j - x_j)^2 + (\xi_k - x_k)^2}$ .

Moreover,  $\sigma_{ij}^k(\xi_1, \xi_2, \xi_3; x_1, x_2, x_3)$  represents stress tensor at point  $P(\xi_1, \xi_2, \xi_3)$ , due to a unit force  $\mathbf{F} = 1 \cdot \mathbf{e}_k$  at point  $Q(x_1, x_2, x_3)$ . In other words,  $\sigma_{ij}^k(\xi_1, \xi_2, \xi_3; x_1, x_2, x_3) = \sigma_{ij}^k(P; Q)$ . By substituting Equation (2.1) into (2.2), we obtain:

$$\begin{aligned} u_k(x_1, x_2, x_3) = & \\ & \frac{U_i}{8\pi\mu} \iint_{\Sigma} \sigma_{ij}^k(\xi_1, \xi_2, \xi_3; x_1, x_2, x_3) v_j d\Sigma \\ & + \frac{\Omega_{ij}}{8\pi\mu} \iint_{\Sigma} \left[ \xi_j \sigma_{il}^k(\xi_1, \xi_2, \xi_3; x_1, x_2, x_3) - \xi_i \sigma_{jl}^k(\xi_1, \xi_2, \xi_3; x_1, x_2, x_3) \right] v_l d\Sigma \end{aligned} \quad (2.4)$$

Where, in this equation,  $U_i$  and  $\Omega_{ij}$  are  $U_1, U_2, U_3$ , and  $\Omega_{12}, \Omega_{23}, \Omega_{31}$ , respectively.

Equation (2.4) consists of six integrals. It needs to be mentioned that this equation follows indicial notation convention, i.e.,  $i, j, k, l = 1, 2, 3$  and if a dummy index is repeated, it means summation is implied. It can be inferred that to compute the displacement field components  $u_k(x_1, x_2, x_3)$  due to dislocation  $\Delta \mathbf{u}$ , a unit force  $\mathbf{F} = 1 \cdot \mathbf{e}_k$  is applied at the

same point  $Q(x_1, x_2, x_3)$ . Then the stresses  $\sigma_{ij}^k(\xi_1, \xi_2, \xi_3; x_1, x_2, x_3)$  at points  $P(\xi_1, \xi_2, \xi_3)$  on  $\Sigma$  due to the applied unit force have to be computed. Having all these parameters on hands, integrals in Equation (2.4) over  $\Sigma$  have to be obtained. These integrals were resolved in detail (Chinnery 1961; Steketee 1958) for both infinite and semi-infinite elastic media to obtain displacement fields in an elastic medium (i.e., formation) and its free boundary (i.e., ground surface). However, the solution has been developed and published by other researchers for specific cases, such as horizontal, vertical, or inclined fault cases and/or different dislocation types. A list of some of the most prominent published solutions is provided in Table 2.1 and Table 2.2. Table 2.1 lists solutions for the case of point source (negligible size and shape) and Table 2.2 for the case of a finite rectangular source. It can be seen from the tables that the solutions by Okada (1985 and 1992) are the most comprehensive for both the point source and finite rectangular source cases. Moreover, it yields both internal and surface deformations with their derivatives. We abbreviate Displacement/Displacement Derivative as DDDv in this context.

## 2.1. Description of Okada Solution

The proposed solution to analyze DDDv by Okada has overcome all types of singularities near fracture surface, fracture tips, or points outside fracture surface but at the same plane. However, for more efficiency and reliability we will avoid those singular zones when Implementing the solution. Let  $P(x_1, x_2, x_3)$  be an observation point at which displacement/displacement-derivative is being analyzed and  $F(\xi_1, \xi_2, \xi_3)$  be a point that a point force  $\mathbf{F}$  is being exerted in Figure 2.2.

Table 2.1—Brief History of Published Closed Form Analytical Solutions for the Case of **Point Source**

	<b>Source Orientation</b>	<b>Dislocation Type</b>	<b>Material Behavior</b>	<b>Displ'nt Field</b>	<b>Displacement Derivatives Field</b>
	Ver. Hor. Incl.	SSLDSL TL	$\lambda = \mu$ $\lambda \neq \mu$	$u_1$ $u_2$ $u_3$	$\frac{\partial u_1}{\partial x_1}$ $\frac{\partial u_2}{\partial x_1}$ $\frac{\partial u_3}{\partial x_1}$ $\frac{\partial u_1}{\partial x_2}$ $\frac{\partial u_2}{\partial x_2}$ $\frac{\partial u_3}{\partial x_2}$ $\frac{\partial u_1}{\partial x_3}$ $\frac{\partial u_2}{\partial x_3}$ $\frac{\partial u_3}{\partial x_3}$
Steketee (1958)	☑	☑	☑	☑ ☑ ☑	
Maruyama (1964)	☑ ☑	☑ ☑ ☑	☑	☑ ☑ ☑	
Yamazaki (1978)	☑	☑	☑ ☑	☑ ☑ ☑	
Iwasaki & Sato (1979)	☑ ☑ ☑	☑ ☑	☑ ☑	☑ ☑ ☑	
Okada (1985)	☑ ☑ ☑	☑ ☑ ☑	☑ ☑	☑ ☑ ☑	☑ ☑ ☑ ☑ ☑ ☑ ☑ ☑ ☑

Table 2.2—Brief History of Published Closed Form Analytical Solutions for the Case of **Finite Rectangular Source**

	<b>Source Orientation</b>	<b>Dislocation Type</b>	<b>Material Behavior</b>	<b>Displ'nt Field</b>	<b>Displacement Derivatives Field</b>
	Ver. Hor. Incl.	SSLDSL TL	$\lambda = \mu$ $\lambda \neq \mu$	$u_1$ $u_2$ $u_3$	$\frac{\partial u_1}{\partial x_1}$ $\frac{\partial u_2}{\partial x_1}$ $\frac{\partial u_3}{\partial x_1}$ $\frac{\partial u_1}{\partial x_2}$ $\frac{\partial u_2}{\partial x_2}$ $\frac{\partial u_3}{\partial x_2}$ $\frac{\partial u_1}{\partial x_3}$ $\frac{\partial u_2}{\partial x_3}$ $\frac{\partial u_3}{\partial x_3}$
Chinnery (1961 & 63)	☑	☑	☑ ☑	☑ ☑ ☑	
Mansinha & Smylie (1971)	☑ ☑ ☑	☑ ☑	☑	☑ ☑ ☑	
Converse (1973)	☑ ☑ ☑	☑ ☑	☑ ☑	☑ ☑ ☑	☑ ☑ ☑ ☑ ☑ ☑ ☑ ☑ ☑
Iwasaki & Sato (1979)	☑ ☑ ☑	☑ ☑	☑ ☑		☑ ☑ ☑ ☑ ☑ ☑ ☑ ☑ ☑
Okada (1992)	☑ ☑ ☑	☑ ☑ ☑	☑ ☑	☑ ☑ ☑	☑ ☑ ☑ ☑ ☑ ☑ ☑ ☑ ☑

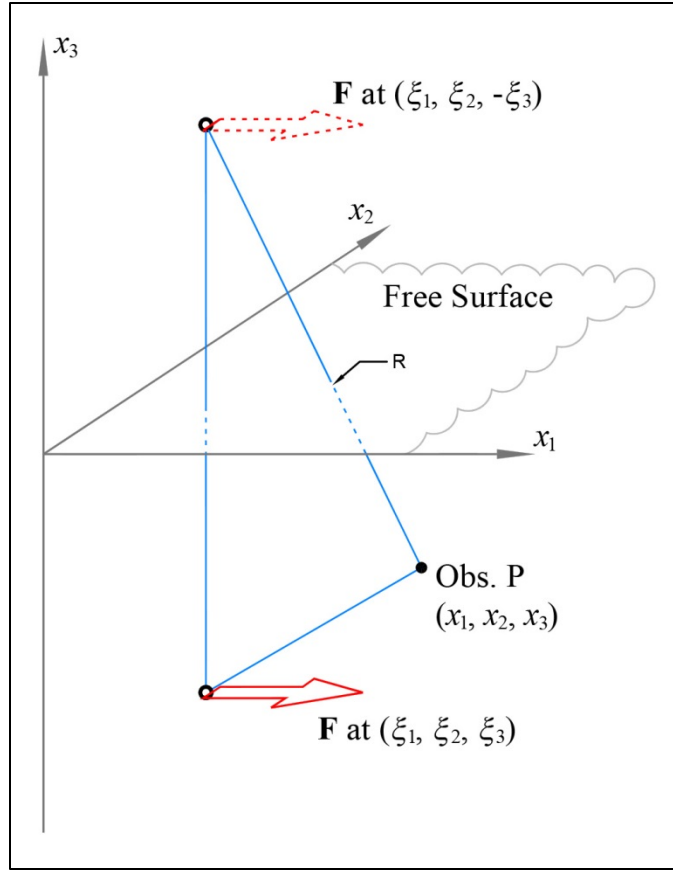


Figure 2.2—A Schematic of a Cartesian frame containing an Observation Point, a Point Force, and an Imagery Point Force

The aim is to obtain  $u_i^j(x_1, x_2, x_3; \xi_1, \xi_2, \xi_3)$  which is the  $i$ th component of the displacement at  $P$  due to  $j$ th component of the point force  $\mathbf{F}$ . Okada shows that  $u_i^j$  can be decomposed to four terms as below.

$$\begin{aligned}
 u_i^j(x_1, x_2, x_3; \xi_1, \xi_2, \xi_3) = & u_{iA}^j(x_1, x_2, -x_3; \xi_1, \xi_2, \xi_3) - u_{iA}^j(x_1, x_2, x_3; \xi_1, \xi_2, -\xi_3) \\
 & + u_{iB}^j(x_1, x_2, x_3; \xi_1, \xi_2, \xi_3) + x_3 u_{iC}^j(x_1, x_2, x_3; \xi_1, \xi_2, \xi_3)
 \end{aligned} \tag{2.5}$$

Equation (2.5), which is superposition rule in linear elasticity, is proven by Mindlin (Mindlin 1936). **Part A** of this equation has two terms. *Term 1* is the displacement field

at image point  $P(x_1, x_2, -x_3)$  due to a point force at  $F(\xi_1, \xi_2, \xi_3)$  in an infinite elastic medium. *Term 2* is the displacement field at the observation point  $P(x_1, x_2, x_3)$  due to an image point force at  $F(\xi_1, \xi_2, -\xi_3)$ . The aim in *Part A* is to eliminate the influence of the upper half-space on the lower one to satisfy the free surface requirements (traction free). But elimination of the upper half-space makes the system unstable because the top surface of the medium is stress-free. To make the top surface stress-free, **Parts B** and **C** have to be added to the equation. It is clear that Parts B and C are surface-dependent and depth-dependent, respectively.

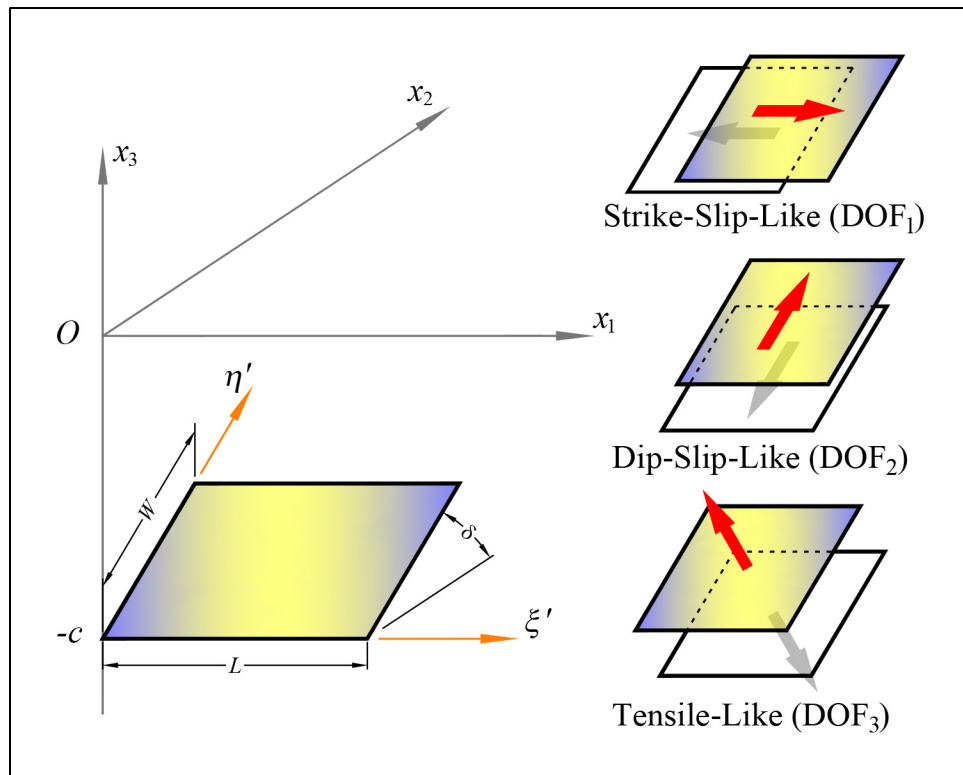


Figure 2.3—A rectangular source with three types of dislocations. Any dislocation at this source can be decomposed to these three dislocation types.



If the source is small enough, it can be assumed a point source. However, if the source is large enough or it is shallow, the influence of point sources on displacement field have to be integrated throughout the surface. According to Figure 2.3, if the source is rectangular, has a dip angle of  $\delta$  with respect to  $Ox_1x_2$  plane, length  $L$  along  $x_1$  axis, and width  $W$  on the other edge, all the displacement field components can be derived for three types of dislocations: Strike-Slip-Like, Dip-Slip-Like, and Tensile-Like. The reason for adding the suffix “Like” is that these terminologies are popular in geology, geophysics, and seismology. Here, we use the same nomenclature to model and simulate HF process.

To obtain DDDv components, integrals in the form of (2.6) have to be resolved for every part and term in Equation (2.5).

$$F_{\Sigma}(x_1, x_2, x_3) = \int_0^L \int_0^W f(\xi', \eta') d\xi' d\eta' = \int_{x_1}^{x_1-L} \int_p^{p-W} f(\xi, \eta) d\xi d\eta \quad (2.6)$$

It needs to be noted that all integrals are carried out in a local coordinate frame attached to the rectangular source  $\xi'\eta'$  but, for simplicity, they are converted to another coordinate frame attached to the point of interest (or observation point)  $P\xi\eta$  which is parallel to the image rectangular source plane. For better understanding, both local coordinate frames  $\xi'\eta'$  and  $P\xi\eta$  are illustrated in Figure 2.4 and also Appendix A. The process has been discussed in detail in Appendix A. In addition, all the variables in Table 2.3 to Table 2.6 have been defined in the same appendix. All geometrical variables and parameters are, also, illustrated in Figure 2.4.

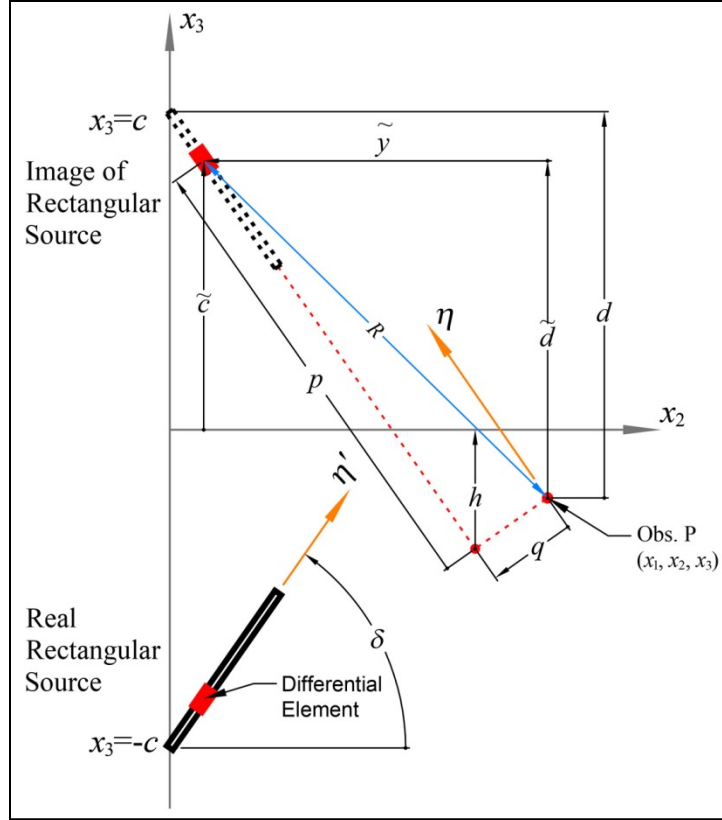


Figure 2.4—Side view of A finite rectangular source with its image pair. Axes  $x_1$ ,  $\xi$ , and  $\xi'$  are perpendicular to the page. Axes  $x_1$  and  $\xi'$  are outward, but axis  $\xi$  at observation point is inward.

## 2.2. Kinematic Equations for the Case of

### Finite Rectangular Source

Deriving the integrals in (2.4), (2.5), and general form of (2.6) lead to 9 set of functions of form  $f_i^M(\xi, \eta, x_3)$  to compute displacement field components for each dislocation type.

Table 2.3—All required functions to analyze displacement field components due to a rectangular source dislocation in a half-space (Okada-1992, with some modifications)

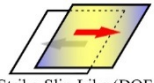
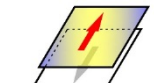
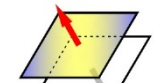
Disl. Type	$f_1^A, f_2^A, \text{ and } f_3^A$	$f_1^B, f_2^B, \text{ and } f_3^B$	$f_1^C, f_2^C, \text{ and } f_3^C$	
 Strike-Slip-Like (DOF <sub>1</sub> )	$\frac{\Theta}{2} + \frac{\alpha}{2} \xi q Y_{11}$ $\frac{\alpha q}{2 R}$ $\frac{1-\alpha}{2} \ln(R+\eta) - \frac{\alpha}{2} q^2 Y_{11}$	$-\xi q Y_{11} - \Theta$ $-\frac{q}{R}$ $q^2 Y_{11}$	$-\frac{1-\alpha}{\alpha} I_4 \sin \delta$ $+\frac{1-\alpha}{\alpha} \frac{\tilde{y}}{R+\tilde{d}} \sin \delta$ $-\frac{1-\alpha}{\alpha} I_3 \sin \delta$	$(1-\alpha) \xi Y_{11} \cos \delta$ $-\alpha \xi q Z_{32}$ $(1-\alpha) \left( \frac{\cos \delta}{R} + 2q Y_{11} \sin \delta \right) - \alpha \frac{\tilde{c}q}{R^3}$ $(1-\alpha) q Y_{11} \cos \delta - \alpha \left( \frac{\tilde{c}\eta}{R^3} - x_3 Y_{11} + \xi^2 Z_{32} \right)$
 Dip-Slip-Like (DOF <sub>2</sub> )	$\frac{\alpha q}{2 R}$ $\frac{\Theta}{2} + \frac{\alpha}{2} \eta q X_{11}$ $\frac{1-\alpha}{2} \ln(R+\xi) - \frac{\alpha}{2} q^2 X_{11}$	$-\frac{q}{R}$ $-\eta q X_{11} - \Theta$ $q^2 X_{11}$	$+\frac{1-\alpha}{\alpha} I_2 \sin \delta \cos \delta$ $-\frac{1-\alpha}{\alpha} \frac{\xi}{R+\tilde{d}} \sin \delta \cos \delta$ $+\frac{1-\alpha}{\alpha} I_1 \sin \delta \cos \delta$	$(1-\alpha) \frac{\cos \delta}{R} - q Y_{11} \sin \delta - \alpha \frac{\tilde{c}q}{R^3}$ $(1-\alpha) \tilde{y} X_{11} - \alpha \tilde{c} \eta q X_{32}$ $-\tilde{d} X_{11} - \xi Y_{11} \sin \delta - \alpha \tilde{c} (X_{11} - q^2 X_{32})$
 Tensile-Like (DOF <sub>3</sub> )	$-\frac{1-\alpha}{2} \ln(R+\eta) - \frac{\alpha}{2} q^2 Y_{11}$ $-\frac{1-\alpha}{2} \ln(R+\xi) - \frac{\alpha}{2} q^2 X_{11}$ $\frac{\Theta}{2} - \frac{\alpha}{2} q (\eta X_{11} + \xi Y_{11})$	$q^2 Y_{11}$ $q^2 X_{11}$ $q (\eta X_{11} + \xi Y_{11}) - \Theta - \frac{1-\alpha}{\alpha} I_1 \sin^2 \delta$	$-\frac{1-\alpha}{\alpha} I_2 \sin^2 \delta$ $+\frac{1-\alpha}{\alpha} \frac{\xi}{R+\tilde{d}} \sin^2 \delta$	$-(1-\alpha) \left( \frac{\sin \delta}{R} + q Y_{11} \cos \delta \right) - \alpha (x_3 Y_{11} - q^2 Z_{32})$ $(1-\alpha) 2\xi Y_{11} \sin \delta + \tilde{d} X_{11} - \alpha \tilde{c} (X_{11} - q^2 Z_{32})$ $(1-\alpha) (\tilde{y} X_{11} + \xi Y_{11} \cos \delta) + \alpha q (\tilde{c} \eta X_{32} + \xi Z_{32})$

Table 2.4—All required functions to analyze  $x_1$ -derivative of displacement field components due to a rectangular source dislocation in a half-space (Okada-1992, with some modifications)

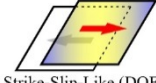
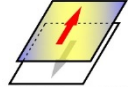
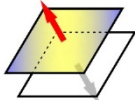
Disl. Type	$f_{1,1}^A, f_{2,1}^A, \text{ and } f_{3,1}^A$	$f_{1,1}^B, f_{2,1}^B, \text{ and } f_{3,1}^B$	$f_{1,1}^C, f_{2,1}^C, \text{ and } f_{3,1}^C$
 Strike-Slip-Like (DOF <sub>1</sub> )	$-\frac{1-\alpha}{2}qY_{11} - \frac{\alpha}{2}\xi^2qY_{32}$ $-\frac{\alpha}{2}\frac{\xi q}{R^3}$ $\frac{1-\alpha}{2}\xi Y_{11} + \frac{\alpha}{2}\xi q^2Y_{32}$	$\xi^2qY_{32} \quad -\frac{1-\alpha}{\alpha}J_1 \sin \delta$ $\frac{\xi q}{R^3} \quad -\frac{1-\alpha}{\alpha}J_2 \sin \delta$ $-\xi q^2Y_{32} \quad -\frac{1-\alpha}{\alpha}J_3 \sin \delta$	$(1-\alpha)Y_0 \cos \delta \quad -\alpha qZ_0$ $-(1-\alpha)\xi \left( \frac{\cos \delta}{R^3} + 2qY_{32} \sin \delta \right) + \alpha \frac{3\tilde{c}\xi q}{R^5}$ $-(1-\alpha)\xi qY_{32} \cos \delta \quad +\alpha \xi \left( \frac{3\tilde{c}\eta}{R^5} - x_3Y_{32} - Z_{32} - Z_0 \right)$
 Dip-Slip-Like (DOF <sub>2</sub> )	$-\frac{q}{2}Y_{11} \quad -\frac{\alpha}{2}\frac{\xi q}{R^3}$ $-\frac{\alpha}{2}\frac{\eta q}{R^3}$ $\frac{1-\alpha}{2}\frac{1}{R} \quad +\frac{\alpha}{2}\frac{q^2}{R^3}$	$\frac{\xi q}{R^3} \quad +\frac{1-\alpha}{\alpha}J_4 \sin \delta \cos \delta$ $\frac{\eta q}{R^3} + qY_{11} + \frac{1-\alpha}{\alpha}J_5 \sin \delta \cos \delta$ $-\frac{q^2}{R^3} \quad +\frac{1-\alpha}{\alpha}J_6 \sin \delta \cos \delta$	$-(1-\alpha)\frac{\xi}{R^3} \cos \delta + \xi qY_{32} \sin \delta \quad +\alpha \frac{3\tilde{c}\xi q}{R^5}$ $-(1-\alpha)\frac{\tilde{y}}{R^3} \quad +\alpha \frac{3\tilde{c}\eta q}{R^5}$ $\frac{\tilde{d}}{R^3} \quad -Y_0 \sin \delta \quad +\alpha \frac{\tilde{c}}{R^3} \left( 1 - \frac{3q^2}{R^2} \right)$
 Tensile-Like (DOF <sub>3</sub> )	$-\frac{1-\alpha}{2}\xi Y_{11} + \frac{\alpha}{2}\xi q^2Y_{32}$ $-\frac{1-\alpha}{2}\frac{1}{R} + \frac{\alpha}{2}\frac{q^2}{R^3}$ $-\frac{1-\alpha}{2}qY_{11} - \frac{\alpha}{2}q^3Y_{32}$	$-\xi q^2Y_{32} \quad -\frac{1-\alpha}{\alpha}J_4 \sin^2 \delta$ $-\frac{q^2}{R^3} \quad -\frac{1-\alpha}{\alpha}J_5 \sin^2 \delta$ $q^3Y_{32} \quad -\frac{1-\alpha}{\alpha}J_6 \sin^2 \delta$	$(1-\alpha)\frac{\xi}{R^3}(\sin \delta + \xi qY_{32} \cos \delta) + \alpha \xi (x_3Y_{32} - q^2Z_{53})$ $2(1-\alpha)Y_0 \sin \delta - \frac{\tilde{d}}{R^3} \quad +\alpha \frac{\tilde{c}}{R^3} \left( 1 - \frac{3q^2}{R^2} \right)$ $-(1-\alpha) \left[ \frac{\tilde{y}}{R^3} - Y_0 \cos \delta \right] \quad -\alpha \left( \frac{3\tilde{c}\eta q}{R^5} - qZ_0 \right)$

Table 2.5—All required functions to analyze  $x_2$ -derivative of displacement field components due to a rectangular source dislocation in a half-space (Okada-1992, with some modifications)

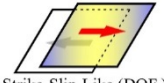
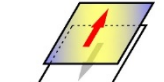
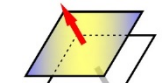
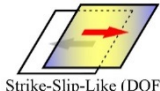
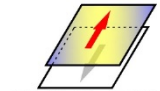
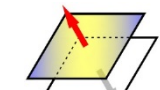
Disl. Type	$f_{1,2}^A, f_{2,2}^A, \text{ and } f_{3,2}^A$	$f_{1,2}^B, f_{2,2}^B, \text{ and } f_{3,2}^B$	$f_{1,2}^C, f_{2,2}^C, \text{ and } f_{3,2}^C$
 Strike-Slip-Like (DOF <sub>1</sub> )	$\frac{1-\alpha}{2} \xi Y_{11} \sin \delta + \frac{\tilde{d}}{2} X_{11} + \frac{\alpha}{2} \xi F$ $\frac{\alpha}{2} E$ $\frac{1-\alpha}{2} \left( \frac{\cos \delta}{R} + q Y_{11} \sin \delta \right) - \frac{\alpha}{2} q F$	$-\xi F - \tilde{d} X_{11} + \frac{1-\alpha}{\alpha} K_1 \sin \delta$ $-E + \frac{1-\alpha}{\alpha} K_2 \sin \delta$ $q F - \frac{1-\alpha}{\alpha} K_3 \sin \delta$	$-(1-\alpha) \xi \left( \frac{\cos \delta}{R^3} + q Y_{32} \sin \delta \right) \cos \delta - \alpha \xi \left[ \frac{3\tilde{c}\tilde{d}}{R^5} - (x_3 Y_{32} + Z_{32} + Z_0) \sin \delta \right]$ $(1-\alpha) \left[ -\frac{\tilde{y}}{R^3} \cos \delta + 2 \left( \frac{\tilde{d}}{R^3} \dots \right) \sin \delta \right] - \alpha \tilde{c} \left( \frac{\sin \delta}{R^3} - \frac{3\tilde{y}q}{R^5} \right)$ $(1-\alpha) \left( \frac{\tilde{d}}{R^3} - Y_0 \sin \delta \right) \cos \delta - \alpha \left[ \begin{aligned} &\tilde{c} \left( \frac{\cos \delta}{R^3} - \frac{3\tilde{y}\eta}{R^5} \right) + \dots \\ &x_3 \left( \frac{\cos \delta}{R^3} + q Y_{32} \sin \delta \right) \dots \\ &-\xi^2 \left( \frac{3\tilde{c}}{R^5} \cos \delta + \left( \frac{Y_{32} \cos \delta \dots}{+qZ_{53}} \right) \sin \delta \right) \end{aligned} \right]$
 Dip-Slip-Like (DOF <sub>2</sub> )	$\frac{\alpha}{2} E$ $\frac{1-\alpha}{2} \tilde{d} X_{11} + \frac{\xi}{2} Y_{11} \sin \delta + \frac{\alpha}{2} \eta G$ $\frac{1-\alpha}{2} \tilde{y} X_{11} - \frac{\alpha}{2} q G$	$-E + \frac{1-\alpha}{\alpha} K_4 \sin \delta \cos \delta$ $-\eta G - \xi Y_{11} \sin \delta + \frac{1-\alpha}{\alpha} K_5 \sin \delta \cos \delta$ $q G + \frac{1-\alpha}{\alpha} K_6 \sin \delta \cos \delta$	$-(1-\alpha) \frac{\tilde{y}}{R^3} \cos \delta - \left( \frac{\tilde{d}}{R^3} - Y_0 \sin \delta \right) \sin \delta - \alpha \tilde{c} \left( \frac{\sin \delta}{R^3} - \frac{3\tilde{y}q}{R^5} \right)$ $(1-\alpha) (X_{11} - \tilde{y}^2 X_{32}) - \alpha \tilde{c} \left[ \begin{aligned} &(\tilde{d} + 2q \cos \delta) X_{32} \dots \\ &-\tilde{y}\eta q X_{53} \end{aligned} \right]$ $\tilde{y} \tilde{d} X_{32} + \xi \left( \frac{\cos \delta}{R^3} + q Y_{32} \sin \delta \right) \sin \delta + \alpha \tilde{c} \left[ \begin{aligned} &\tilde{y} X_{32} + q \left( \frac{2X_{32} \sin \delta \dots}{-\tilde{y}q X_{53}} \right) \end{aligned} \right]$
 Tensile-Like (DOF <sub>3</sub> )	$-\frac{1-\alpha}{2} \left( \frac{\cos \delta}{R} + q Y_{11} \sin \delta \right) - \frac{\alpha}{2} q F$ $-\frac{1-\alpha}{2} \tilde{y} X_{11} - \frac{\alpha}{2} q G$ $\frac{1-\alpha}{2} (\tilde{d} X_{11} + \xi Y_{11} \sin \delta) + \frac{\alpha}{2} q H$	$q F - \frac{1-\alpha}{\alpha} K_4 \sin^2 \delta$ $q G - \frac{1-\alpha}{\alpha} K_5 \sin^2 \delta$ $-q H - \frac{1-\alpha}{\alpha} K_6 \sin^2 \delta$	$(1-\alpha) \left( \frac{q}{R^3} + Y_0 \sin \delta \cos \delta \right) + \alpha \left( \frac{x_3}{R^3} \cos \delta + \frac{3\tilde{c}\tilde{d}q}{R^5} - q Z_0 \sin \delta \right)$ $-2(1-\alpha) \xi P \sin \delta + \tilde{y} \tilde{d} X_{32} + \alpha \tilde{c} \left[ \begin{aligned} &(\tilde{y} + 2q \sin \delta) X_{32} \dots \\ &-\tilde{y}q^2 X_{53} \end{aligned} \right]$ $-(1-\alpha) (\xi P \cos \delta - X_{11} + \tilde{y}^2 X_{32}) + \alpha \tilde{c} \left[ (\tilde{d} + 2q \cos \delta) X_{32} - \tilde{y}\eta q X_{53} \right]$

Table 2.6—All required functions to analyze  $x_3$ -derivative of displacement field components due to a rectangular source dislocation in a half-space (Okada-1992, with some modifications)

Disl. Type	$f_{1,3}^A, f_{2,3}^A, \text{ and } f_{3,3}^A$	$f_{1,3}^B, f_{2,3}^B, \text{ and } f_{3,3}^B$	$f_{1,3}^C, f_{2,3}^C, \text{ and } f_{3,3}^C$
 Strike-Slip-Like (DOF <sub>1</sub> )	$\frac{1-\alpha}{2} \xi Y_{11} \cos \delta + \frac{\tilde{y}}{2} X_{11} + \frac{\alpha}{2} \xi F'$ $\frac{\alpha}{2} E'$ $-\frac{1-\alpha}{2} \left( \frac{\sin \delta}{R} - q Y_{11} \cos \delta \right) - \frac{\alpha}{2} q F'$	$-\xi F' - \tilde{y} X_{11} + \frac{1-\alpha}{\alpha} L_1 \sin \delta$ $-E'$ $+ \frac{1-\alpha}{\alpha} L_2 \sin \delta$ $q F' + \frac{1-\alpha}{\alpha} L_3 \sin \delta$	$(1-\alpha) \xi \left( \frac{\sin \delta}{R^3} - q Y_{32} \cos \delta \right) \cos \delta - \alpha \xi \left[ \frac{3\tilde{c}\tilde{y}}{R^5} + q Y_{32} \dots \right. \\ \left. - (x_3 Y_{32} + Z_{32} + Z_0) \cos \delta \right]$ $2(1-\alpha) \left( \frac{\tilde{y}}{R^3} - Y_0 \cos \delta \right) \sin \delta + \frac{\tilde{d}}{R^3} \cos \delta - \alpha \left( \frac{\tilde{c} + \tilde{d}}{R^3} \cos \delta + \frac{3\tilde{c}\tilde{d}q}{R^5} \right)$ $\left( \frac{\tilde{y}}{R^3} - Y_0 \sin \delta \right) \cos \delta - \alpha \left( \frac{\tilde{c} + \tilde{d}}{R^3} \sin \delta - \frac{3\tilde{c}\tilde{y}q}{R^5} \dots \right. \\ \left. - Y_0 \sin^2 \delta + q Z_0 \cos \delta \right)$
 Dip-Slip-Like (DOF <sub>2</sub> )	$\frac{\alpha}{2} E'$ $\frac{1-\alpha}{2} \tilde{y} X_{11} + \frac{\xi}{2} Y_{11} \cos \delta + \frac{\alpha}{2} \eta G'$ $-\frac{1-\alpha}{2} \tilde{d} X_{11} - \frac{\alpha}{2} q G'$	$-E' - \frac{1-\alpha}{\alpha} L_4 \sin \delta \cos \delta$ $-\eta G' - \xi Y_{11} \cos \delta - \frac{1-\alpha}{\alpha} L_5 \sin \delta \cos \delta$ $q G' - \frac{1-\alpha}{\alpha} L_6 \sin \delta \cos \delta$	$-\frac{q}{R^3} + Y_0 \sin \delta \cos \delta - \alpha \left( \frac{\tilde{c} + \tilde{d}}{R^3} \cos \delta + \frac{3\tilde{c}\tilde{d}q}{R^5} \right)$ $(1-\alpha) \tilde{y} \tilde{d} X_{32} - \alpha \tilde{c} \left[ (\tilde{y} - 2q \sin \delta) X_{32} \dots \right. \\ \left. + \tilde{d} \eta q X_{53} \right]$ $-\xi P' \sin \delta + X_{11} - \tilde{d}^2 X_{32} - \alpha \tilde{c} \left[ (\tilde{d} - 2q \cos \delta) X_{32} - \tilde{d} q^2 X_{53} \right]$
 Tensile-Like (DOF <sub>3</sub> )	$\frac{1-\alpha}{2} \left( \frac{\cos \delta}{R} + q Y_{11} \cos \delta \right) - \frac{\alpha}{2} q F'$ $\frac{1-\alpha}{2} \tilde{d} X_{11} - \frac{\alpha}{2} q G'$ $\frac{1-\alpha}{2} (\tilde{y} X_{11} + \xi Y_{11} \cos \delta) + \frac{\alpha}{2} q H'$	$q F' + \frac{1-\alpha}{\alpha} L_4 \sin^2 \delta$ $q G' + \frac{1-\alpha}{\alpha} L_5 \sin^2 \delta$ $-q H' + \frac{1-\alpha}{\alpha} L_6 \sin^2 \delta$	$-(1-\alpha) \left( \frac{\eta}{R^3} - Y_0 \cos^2 \delta \right) - \alpha \left( \frac{x_3 \sin \delta}{R^3} - \frac{3\tilde{c}\tilde{y}q}{R^5} + Y_{11} \dots \right. \\ \left. - q^2 Y_{32} + q Z_0 \cos \delta \right)$ $2(1-\alpha) \xi P' - X_{11} + \tilde{d}^2 X_{32} - \alpha \tilde{c} \left[ (\tilde{d} - 2q \cos \delta) X_{32} \dots \right. \\ \left. - \tilde{d} q^2 X_{53} \right]$ $(1-\alpha) (\xi P' \cos \delta + \tilde{y} \tilde{d} X_{32}) + \alpha \tilde{c} \left[ (\tilde{y} - 2q \sin \delta) X_{32} \dots \right. \\ \left. + \tilde{d} \eta q X_{53} \right] + \alpha \xi Q'$

The index  $i = 1, 2,$  and  $3,$  and the index  $M = A, B,$  and  $C$  which were explained in reference to Equation (2.5). Functions  $f_i^M(\xi, \eta, x_3)$  in Table 2.3 are indefinite integrals. To compute the value of a displacement component, they have to be acquired in upper-bounds and lower-bounds of the domain. Therefore, Equation (2.7) is used to obtain the value at an Obs. Point.

$$\begin{aligned}
 u_i^M &= f_i^M(\xi, \eta, x_3) \Big|_{\xi=x_1}^{\xi=x_1-L} \Big|_{\eta=p}^{\eta=p-W} \\
 &= f_i^M(x_1 - L, p - W, x_3) + f_i^M(x_1, p, x_3) \\
 &\quad - f_i^M(x_1 - L, p, x_3) \quad - f_i^M(x_1, p - W, x_3)
 \end{aligned} \tag{2.7}$$

To analyze derivatives of displacement field components, Equation (2.8) is required. Note that, definite integrals in Equation (2.7) are with respect to  $\xi$  and  $\eta$  while derivatives in Equation (2.8) are with respect to  $x_i$ .

$$\begin{aligned}
 u_{i,j}^M &= \frac{\partial f_i^M(\xi, \eta, x_3)}{\partial x_j} \Big|_{\xi=x_1}^{\xi=x_1-L} \Big|_{\eta=p}^{\eta=p-W} \\
 &= f_{i,j}^M(x_1 - L, p - W, x_3) + f_{i,j}^M(x_1, p, x_3) \\
 &\quad - f_{i,j}^M(x_1 - L, p, x_3) \quad - f_{i,j}^M(x_1, p - W, x_3)
 \end{aligned} \tag{2.8}$$

Therefore, chain rule technique needs to be applied. The summary of results of form  $f_{i,j}^M(\xi, \eta, x_3)$  are in Table 2.4, Table 2.5, and Table 2.6. All involving variables and parameters in these tables are explained in detail in **Appendix A**. Since integrals are in

local coordinate frame, the results will, also, be in the same frame. The results  $u_i^M$  and  $u_{i,j}^M$  have to be converted to global coordinate frame thereupon. Therefore,

$$\begin{aligned}
u_1(x_1, x_2, x_3) &= \frac{U}{2\pi} \left( u_1^A - \hat{u}_1^A + u_1^B + x_3 u_1^C \right) \\
u_2(x_1, x_2, x_3) &= \frac{U}{2\pi} \left[ \begin{aligned} &\left( u_2^A - \hat{u}_2^A + u_2^B + x_3 u_2^C \right) \cos \delta \dots \\ &\dots - \left( u_3^A - \hat{u}_3^A + u_3^B + x_3 u_3^C \right) \sin \delta \end{aligned} \right] \\
u_3(x_1, x_2, x_3) &= \frac{U}{2\pi} \left[ \begin{aligned} &\left( u_2^A - \hat{u}_2^A + u_2^B - x_3 u_2^C \right) \sin \delta \dots \\ &\dots + \left( u_3^A - \hat{u}_3^A + u_3^B - x_3 u_3^C \right) \cos \delta \end{aligned} \right]
\end{aligned} \tag{2.9}$$

And,

$$\begin{aligned}
u_{1,j}(x_1, x_2, x_3) &= \frac{U}{2\pi} \left( u_{1,j}^A - \hat{u}_{1,j}^A + u_{1,j}^B + x_3 u_{1,j}^C \right) \\
u_{2,j}(x_1, x_2, x_3) &= \frac{U}{2\pi} \left[ \begin{aligned} &\left( u_{2,j}^A - \hat{u}_{2,j}^A + u_{2,j}^B + x_3 u_{2,j}^C \right) \cos \delta \dots \\ &\dots - \left( u_{3,j}^A - \hat{u}_{3,j}^A + u_{3,j}^B + x_3 u_{3,j}^C \right) \sin \delta \end{aligned} \right] \\
u_{3,j}(x_1, x_2, x_3) &= \frac{U}{2\pi} \left[ \begin{aligned} &\left( u_{2,j}^A - \hat{u}_{2,j}^A + u_{2,j}^B - x_3 u_{2,j}^C \right) \sin \delta \dots \\ &\dots + \left( u_{3,j}^A - \hat{u}_{3,j}^A + u_{3,j}^B - x_3 u_{3,j}^C \right) \cos \delta \end{aligned} \right]
\end{aligned} \tag{2.10}$$

Here,  $\hat{u}_i^A$  and  $\hat{u}_{i,j}^A$  are contribution of the image rectangular source on displacement and displacement derivative field components in Equations (2.9) and (2.10), i.e., the value of  $x_3$  has to be substituted by  $-x_3$ .

By all the material-property-related and geometry-related values on hand in a HF model, all the variables and parameters given in Appendix A can be computed and plugged into equations of forms  $f_i^M(\xi, \eta, x_3)$  and  $f_{i,j}^M(\xi, \eta, x_3)$  in Table 2.3 to Table 2.6. All displacement and displacement derivative fields' components, now, can be obtained by



substituting  $f_i^M(\xi, \eta, x_3)$  and  $f_{i,j}^M(\xi, \eta, x_3)$  in Equations (2.7) and (2.8) respectively. Consequently, variable  $u_i^M$  and  $u_{i,j}^M$  from Equations (2.7) and (2.8) have to be substituted in Equations (2.9) and (2.10). To obtain equations of forms  $\hat{u}_i^M$  and  $\hat{u}_{i,j}^M$ , the coordinate value  $x_3$  has to be substituted by  $-x_3$ . By all displacement field components on hand, deformation of the domain (reservoir) is achievable. Furthermore, by all displacement derivative fields' components and material properties on hand, both Cauchy strain and stress components will be analyzed by Equation (2.11) which is given below.

$$\begin{cases} \varepsilon_{ij} = \frac{1}{2}(u_{i,j} + u_{j,i}) \\ \sigma_{ij} = \lambda \varepsilon_{kk} \delta_{ij} + 2\mu \varepsilon_{ij} \end{cases} \quad (2.11)$$

In Equation (2.11),  $\mu$  and  $\lambda$  are Lamé constants. And in this equation,  $\delta_{ij}$  is called Kronecker delta and defined as,

$$\delta_{ij} = \begin{cases} 0 & \text{if } i \neq j \\ 1 & \text{if } i = j \end{cases} \quad (2.12)$$

In Linear Algebra, it is equivalent to  $3 \times 3$  Identity Matrix  $\mathbf{I}_{3 \times 3}$ . If Poisson's Ratio, Normal and Shear Elastic moduli are given instead, we have,

$$\lambda = \frac{E\nu}{(1+\nu)(1-2\nu)} \quad \text{and} \quad \mu = G \quad (2.13)$$

### 2.3. The Case of Multiple Discontinuities in an Elastic Half-Space Medium

The solution discussed in section 2.2. is for just one rectangular discontinuity (let say fracture or fault in a reservoir). Since material behavior is linear and elastic, superposition rule can be applied to model multiple rectangular discontinuities. All we need is to compute all the components of  $DDDv$  for each discontinuity and then combine values.

### 2.4. Model Development

The above formulations have been coded into algorithms by Okada (2001). In this work we use his DC3D for a finite rectangular source. The Okada sub-programs were overhauled and improved to make it compatible with PGI Visual FORTRAN 18.5 and Intel Parallel Studio XE 2019 standards. All required input parameters and their corresponding descriptions are given in Table 2.7. Input variables are illustrated in Figure 2.5. Dislocation types SSL, DSL, and TL in Figure 2.5 show positive sign conventions. It is obvious that output variables are scalar components of  $DDDv$  fields. The unit of  $u_i$  is the same as that of dislocations. However, the unit of  $u_{i,j}$  is:

$$\frac{\text{Unit of Dislocation}}{\text{Unit of } X_i} \tag{2.14}$$

Table 2.7—Input Variables and Their Descriptions

Input Arguments (64-bit Types)	Description
ALPHA	Medium Constant = $\frac{\lambda + \mu}{\lambda + 2\mu} = 1 - \left(\frac{v_s}{v_p}\right)^2$  $\lambda = \frac{E\nu}{(1+\nu)(1-2\nu)}$ and $\mu = G = \frac{E}{2(1+\nu)}$
X1, X2, X3	Field Point $P$ . Note: $X3 \leq 0$
DEPTH	Depth of the Reference Point (Midpoint of Rectangle) which is greater than 0.
DIP	Dip Angle $0^\circ \leq \delta \leq 90^\circ$
AL1, AL2	Extent of Rectangle in $\xi'$ or $x_1$ direction (Strike Direction)
AW1, AW2	Extent of Rectangle in $\eta'$ direction (Dip Direction)
DISL1	Strike-Slip-Like Dislocation Value (Left-Lateral-Like, Positive)
DISL2	Dip-Slip-Like Dislocation Value (Reverse-Like, Positive)
DISL3	Tensile-Like Dislocation Value (Perpendicular to BE Plane)

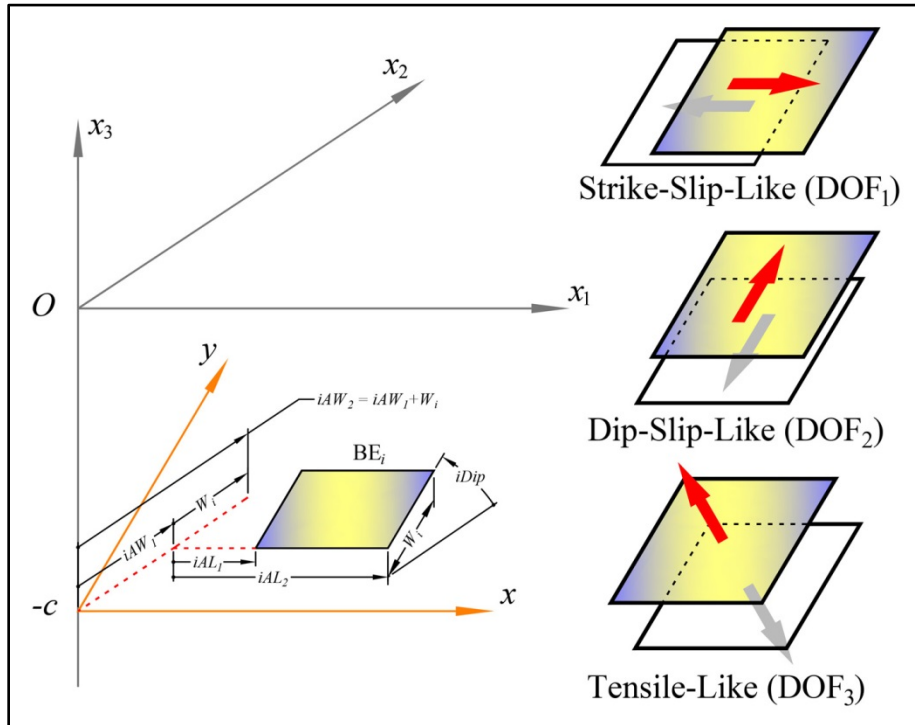


Figure 2.5—Input Variables to Define RABE. Parameters  $iAW_1$  and  $iAW_2$  are measured Assuming  $iDip = 0^\circ$ .

## 2.5. Locus of Singularities

At any field point where the denominator of functions in Table 2.3 to Table 2.6 become zero (Division by Zero) is/are locus of singularities which should be avoided. The sub-program DC3D has a controlling output IRET which is to identify whether the computation is singular or not. Our simulator always checks IRET to possibly relocate field point (say grid-nodes) by  $10^{-5}$  unit to avoid singularity. It is obvious that at the edge and plane of the rectangular source, the solution is singular.

## CHAPTER 3.

# Boundary Element Procedure to Model and Simulate a Hydraulic Fracture

Before proposing our new boundary element procedure to model a HF problem, it is a good idea to discuss about conventional BEM and then compare it with our approach. As mentioned in introductory chapter, Boundary Element Methods, unlike Finite Element Methods, deal with Integral Equations. But most physical problems are known by partial differential equation representation. Some of the well-known continuum mechanics problems such as Navier-Cauchy equation (in solid mechanics) or diffusivity equation (in reservoir fluid transportation modeling) are just a few examples. Therefore, boundary element methods are not directly applicable to solve those problems and the field equation for mentioned problems should be first represented in an integral form. Here, we attempt to explain a conventional boundary element method by means of a well-known elastostatic problem.

### 3.1. Two-Dimensional Plane-Strain

#### Problem in Elasticity (Katsikadelis 2016)

Suppose an elastic body in a Cartesian coordinate frame  $Ox_1x_2x_3$  with unit vectors  $\mathbf{e}_i$  (Figure 3.1). Note that  $i$  is an indicial notation which summation applies if repeated. The body is under influence of body force  $\mathbf{F}^b = F_i^b \mathbf{e}_i$ , a concentrated force  $\mathbf{F} = F_i \mathbf{e}_i$  at point  $Q(\xi_1, \xi_2)$ . The locus of the force  $\mathbf{F}$  is, also, showed as  $\mathbf{Q} = \xi_i \mathbf{e}_i$ . The goal is to

obtain displacement field components  $u_i$  and their derivatives  $u_{i,j}$  at an arbitrary point  $P(x_1, x_2)$ , where  $\mathbf{P} = x_i \mathbf{e}_i$ . According to Equations (2.11) to (2.13),  $u_{i,j}$  is required to compute the components of strain and stress tensors.

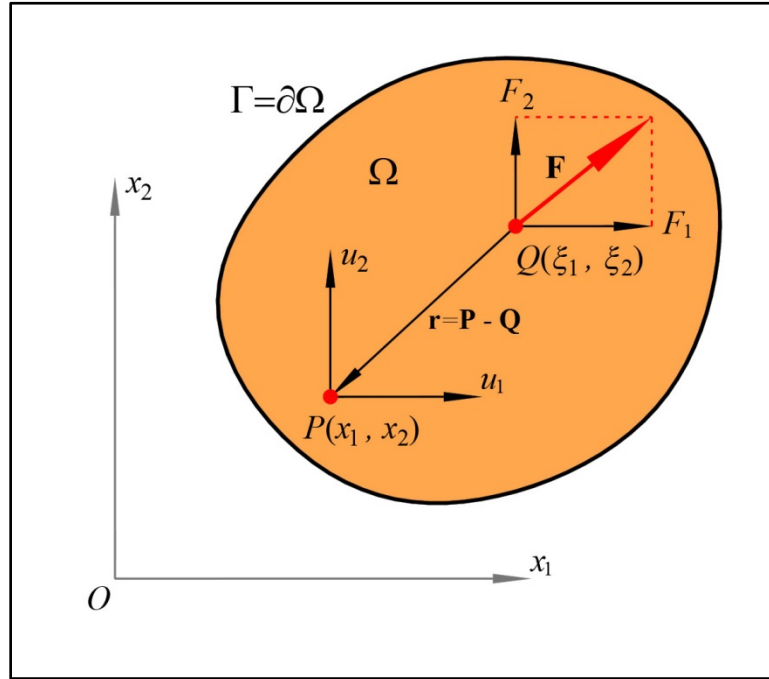


Figure 3.1—A Schematic of a 2D Elastic Body Subjected to a Force  $\mathbf{F}$  Exerted at Point  $Q$

If the dimension of the body along  $x_3$  is long enough, it can be inferred that,

$$\begin{cases} \varepsilon_{i3} = 0 \\ \sigma_{12} = \mu \varepsilon_{12} \\ \sigma_{13} = \sigma_{23} = 0 \end{cases} \quad (3.1)$$

It needs to be mentioned that the aim to assume a 2D plane-strain behavior is to reduce the volume of equations here. The process can, easily, be extended to General 3D linear elastic problem. The constitutive relation which dictates static equilibrium of the body is called Navier-Cauchy (or Navier-Lamé) Equation.

$$\begin{aligned}
\text{Indicial Form: } & u_{i,kk} + \frac{1}{1-2\nu} u_{k,ki} + \frac{F_i^b}{\mu} = 0 \\
\text{Classical Form: } & \nabla^2 \mathbf{u} + \frac{1}{1-2\nu} \nabla \nabla \cdot \mathbf{u} + \frac{\mathbf{F}^b}{\mu} = \mathbf{0}
\end{aligned} \tag{3.2}$$

As evident, Navier equation has a form of Partial Differential Equation. For the system to be in equilibrium, Equation (3.2) must satisfy a set of boundary conditions. Boundary conditions may be of type Essential or Geometrical (Dirichlet type). They may, also, be of type Natural or Force (Neumann type). Combination of these two types of boundary conditions is like the following.

$$\left\{ \begin{array}{l} \text{(i)} \quad u_1 = u_1^E, \quad u_2 = u_2^E \\ \text{(ii)} \quad u_1 = u_1^E, \quad t_2 = t_2^N \\ \text{(iii)} \quad t_1 = t_1^N, \quad u_2 = u_2^E \\ \text{(iv)} \quad t_1 = t_1^N, \quad t_2 = t_2^N \end{array} \right. \quad \text{on } \Gamma \tag{3.3}$$

Essential and Natural boundary condition types are specified by superscripts  $E$  and  $N$  respectively in Equation (3.3). In this equation,  $\mathbf{T} = t_i \mathbf{e}_i$  is a load (traction) on the whole or part of  $\Gamma$ .

The relation between essential boundary conditions and Navier equation is explicit. However, it is not the same for natural boundary conditions. It is possible by means of relation between stress components near the boundary and tractions.

$$t_i = \sigma_{ij} n_j \tag{3.4}$$

In Equation (3.4),  $\mathbf{n} = n_1 \mathbf{e}_1 + n_2 \mathbf{e}_2$  is a normal vector of the boundary  $\Gamma$  and  $n_i$  is a direction cosine of  $\mathbf{n}$ . By substituting Equation (2.11) in Equation (3.4), we have,

$$t_i = \lambda u_{j,j} n_i + \mu (u_{j,i} n_j + u_{i,k} n_k) \quad (3.5)$$

Note that,  $u_{i,k} n_k = \frac{\partial u_i}{\partial \mathbf{n}}$  is a directional derivative of the displacement component  $u_i$ .

### 3.1.1. Transformation to a Boundary Integral Equation

(Katsikadelis 2016; Youn 1993)

Before getting to a boundary integral equation, it is a good idea to briefly mention a well-known theorem called Maxwell-Betti Reciprocal Work Theorem or, in a shorter form, Reciprocal Identity. The foundation of the identity is based on state of stresses, tractions, body forces and strains in two separate states. Suppose state (P) in which the state of stresses and their resultant strains are  $\sigma_{ij}$  and  $\varepsilon_{ij}$  respectively, and likewise, State (Q) with  $\sigma_{ij}^*$  and  $\varepsilon_{ij}^*$ . Reciprocal Identity says that the work done by  $\sigma_{ij}$  as a result of  $\varepsilon_{ij}^*$  is the same as the work done by  $\sigma_{ij}^*$  as a result of  $\varepsilon_{ij}$  in an elastic domain  $\Omega$ . Hence,

$$\int_{\Omega} \sigma_{ij} \varepsilon_{ij}^* d\Omega = \int_{\Omega} \sigma_{ij}^* \varepsilon_{ij} d\Omega \quad (3.6)$$

Equation (3.6) can, also, be rewritten based of body forces, tractions and displacements based on two separate states. Therefore, we have:

$$\int_{\Omega} F_i^b u_i^* d\Omega + \int_{\Gamma} t_i u_i^* d\Gamma = \int_{\Omega} F_i^{b*} u_i d\Omega + \int_{\Gamma} t_i^* u_i d\Gamma \quad (3.7)$$

Hence,

$$\int_{\Omega} F_i^b u_i^* d\Omega - \int_{\Omega} F_i^{b*} u_i d\Omega = \int_{\Gamma} t_i^* u_i d\Gamma - \int_{\Gamma} t_i u_i^* d\Gamma \quad (3.8)$$



Body forces are obtained from Navier Equation. Therefore,

$$F_i^b = -\mu \left( u_{i,kk} + \frac{1}{1-2\nu} u_{k,ki} \right) \quad (3.9)$$

As mentioned above, a concentrated force  $\mathbf{F}$  is exerted to the elastic body in Figure 3.1. To take its effect into account, it is combined with body force by means of Dirac's Delta function as the following equation.

$$F_i^{bc} = \delta(\mathbf{r}) F_i \quad (3.10)$$

In this equation,  $F_i^{bc}$  means body force resulted by a concentrated Force. For the simplicity of the solution, it can be assumed a unit force  $|\mathbf{F}|=1$ . The best idea before obtaining the boundary integral equation, is to further simplify Navier Equation. One of the most well-known methods is to utilize Galerkin Vector  $\Phi = \phi_i \mathbf{e}_i$ . Components of Galerkin vectors are biharmonic if body force  $\mathbf{F}^b = F_i^b \mathbf{e}_i$  is a constant vector. Hence, we have,

$$\nabla^4 \phi_i = 0 \quad (3.11)$$

A particular solution to PDE in Equation (3.11) is,

$$\phi_i = -\frac{1}{8\pi(1-\nu)} F_i^{bc} r^2 \ln r \quad (3.12)$$

Now, a particular solution to obtain  $u_i$  is to substitute Equation (3.12) in the following equation.

$$\begin{aligned}
\text{Indicial: } 2\mu u_i &= \frac{1-\nu}{2} \phi_{i,jj} - (\phi_{j,j})_{,i} \\
&\text{or} \\
\text{Classical: } 2\mu u_i &= \frac{1-\nu}{2} \nabla^2 \phi_i - \frac{\partial}{\partial x_i} \left( \frac{\partial \phi_1}{\partial x_1} + \frac{\partial \phi_2}{\partial x_2} \right)
\end{aligned} \tag{3.13}$$

### 3.1.1.1. Displacement Field Components due to a Unit Concentrated Force

To reach to a boundary integral equation, we need to solve Equation (3.13) for separate cases as the following,

$$\text{Case 1: } \begin{cases} F_1^{bc} = 1 \\ F_2^{bc} = 0 \end{cases} \quad ; \quad \text{Case 2: } \begin{cases} F_1^{bc} = 0 \\ F_2^{bc} = 1 \end{cases} \tag{3.14}$$

For every case, we need to obtain  $u_i$ 's due to exertion of a unit force  $F_j^{bc} = 1$ . Remember the problem is of type 2D plane-strain, so  $i, j = 1$  or  $2$ . Therefore, we have a set of four equations in the form of  $U_{mn}$  which  $m, n = 1$  or  $2$ . The first index  $m$  is corresponding to direction of *displacement component* and the second index  $n$  is corresponding to direction of *unit force*. Based on Equations (3.12) to (3.14) we will have,

$$\begin{cases} U_{11} = -\frac{1}{8\pi\mu(1-\nu)} \left[ (3-4\nu) \ln r - \left( \frac{\partial r}{\partial x_1} \right)^2 + \frac{7-8\nu}{2} \right] \\ U_{21} = \frac{1}{8\pi\mu(1-\nu)} \left( \frac{\partial r}{\partial x_1} \cdot \frac{\partial r}{\partial x_2} \right) \\ U_{12} = \frac{1}{8\pi\mu(1-\nu)} \left( \frac{\partial r}{\partial x_1} \cdot \frac{\partial r}{\partial x_2} \right) = U_{21} \\ U_{22} = -\frac{1}{8\pi\mu(1-\nu)} \left[ (3-4\nu) \ln r - \left( \frac{\partial r}{\partial x_2} \right)^2 + \frac{7-8\nu}{2} \right] \end{cases} \tag{3.15}$$

In Equation (3.15) and all forthcoming equations,

$$\begin{cases} \frac{\partial r}{\partial x_1} = r_{,1} = -\frac{\xi_1 - x_1}{r} & \text{and} & \frac{\partial r}{\partial x_2} = r_{,2} = -\frac{\xi_2 - x_2}{r} \\ r = \sqrt{(\xi_1 - x_1)^2 + (\xi_2 - x_2)^2} \end{cases} \quad (3.16)$$

Equation (3.15) may, also, be rewritten in indicial form as,

$$U_{mn} = -\frac{1}{8\pi\mu(1-\nu)} \left[ \delta_{mn} (3-4\nu) \ln r - r_{,m} \cdot r_{,n} + \delta_{mn} \left( \frac{7-8\nu}{2} \right) \right] \quad (3.17)$$

Equation (3.17) is, indeed, components of a  $2 \times 2$  matrix as the following,

$$\mathbf{U}(P, Q) = \mathbf{U}(Q, P) = U_{mn} = \begin{bmatrix} U_{11} & U_{12} \\ U_{21} & U_{22} \end{bmatrix} \quad (3.18)$$

It is evident from Equation (3.15) that the matrix  $\mathbf{U}$  is symmetric. According to Figure 3.1, point  $P$  is observation point at which displacement, displacement derivative, and stresses are going to be computed. Point  $Q$  is the source point at which unit forces are going to be exerted. It can be inferred from Equation (3.15) that the role of these two points is exchangeable. It is one of the characteristics of Maxwell-Betti Reciprocal Work Theorem.

### 3.1.1.2. Stress Field components Due to a

#### *Unit Concentrated Force*

By means of Hooke's law mentioned in Equation (2.11) and substituting components from Equation (3.15) in it, stress components are obtained as following.

$$\left\{ \begin{array}{l}
\Sigma_{111} = -\frac{1}{4\pi(1-\nu)r} \left[ (1-2\nu) \frac{\partial r}{\partial x_1} + \left( \frac{\partial r}{\partial x_1} \right)^3 \right] \\
\Sigma_{221} = -\frac{1}{4\pi(1-\nu)r} \left[ -(1-2\nu) \frac{\partial r}{\partial x_1} + \left( \frac{\partial r}{\partial x_1} \right) \left( \frac{\partial r}{\partial x_2} \right)^2 \right] \\
\Sigma_{121} = -\frac{1}{4\pi(1-\nu)r} \left[ (1-2\nu) \frac{\partial r}{\partial x_2} + \left( \frac{\partial r}{\partial x_1} \right)^2 \left( \frac{\partial r}{\partial x_2} \right) \right] \\
\Sigma_{112} = -\frac{1}{4\pi(1-\nu)r} \left[ -(1-2\nu) \frac{\partial r}{\partial x_2} + \left( \frac{\partial r}{\partial x_1} \right)^2 \left( \frac{\partial r}{\partial x_2} \right) \right] \\
\Sigma_{222} = -\frac{1}{4\pi(1-\nu)r} \left[ (1-2\nu) \frac{\partial r}{\partial x_2} + \left( \frac{\partial r}{\partial x_2} \right)^3 \right] \\
\Sigma_{122} = -\frac{1}{4\pi(1-\nu)r} \left[ (1-2\nu) \frac{\partial r}{\partial x_1} + \left( \frac{\partial r}{\partial x_1} \right) \left( \frac{\partial r}{\partial x_2} \right)^2 \right]
\end{array} \right. \quad (3.19)$$

In Equation (3.19), stress components due to a unit point force are in the form of  $\Sigma_{ijk}$ . Indices  $i$  and  $j$  are component indicators, and the third index  $k$  is the indicator of unit force direction. Stress components in Equation (3.19) are rewritten in indicial form as following.

$$\Sigma_{ijk} = -\frac{1}{4\pi(1-\nu)r} \left[ (3-4\nu) (\delta_{ik} r_{,j} + \delta_{jk} r_{,i} - \delta_{ij} r_{,k}) + 2r_{,i} \cdot r_{,j} \cdot r_{,k} \right] \quad (3.20)$$

### 3.1.1.3. Boundary Traction components Due to a

#### *Unit Concentrated Force*

Equation (3.4) expresses the relation between internal stress components near boundary and components of the traction at the boundary. Since stress components are on hand in Equation (3.19), we are able to obtain equations for traction components due to a unit point force.

$$\left\{ \begin{array}{l}
T_{11} = -\frac{1}{4\pi(1-\nu)r} \left[ (1-2\nu) + 2 \left( \frac{\partial r}{\partial x_1} \right)^2 \right] \left( \frac{\partial r}{\partial x_1} n_1 + \frac{\partial r}{\partial x_2} n_2 \right) \\
T_{21} = -\frac{1}{4\pi(1-\nu)r} \left[ (1-2\nu) \left( -\frac{\partial r}{\partial x_1} n_2 + \frac{\partial r}{\partial x_2} n_1 \right) \cdots \right. \\
\left. + 2 \left( \frac{\partial r}{\partial x_1} \right) \left( \frac{\partial r}{\partial x_2} \right) \left( \frac{\partial r}{\partial x_1} n_1 + \frac{\partial r}{\partial x_2} n_2 \right) \right] \\
T_{12} = -\frac{1}{4\pi(1-\nu)r} \left[ -(1-2\nu) \left( -\frac{\partial r}{\partial x_1} n_2 + \frac{\partial r}{\partial x_2} n_1 \right) \cdots \right. \\
\left. + 2 \left( \frac{\partial r}{\partial x_1} \right) \left( \frac{\partial r}{\partial x_2} \right) \left( \frac{\partial r}{\partial x_1} n_1 + \frac{\partial r}{\partial x_2} n_2 \right) \right] \\
T_{22} = -\frac{1}{4\pi(1-\nu)r} \left[ (1-2\nu) + 2 \left( \frac{\partial r}{\partial x_2} \right)^2 \right] \left( \frac{\partial r}{\partial x_1} n_1 + \frac{\partial r}{\partial x_2} n_2 \right)
\end{array} \right. \quad (3.21)$$

Just like before, Equation (3.21) is written as indicial form. That is,

$$T_{ij} = -\frac{1}{4\pi(1-\nu)r} \left\{ \left[ (1-2\nu)\delta_{ij} + 2r_{,i} \cdot r_{,j} \right] r_{,k} n_k + (1-2\nu)(r_i n_j - r_j n_i) \right\} \quad (3.22)$$

#### 3.1.1.4. Final Step to express Integral form of the Solution

By Equations (3.15) and (3.21) on hand and imposing Betti-Maxwell Reciprocal Identity, an integral form of Navier equation is obtained. By imposing State (1) and, then, State (2) of the unit force mentioned in (3.14) in point  $Q$  of the Figure 3.1 we can get displacement components  $u_i$  at point  $P$ . It needs to me noted that, Point  $P$  is Field Point and Point  $Q$  is Source Point in our assumption. To represent the unit concentrated force, Dirac's Delta in Equation (3.10) has to be used, since Navier Equation (3.2) is established based on a body force distributed continuously in domain  $\Omega$ . Therefore,

$$\int_{\Omega} u_i^P (F_i^{bc})^Q = \int_{\Omega} u_i^P \delta(\mathbf{P}-\mathbf{Q})_i = u_i^Q \quad (3.23)$$

As evident from Equation (3.23), field point  $P$  has been switched to source point  $Q$  which is the characteristic of Reciprocal Identity. In other words, point  $Q$ , now, is field point and point  $P$  is source point. It can be inferred that; field points and source points are interchangeable. As mentioned above, a unit concentrated force was exerted to a source point. To obtain displacement field due to a distributed body force and/or distributed traction, the Integral of Equation (3.23) through the domain  $\Omega$  and boundary  $\partial\Omega = \Gamma$  needs to be computed. Therefore,

$$\begin{aligned}
\begin{Bmatrix} u_1^P \\ u_2^P \end{Bmatrix} &= \int_{\Omega} \begin{bmatrix} U_{11} & U_{12} \\ U_{12} & U_{22} \end{bmatrix} \begin{Bmatrix} (F_1^B)^Q \\ (F_2^B)^Q \end{Bmatrix} d\Omega_Q \\
&+ \int_{\Gamma} \begin{bmatrix} U_{11} & U_{12} \\ U_{12} & U_{22} \end{bmatrix} \begin{Bmatrix} t_1^q \\ t_2^q \end{Bmatrix} d\Gamma_q \\
&- \int_{\Gamma} \begin{bmatrix} T_{11} & T_{12} \\ T_{21} & T_{22} \end{bmatrix} \begin{Bmatrix} u_1^q \\ u_2^q \end{Bmatrix} d\Gamma_q
\end{aligned} \tag{3.24}$$

Note that  $q \in \Gamma$  and  $Q \in \Gamma$ . In Equation (3.24), the components  $U_{ij}$  and  $T_{ij}$  are the same as Equations (3.15) and (3.21) respectively. Equation (3.24), in a short indicial form, is rewritten as,

$$u_i^P = \int_{\Omega} U_{ji} F_j^B d\Omega + \int_{\Gamma} (U_{ji} t_j - T_{ji} u_j) d\Gamma \tag{3.25}$$

The above integral is singular when source and field points are the same. Moreover, when field point is at the boundary, Equation (3.25) becomes singular. It is proven that,

$$\alpha_{ij} u_i^P = \int_{\Omega} U_{ji} F_j^B d\Omega + \int_{\Gamma} (U_{ji} t_j - T_{ji} u_j) d\Gamma \tag{3.26}$$

Where for the case of smooth boundary,  $\alpha_{ij} = \frac{1}{2} \delta_{ij}$ . Equation (3.26) is the Integral Equation of the problem.

### 3.1.1.5. Integral Equations of the Stress Components

The equations to compute stress components at field points can be derived by means of Hooke's law in Equation (2.11), displacement components in Equation (3.24), and stress components in Equation (3.19). Thus, we have,

$$\left\{ \begin{array}{l} \sigma_{11} = \int_{\Omega} (\Sigma_{111} F_1^b + \Sigma_{112} F_2^b) d\Omega + \int_{\Gamma} (\Sigma_{111} t_1 + \Sigma_{112} t_2) d\Gamma \cdots \\ \quad - \int_{\Gamma} (\bar{\Sigma}_{111} u_1 + \bar{\Sigma}_{112} u_2) d\Gamma \\ \sigma_{22} = \int_{\Omega} (\Sigma_{221} F_1^b + \Sigma_{222} F_2^b) d\Omega + \int_{\Gamma} (\Sigma_{221} t_1 + \Sigma_{222} t_2) d\Gamma \cdots \\ \quad - \int_{\Gamma} (\bar{\Sigma}_{221} u_1 + \bar{\Sigma}_{222} u_2) d\Gamma \\ \sigma_{12} = \int_{\Omega} (\Sigma_{121} F_1^b + \Sigma_{122} F_2^b) d\Omega + \int_{\Gamma} (\Sigma_{121} t_1 + \Sigma_{122} t_2) d\Gamma \cdots \\ \quad - \int_{\Gamma} (\bar{\Sigma}_{121} u_1 + \bar{\Sigma}_{122} u_2) d\Gamma \end{array} \right. \quad (3.27)$$

In indicial form, Equation (3.27) becomes,

$$\sigma_{ij} = \int_{\Omega} \Sigma_{ijk} F_k^b d\Omega + \int_{\Gamma} \Sigma_{ijk} t_k d\Gamma - \int_{\Gamma} \bar{\Sigma}_{ijk} u_k d\Gamma \quad (3.28)$$

In Equation (3.28),  $\Sigma_{ijk}$  are mentioned in Equation (3.19). Furthermore,  $\bar{\Sigma}_{ijk}$  are the following.

$$\left. \begin{aligned}
\bar{\Sigma}_{111} &= -\frac{2\mu}{4\pi(1-\nu)r^2} \left\{ \begin{aligned} &2\left(\frac{\partial r}{\partial x_1}\right)\left(\frac{\partial r}{\partial x_1}n_1 + \frac{\partial r}{\partial x_2}n_2\right)\left[1-4\left(\frac{\partial r}{\partial x_1}\right)^2\right]\dots \\ &+ \left[2\left(\frac{\partial r}{\partial x_1}\right)^2 + 1\right]n_1 \end{aligned} \right\} \\
\bar{\Sigma}_{112} &= -\frac{2\mu}{4\pi(1-\nu)r^2} \left\{ \begin{aligned} &-8\left(\frac{\partial r}{\partial x_1}\right)^2\left(\frac{\partial r}{\partial x_2}\right)\left(\frac{\partial r}{\partial x_1}n_1 + \frac{\partial r}{\partial x_2}n_2\right)\dots \\ &+ 2\left(\frac{\partial r}{\partial x_1}\right)\left(\frac{\partial r}{\partial x_2}\right)n_1 + n_2 \end{aligned} \right\} \\
\bar{\Sigma}_{221} &= -\frac{2\mu}{4\pi(1-\nu)r^2} \left\{ \begin{aligned} &-8\left(\frac{\partial r}{\partial x_2}\right)^2\left(\frac{\partial r}{\partial x_1}\right)\left(\frac{\partial r}{\partial x_1}n_1 + \frac{\partial r}{\partial x_2}n_2\right)\dots \\ &+ 2\left(\frac{\partial r}{\partial x_1}\right)\left(\frac{\partial r}{\partial x_2}\right)n_2 + n_1 \end{aligned} \right\} \\
\bar{\Sigma}_{222} &= -\frac{2\mu}{4\pi(1-\nu)r^2} \left\{ \begin{aligned} &2\left(\frac{\partial r}{\partial x_2}\right)\left(\frac{\partial r}{\partial x_1}n_1 + \frac{\partial r}{\partial x_2}n_2\right)\left[1-4\left(\frac{\partial r}{\partial x_2}\right)^2\right]\dots \\ &+ \left[2\left(\frac{\partial r}{\partial x_2}\right)^2 + 1\right]n_2 \end{aligned} \right\} \\
\bar{\Sigma}_{121} &= \bar{\Sigma}_{112} \\
\bar{\Sigma}_{122} &= \bar{\Sigma}_{221}
\end{aligned} \right\} \quad (3.29)$$

### 3.1.2. Discretization of the Boundary Integral Equations

The boundary integral equations (3.26), and (3.29) are applicable to solve a simple 2D plane-strain problem. Therefore, its application is so limited. In order to use the abovementioned Boundary Integral Equations to solve a general 2D plane-strain problem with arbitrary domain geometry and boundary conditions, both  $\Omega$  and  $\Gamma$  have to be discretized. Discretization can help us approximate integrals numerically. If the boundary



is discretized into  $N$  separate elements, for every Boundary Element  $i$ , Equation (3.26) may be rewritten as,

$$\frac{1}{2} \mathbf{u}_i + \sum_{j=1}^N \hat{\mathbf{K}}^{ij} \mathbf{u}_j = \sum_{j=1}^N \mathbf{G}^{ij} \mathbf{t}_j + \mathbf{F}_i \quad (3.30)$$

Where,

$$\mathbf{u}_i = \{u_1^i \quad u_2^i\}^T \quad ; \quad \mathbf{t}_i = \{t_1^i \quad t_2^i\}^T \quad (3.31)$$

$$\hat{\mathbf{K}}^{ij} = \begin{bmatrix} \int_{\Gamma_j} T_{11}(q, p_i) ds_q & \int_{\Gamma_j} T_{21}(q, p_i) ds_q \\ \int_{\Gamma_j} T_{12}(q, p_i) ds_q & \int_{\Gamma_j} T_{22}(q, p_i) ds_q \end{bmatrix} \quad (3.32)$$

$$\mathbf{G}^{ij} = \begin{bmatrix} \int_{\Gamma_j} U_{11}(q, p_i) ds_q & \int_{\Gamma_j} U_{21}(q, p_i) ds_q \\ \int_{\Gamma_j} U_{12}(q, p_i) ds_q & \int_{\Gamma_j} U_{22}(q, p_i) ds_q \end{bmatrix}$$

And,

$$\mathbf{F}^i = \left\{ \begin{array}{l} \int_{\Omega} (U_{11}(Q, p_i) F_1^b(Q) + U_{21}(Q, p_i) F_2^b(Q)) d\Omega_Q \\ \int_{\Omega} (U_{12}(Q, p_i) F_1^b(Q) + U_{22}(Q, p_i) F_2^b(Q)) d\Omega_Q \end{array} \right\} \quad (3.33)$$

To distinguish whether field or source point is in domain or boundary, we denote them by uppercase or lowercase letters respectively. That is,  $p, q \in \Gamma$  and  $P, Q \in \Omega$ .

By applying, Equation (3.30) to all boundary elements, we end up to a system of  $2 \times N$  linear equations as following.

$$\mathbf{K}\mathbf{u} = \mathbf{G}\mathbf{t} + \mathbf{F} \quad ; \quad \mathbf{K} = \hat{\mathbf{K}} + \frac{1}{2}\mathbf{I} \quad (3.34)$$

All known and unknown displacements and tractions at the boundary need to be rearranged to facilitate the numerical process. By solving the system of linear equation in (3.34) we will have  $2 \times N$  known displacements and tractions at the boundary. By having all those variables, all unknown displacements and stresses in domain can be obtained easily. It is noted that to get the components of matrices  $\mathbf{K}$  and  $\mathbf{G}$  and vector  $\mathbf{F}$ ,  $2 \times 2N \times 2N + 2N = 8N^2 + 2N$  integrations are required. Depending on interpolation functions, all functions have to be computed in Gauss integration points and then combined by their corresponding weights. Since matrices  $\mathbf{K}$  and  $\mathbf{G}$  are symmetric, the number of numerical integrations can be reduced to  $N(2N + 3)$ . To reach a relatively accurate results, if using lower number of Gauss integration points, the number of boundary elements,  $N$ , have to be increased significantly.

### 3.1.3. Calculation of displacement Field Components

#### at Interior Field Points

Now that all the unknown displacement field components in the boundary are at hand by solving Equation (3.34), we are able to compute them at any interior field points as well.

$$\mathbf{u}^i = \sum_{j=1}^n \mathbf{G}^{ij} \mathbf{t}^j - \sum_{j=1}^n \hat{\mathbf{K}}^{ij} \mathbf{u}^j + \mathbf{F}^i \quad (3.35)$$

In Equation (3.35),  $\mathbf{t}^j$  and  $\mathbf{u}^j$  are known. However, to compute  $\mathbf{G}^{ij}$  and  $\hat{\mathbf{K}}^{ij}$ , and  $\mathbf{F}^i$  Equations (3.32) and (3.39) are used based of coordinates of the field point. In other words, they have to be recalculated for each and every field point.

### 3.1.4. Calculation of Stress Components

#### at Interior Field Points

Stress field components are computed by the following equation. Note that,  $\mathbf{t}^j$  and  $\mathbf{u}^j$  are known, now.

$$\sigma_{mn}^i = \sum_{j=1}^n \Sigma_{mnk}^i t_k^j - \sum_{j=1}^n \bar{\Sigma}_{mnk}^i u_k^j + \int_{\Omega} \Sigma_{mnk}^{\Omega} F_k^b d\Omega \quad (3.36)$$

In Equation (3.36), parameters  $\Sigma_{mnk}^i$  and  $\bar{\Sigma}_{mnk}^i$  are computed based on field point coordinates and Equations (3.29), however, third term is a domain integral. So,  $\Sigma_{mnk}^{\Omega}$  has to be calculated for all field points in the domain.

### 3.1.5. Converting domain integrals to boundary integrals

It is evident in Equations (3.28), (3.33), and (3.36) that some of the integrals are still domain integrals. Therefore, both domain and boundary shall be discretized. Discretization of both domain and boundary of the elastic medium, impacts the performance of the method. The major goal in BEM is to limit numerical analysis procedure in the boundary and avoid volume integrals. One method to do so is to use Potential function which is, sometimes, called Harmonic function. If body force field is of type Gravitational, it follows the property of Harmonic function.

$$\nabla^2 V = 0 \quad (3.37)$$

Thus, body force can be rewritten as,

$$F_i^b = \frac{\partial V}{\partial x_i} = V_{,i} \quad (3.38)$$

It can be proven that domain integral (3.33), can be converted to the following form.

$$\mathbf{F}^i = \left\{ \begin{array}{l} \frac{1-2\nu}{4\pi(1-\nu)\mu} \int_{\Gamma} [V\phi_{,1k}n_k - \phi_{,1}V_{,k}n_k + U_{k1}n_k] ds \\ \frac{1-2\nu}{4\pi(1-\nu)\mu} \int_{\Gamma} [V\phi_{,2k}n_k - \phi_{,2}V_{,k}n_k + U_{k2}n_k] ds \end{array} \right\} \quad (3.39)$$

In Equation (3.39),  $k$  is an indicial notation and  $\phi$  is a Galerkin vector,  $\phi = \frac{1}{4}r^2 \ln r$ .

## 3.2. Boundary Element Method Based on

### Okada Formulation

A classical Boundary Element Method was discussed in Section 3.1. by an example of an elastic Two-Dimensional plane-strain problem which represented by famous Navier-Cauchy partial differential equation. Then, the governing PDE was converted to a set of boundary integral forms by means of Maxwell-Betti Reciprocal Identity to obtain relations between known displacements, tractions, and body forces with unknown displacement and stress fields in elastic domain and its boundaries. Since the boundary integral equations were limited to a very simple known conditions, they were discretized both in domain and

boundary to generalize the solution to virtually any given conditions. Finally, to improve performance of the solution, all domain integral equations were converted to equivalent boundary integral equations. This conversion is necessary in presence of body forces distributed in the volume of the body, in whole or in part. If the effect of body forces is seemed to be negligible, the final part can be canceled out. Like other methods, the explained BEM, is a numerical approximation to a real problem. Therefore, to achieve results within an acceptable range, the number of discretizations (size of BEs) has to be adjusted. To obtain stiffness and traction matrices  $\mathbf{K}$  and  $\mathbf{G}$ ,  $N(2N+3)$  or  $N(2N+1)$  numerical integrations, with or without presence of body forces, are required for a 2D problem. For general 3D problems, they will be  $\frac{9N(N+1)}{2}$  or  $\frac{3N(3N+1)}{2}$  respectively.

Gauss Integration is used most often. Each integration, based on the number of Gauss integration points, needs several arithmetic operations by computers. The most laborious part of abovementioned equations is to compute  $\ln r$  at Gauss integration points which needs Taylor expansion.

### 3.2.1. Philosophy of the Method

It is useful to develop a boundary element method which does not need numerical integration. Since Okada proposed a closed-form solution to a finite rectangular dislocation problem, its exact functions can be used as interpolation functions. Conventional BEM discussed above can also produce exact results for finite rectangular source. Our proposed method is a specific type of sub-parametric formulation, since the order of functions to interpolate fracture geometry is zero, however, the order of functions in Table 2.3 to Table 2.6 can mathematically be assumed infinity in terms of Taylor

expansion. Our method is new-of-a-kind, since no research article has been published which is similar to it.

### 3.2.2. Description of the Method

As mentioned above, Okada's solution is valid for a single rectangular discontinuous source, however in reality, hydraulic fractures may have complicated geometries especially when it comes to model natural fractures and faults. Moreover, hydraulic fractures initiate from a small perforated spot in boreholes and when fluid injection pressure is increasing the reservoir rock around perforation begins to fail. By the initiation of rock failure, an initial fracture plane is created. When fluid injection pressure is increasing continuously, hydraulic fracture propagates. Therefore, all the fractures (hydraulic, natural, faults, etc.) shall be discretized. The approximation of the fracture geometry is going to be carried out by simple rectangular boundary elements. In this study, penny-shaped (circular) and rectangular fractures are going to be simulated. Since the reservoir rock is assumed linear elastic, Superposition rule can be applied to obtain system of equilibrium equations. By separately analyzing a HF domain with on-by-one of those RABEs and, then, combining all the analysis results we expect to achieve a final result which approximates the ideal result. And, we believe by increasing the number of RABEs the numerical results will approach and converge to an ideal model, i.e., better approximation of a fracture geometry ends up to better approximation of analysis results. our workflow is so simple. It is summarized as below.

1. Discretize an either single/multiple fractures by having all required data on hand.
2. Define a grid of field point (grid-nodes) throughout the reservoir. Grid-nodes are essentially independent from fracture meshes, but matching grid-nodes with

RABE meshes is recommended. Grid-nodes in the vicinity of RABEs have to be at middle point of them. The reason is discussed in section 3.2.3. It improves the quality of graphical illustrations. The grid of field nodes can, also be modified after fracture dislocation analysis in next steps.

3. Compute components of the stiffness matrix for each and every RABEs.
4. Pressurize the fracture model. Generally, fault/fracture walls are not smooth and might have cohesive sediments such as calcite. Any amount of slip might create cohesion/friction. Now, Obtain Load matrix for each and every RABEs
5. Assemble all matrices and vectors to get the system of equilibrium equation as (3.34).
6. Analyze the system of equilibrium equation to obtain dislocations in each of the RABEs.
7. By having all RABE dislocations at hand, analyze displacement field components due to each of the dislocation components obtained from step 6 at grid-nodes and apply superposition.
8. If necessary, modify the field grid. Increase/decrease density of the nodes. Or change distribution. Grid-Node distribution may be uniform, exponential, or logarithmic. For instance, grid-nodes near fracture tips can be denser due to dramatic gradient of parameters.
9. Compute Cauchy Strain Tensor, Cauchy Stress Tensor, Principal Stresses, Principal Directions by DDDv components at all grid-nodes. As a preliminary failure criteria, Maximum Shear Stresses, and Maximum Shear Directions in a defined Grid-nodes will be analyzed.

10. Due to high volume of analysis data, illustrate all above-mentioned parameters graphically.
11. If results are acceptable it is done. If not, go to Step 1 and modify shape and size of RABEs and/or field grid.

The abovementioned steps are summarized in the following flowchart.

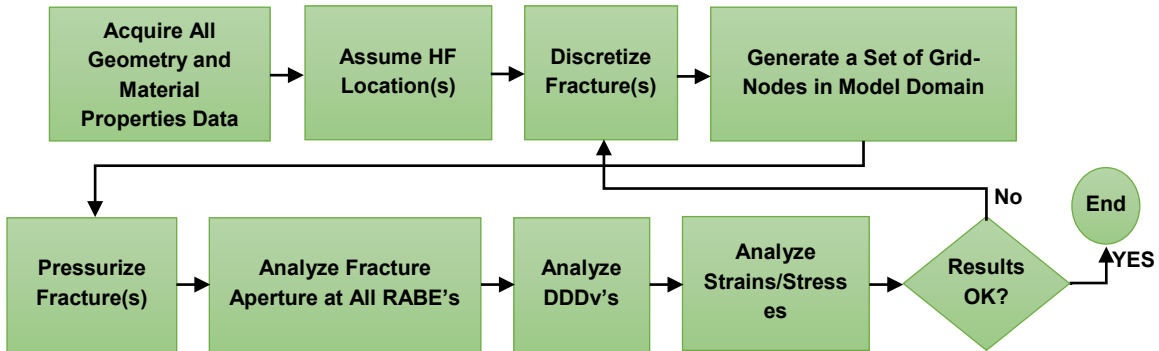


Figure 3.2—Workflow of the BEM Simulation

### 3.2.3. Representation of System of Equilibrium Equation

According to Figure 3.2, first parameter(s) to obtain is *fracture aperture* for each of the RABEs. We also call it dislocation(s). To compute dislocation components we need stiffness matrix  $\mathbf{K}$  and  $\mathbf{G}$  which was mentioned in Equation (3.34). In most research articles, body force is not the case and can be neglected. So, we don't need to obtain vector  $\mathbf{F}$ . Since it is assumed that pressure, cohesion, or friction on fracture face is constant, matrix  $\mathbf{G}$  will be an Identity matrix. But the major obstacle is to compute matrix  $\mathbf{K}$ . Our method to compute matrix  $\mathbf{K}$  is to apply unit dislocation  $U_k^m = 1$  to iDOF in RABE  $m$ . therefore,  $\mathbf{m}$  is the identifier of RABE and  $m = 1, 2, 3, \dots, n\text{RABE}$ . The index  $k$ , however, is 1 for SSL, 2 for DSL, and 3 for TL dislocation types. Therefore,  $n\text{DOF} = 3 \times n\text{RABE}$ . Some of these degrees of freedom can be constrained if we decide, but it is



recommended that all of DOFs remain open. But to obtain matrix  $\mathbf{K}$ , superposition rule dictates that all DOFs become constrained except for  $U_k^m = 1$ , i.e., all RABEs must be kept inactive except for one. To keep all-but-one RABEs closed and inactive, a stress must be exerted because they are active in reality. Exerted stresses to all-but-one RABEs will keep them closed. Moreover, the stress to have a unit dislocation at iDOF has to be computed as well. All the exerted stress components to keep all-but-one RABEs inactive can be computed by Equations, (2.8), (2.10), and (2.11). The exerting stress on RABE  $m$  to create unit dislocation  $U_k^m = 1$  can, also, be computed by the same equations. Figure 3.3 illustrates a schematic of an arbitrary HF with two RABEs  $m$  and  $n$ . RABE  $m$  experiences a unit TL dislocation that creates stresses in the vicinity of both RABEs.

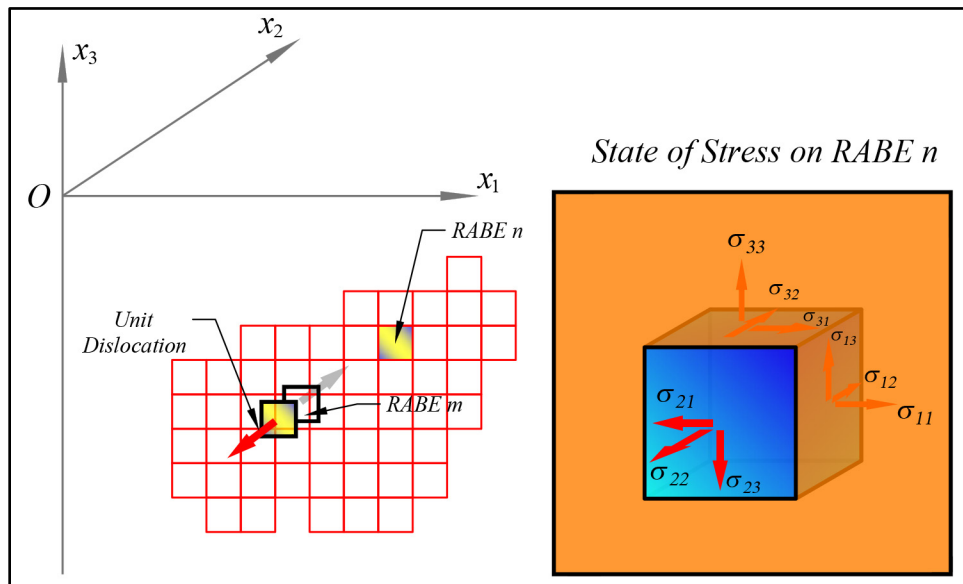


Figure 3.3—A Schematic of a discretized HF. In this figure,  $m$ th RABE undergoes a unit TL dislocation. It generates stress in the same RABE and  $n$ th RABE

The state of stress in the vicinity of the RABE faces are, also, depicted in Figure 3.3. It needs to be mentioned that, stress components in the vicinity of RABE faces are not

uniform. To get better results, average of stresses can be computed. But it is so time-consuming and makes our method disadvantageous with respect to other methods. To overcome this problem, we assume average of stresses is at the middle point of the RABEs. Although inexact, the assumption can come true by reducing the size of the RABE. By redoing the process to all DOFs we will have all required stress components. Now, fluid injection pressure or possible frictions/ cohesions (tractions) at fracture face and internal stress components in the vicinity of the fracture face due to SSL, DSL, and TL dislocations must be in equilibrium in the open iDOF in RABE  $m$ . Equilibrium Equation (3.5), now, is rewritten as,

$$\left(\sigma_{in-situ}\right)_j + \sigma_{ij}^m \nu_j - p_j = 0 \quad (3.40)$$

In Equation (3.40),  $\left(\sigma_{in-situ}\right)_1 = S_{H \max}$ ,  $\left(\sigma_{in-situ}\right)_2 = S_{H \min}$ , and  $\left(\sigma_{in-situ}\right)_3 = \text{Overburden stress}$ . They are, indeed, far-field stress components. In addition,  $\sigma_{ij}^m$  is components of Cauchy stress at mid-surface of RABE  $m$ . Moreover,  $p_j$  is force per unit area that can be due to friction/cohesion or injection pressure. Some useful information such as our convention for positive stress are illustrated in Figure 3.3. Remember that these stresses can be negative in Equation (3.40). For example,  $\sigma_{22}$  in Figure 3.3 is positive (tension stress) but it does not comply with positive  $x_2$  direction and, hence, is negative in above equation. Now, by all stress components at hand, we may release all RABEs. Since the system is assumed linear, all the strains and stresses are proportional to dislocation values. If we apply arbitrary dislocation values  $U_k^n$  to all DOFs, we can obtain stress components at any DOF. For example,

$$\begin{aligned}
\sigma_{ij}^m = & \sigma_{ij}^{m-1-1} U_1^1 + \sigma_{ij}^{m-1-2} U_2^1 + \sigma_{ij}^{m-1-3} U_3^1 \\
& + \sigma_{ij}^{m-2-1} U_1^2 + \sigma_{ij}^{m-2-2} U_2^2 + \sigma_{ij}^{m-2-3} U_3^2 + \dots \\
& + \sigma_{ij}^{mnk} U_k^n + \dots \\
& + \sigma_{ij}^{m-NBE-k} U_k^{NBE}
\end{aligned} \tag{3.41}$$

In this equation,  $\sigma_{ij}^{mnk}$  is a stress component at midpoint of RABE  $m$  due to unit dislocation in  $k$ th DOF of RABE  $n$ . By substituting Equation (3.41) in (3.40) we get,

$$k_{pq} U_q = P_q - (\sigma_{in-situ})_q = \Delta P_q \tag{3.42}$$

Indices  $p$  and  $q$  are indicial notations. Equation (3.42) in matrix form is represented as,

$$\mathbf{K}\mathbf{U} = \mathbf{P} - \boldsymbol{\sigma}_{in-situ} = \Delta\mathbf{P} \tag{3.43}$$

Equation (3.43) is similar to equilibrium equation in Finite Element or other numerical Methods. Components of stiffness matrix  $k_{pq}$  are stress values in DOF  $p$  due to unit dislocations at DOF  $q$ . Stiffness component  $k_{pp}$  which relies at diagonal of stiffness matrix is stress value required to create unit dislocation in DOF  $p$ . Vector  $\mathbf{U}$  comprises dislocation at DOF  $q$  which is unknown. Vector  $\mathbf{P}$  consists of cohesions/ frictions and injection pressure at fracture surface. Vector  $\boldsymbol{\sigma}_{in-situ}$ , has in-situ stress values at DOF  $q$ .

The effective load which opens the fracture is  $\Delta\mathbf{P}$ . If fluid injection pressure is less than minimum in-situ stress, fracture aperture will remain zero. Moreover, if shear stress is less than cohesion, no SSL or DSL dislocation will happen. In our model, DOF<sub>1</sub> to DOF<sub>3</sub> in RABE  $m$  correspond to SSL, DSL, and TL dislocation types respectively. By solving the system of linear equations in Equation (3.43), all the values of dislocation will

be obtained. It is a good idea to remember famous Betti-Maxwell theorem. In Theory of Elasticity. The Maxwell-Betti Reciprocal Work theorem dictates that stiffness matrix  $\mathbf{K}$ , become symmetric. If for any reason, the matrix  $\mathbf{K}$  is not symmetric, the system is unstable. So, this property is one of the criteria to verify the integrity and correctness of the process.

### **3.2.4. Analysis of Displacement and Displacement**

#### Derivative Fields

By solving the system of equilibrium equation (3.43), all the values of dislocations in active degrees of freedom will be obtained. Having dislocation values, functions in Table 2.3 to Table 2.6, and Equations (2.7) to (2.10) will give us a path to compute DDDv field components at any point away from locus of singularities discussed in section 2.5. . Since the domain is linear elastic, all components obtained from each and every dislocation component can be combined linearly.

### **3.2.5. Analysis of Strain and Stress**

Since displacement derivative field components are available, all the strain components are computed at any grid-node by means of Equation (2.11). Equations (2.11) and (2.13), along with strain components, will result stress components at any field point generated by a grid in the domain.

### **3.2.6. Analysis of Principal Strains, Principal**

#### Stresses, and their directions

Both strain and stress follow tensor properties. So, there are always three planes with strain/stress components perpendicular to them. In other words, there will be no

shearing strain/stress components on those planes. These normal strain/stress components are called principal strains/stresses. The corresponding normal vectors of those planes are called principal directions. In the presence of in-situ stresses, principal directions for strain and stress may be different, since in-situ stresses are far-field stresses and don't create strains. Strains are generated in the reservoir due to its disturbance such as hydraulic fracturing. To obtain principal values and directions, eigenpair analysis of strain and stress tensors are required. That is,

$$\boldsymbol{\varepsilon} \mathbf{n}_i^\varepsilon = \varepsilon_i \mathbf{n}_i^\varepsilon \quad \text{and} \quad \boldsymbol{\sigma} \mathbf{n}_i^\sigma = \sigma_i \mathbf{n}_i^\sigma \quad (3.44)$$

Here in Equation (3.44),  $i$  is not an indicial notation. Both strain and stress tensors have three distinct eigenpairs (eigenvalues and eigenvectors). There are numerous methods to get eigenpairs. However, for our study, Jacobian Iterative method is suitable.

### 3.2.7. Analysis of Maximum Shearing Strain and Stress and their corresponding directions

Maximum shearing strains and maximum shearing stresses take place in a plane passing normal vectors corresponding to minimum and maximum principal strains and stresses. The values of maximum shearing strain and stress is as the following.

$$\begin{cases} \gamma_{\max} = \frac{1}{2} [(\varepsilon_p)_{\max} - (\varepsilon_p)_{\min}] \\ \tau_{\max} = \frac{1}{2} [(\sigma_p)_{\max} - (\sigma_p)_{\min}] \end{cases} \quad (3.45)$$

There are two perpendicular directions for maximum shearing strain and stress. One of them is bisector of normal vectors corresponding to maximum and minimum principal values, and the other one is perpendicular to that. So,

$$\begin{cases} \mathbf{n}_\gamma = \frac{1}{\sqrt{2}} [\mathbf{n}_{p_{\max}}^\varepsilon - \mathbf{n}_{p_{\min}}^\varepsilon] & \text{or } \mathbf{n}_\gamma = \frac{1}{\sqrt{2}} [\mathbf{n}_{p_{\max}}^\varepsilon + \mathbf{n}_{p_{\min}}^\varepsilon] \\ \mathbf{n}_\tau = \frac{1}{\sqrt{2}} [\mathbf{n}_{p_{\max}}^\sigma - \mathbf{n}_{p_{\min}}^\sigma] & \text{or } \mathbf{n}_\tau = \frac{1}{\sqrt{2}} [\mathbf{n}_{p_{\max}}^\sigma + \mathbf{n}_{p_{\min}}^\sigma] \end{cases} \quad (3.46)$$

Assessing and Understanding Maximum shearing strain and maximum shearing stress fields is helpful to approximately estimate and localize rock failure and find their orientations. It is obvious that more comprehensive failure analysis is required, because rock failure is complicated in nature. Other factors can influence rock failure such as poro-elastic transitions, thermo-elastic effects, presence of micro-fractures and so on (Huang et al. 2013).

### 3.3. Comparison of the classical BEM to Our Proposed BEM

As explained in both sections 3.1. and 3.2. in order to reach an acceptable approximation of a model, the boundary of the model domain has to be discretized into smaller elements. To obtain the system of equilibrium equation for a 2D problem in *classical method* at least  $N(2N+1)$  often numerical integration is required. For a 3D problem (without presence of body forces), this number will be  $\frac{3N(3N+1)}{2}$ . Moreover, to compute displacement field and stress field components at an interior field point, according to Equations (3.35) and (3.36), 20 additional integrations are required. Since if integrations are carried out numerically (let say Gauss integration), the value of all

abovementioned complicated functions has to be computed at Gauss integration points. The minimum recommended number of integration points for 1D and 2D boundary elements is at least 3 and 8 respectively (Youn 1993).

In this work, numerical integration is not needed. Moreover, our method needs fewer number of discretizations; therefore, it can reduce the rank of stiffness matrix  $\mathbf{K}$  and analyze a model much faster. Based on functions in Table 2.3 to Table 2.6 and Appendix A, the only laborious and time-consuming factor which can impact performance of our method is calculation of functions  $\sin \delta$ ,  $\cos \delta$ ,  $\ln(R + \xi)$ ,  $\ln(R + \eta)$ , and  $\ln(R + \tilde{d})$ . These functions need Taylor expansion to be calculated accurately by computers. These functions need to be calculated twice; one for real source and the other for image source.

Figure 3.4 depicts the difference between boundary element shapes for our method and other classical methods. It is clear that with classical methods, geometry of a field boundary can be approximated better.

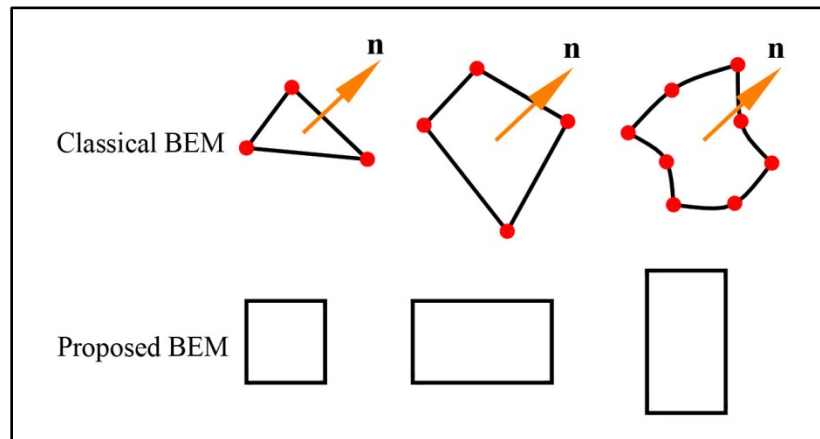


Figure 3.4—Comparison of Boundary Element Shapes

Another major advantage of our method is that the utilized formulation already includes half-space condition of the boundaries, therefore the accuracy of the model is totally independent from size and extent of the domain encompassing the hydraulic fracture(s) we choose. However, classical BEMs still need modeling of the boundary surrounding the domain in addition to fracture(s). For a classical BEM to be satisfactory, the surrounding boundary shall be large and, also, far enough from main boundaries (fractures). Selecting a large domain and its surrounding boundary, needs quite larger number of boundary elements which tremendously increases the rank of stiffness matrix **K**.



# CHAPTER 4. Implementation of the BEM in a Computer Code

In this chapter, a computer program is developed in FORTRAN90 and compiled by Intel® Parallel Studio XE 2019 update 4. We call our simulator HiFrac 3D. Our model is capable to model both 2D and 3D fractures as shown below.

## 4.1. Discretization of a Fracture

Currently, only horizontal or vertical fractures can be treated. Moreover, according to Figure 2.3, local  $x$ -axis is, always, parallel to global  $x_1$ -axis. More developments are required to overcome these limits.

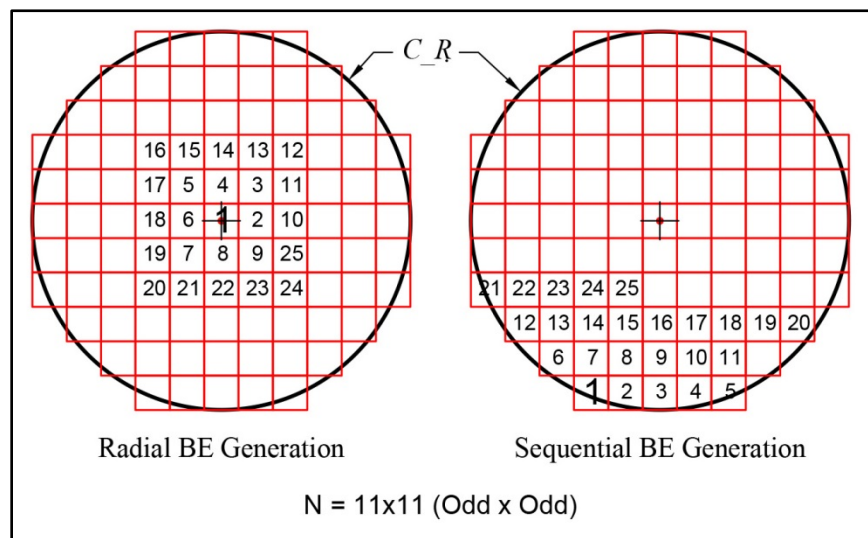


Figure 4.1—Radial and Sequential BE Mesh Generation in a Penny-Shaped Fracture

To model a penny-shaped fracture, all we need is coordinates of its center in a global Cartesian frame and the radius. There are two ways to generate boundary elements,

sequential or radial. The difference is illustrated in Figure 4.1. Although sequential method is very easy, but we prefer the radial method. The radial method has a difficult algorithm especially in terms of number of discretization in both  $x$ - and  $y$ - directions. Depending on whether discretization is  $\text{Odd} \times \text{Odd}$  ,  $\text{Odd} \times \text{Even}$  ,  $\text{Even} \times \text{Odd}$  , or  $\text{Even} \times \text{Even}$  , the algorithms are slightly different. The reason to choose this method is that it makes stiffness matrix organized, so that larger values are located around the diagonal of the matrix, and the smaller influences farther from diagonal. In addition, by adding fracture propagation capability to simulator, more boundary elements need to be added automatically to the model. Therefore, the size of stiffness matrix will increase both in row and column directions. Since, mesh generation is radial, the stiffness matrix will grow in size from the right and bottom edges and adding rows and columns between existing ones won't be required. Therefore, radial mesh generation method will make simulator development in future a lot easier.

Mesh generation for a rectangular fracture is so similar to that of penny-shaped one, except for the condition to when/where to change BE row or BE column. Instead of radius, this shape needs half-length in both  $x$ - and  $y$ - directions. Two methods for generate mesh are shown in Figure 4.2.

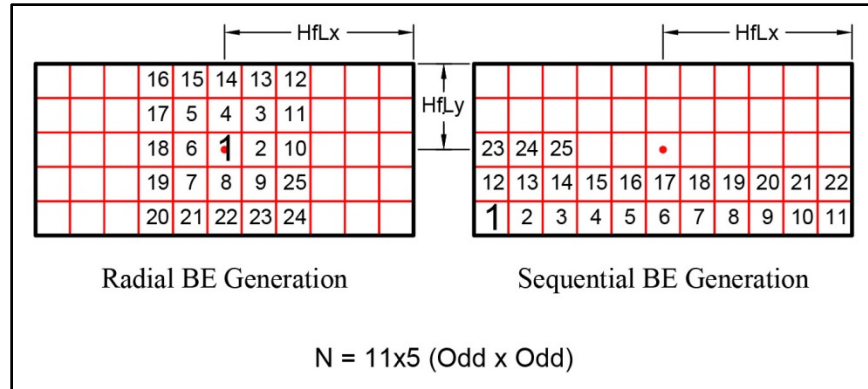


Figure 4.2—Radial and Sequential BE Mesh Generation  
in a Rectangular Fracture

## 4.2. Generation of Field Points in a HF Domain

Although domain discretization is not required in BEM, we still need field points throughout the domain to compute all necessary variables such as displacement field, strain and stress fields, etc. to have a deep insight about any HF model. Therefore, we need to generate a grid inside HF domain, which is a part of a reservoir around a drilled well. Field points, which we call them grid-nodes, are located at intersection of an orthogonal gridlines. The grid may be defined as uniformly spaced, or exponential/logarithmic-spaced. It needs to be reminded that the grid spacing inside the fracture is always uniform. Grid-nodes in the vicinity of the fracture have to be at mid-point of boundary elements.

For instance, for a penny-shaped fracture in Figure 4.3, the grid outside of the fracture is uniformly spaced. Since the formulation is singular at any boundary element face and edges, grid-nodes must have a small gap with them to avoid singularity. Figure 4.4 is an example of a fracture model with non-uniform grid spacing outside of it. Another

example in Figure 4.5 is a rectangular fracture with either uniform or non-uniform grid spacing.

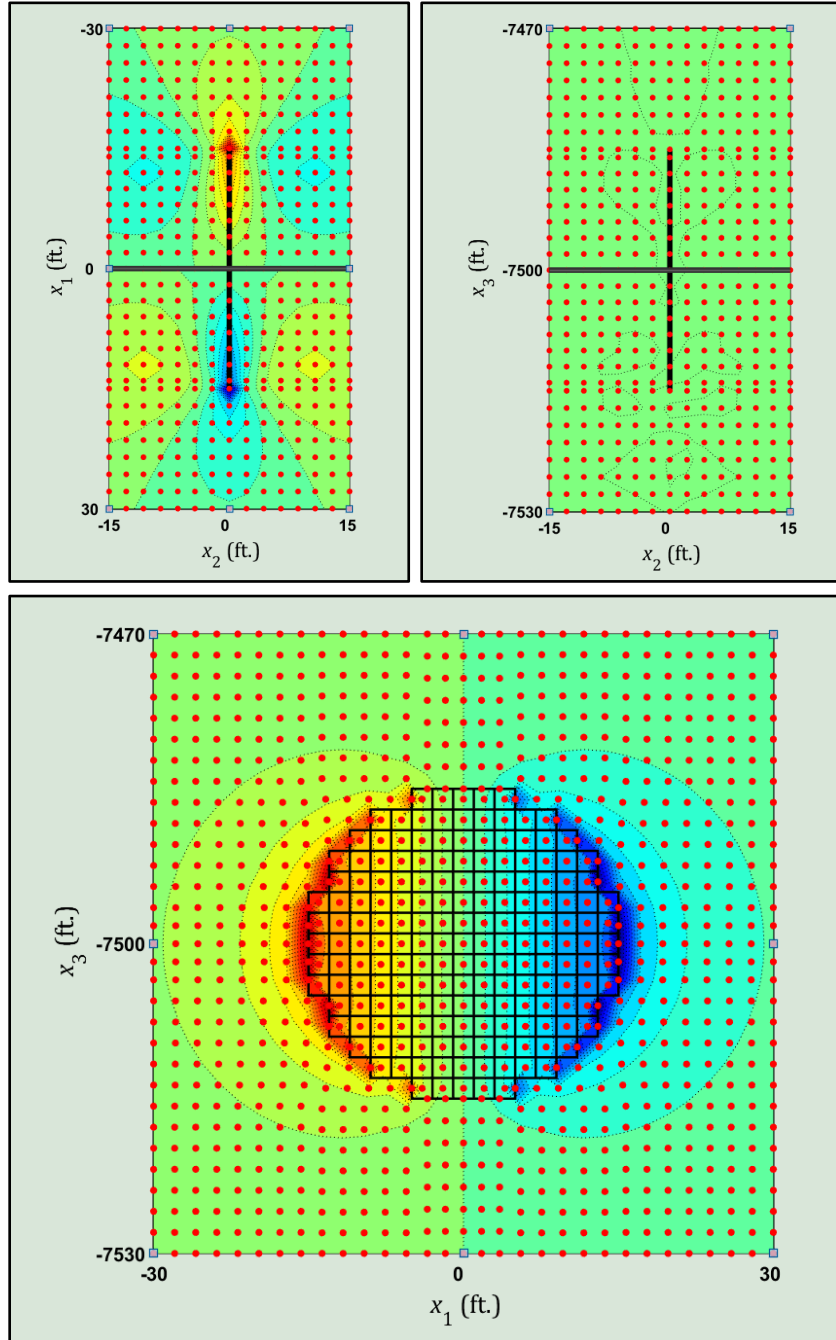


Figure 4.3—An Example of a  $15 \times 15$  Penny-Shaped Fracture and its corresponding grid of field-points. Upper-Left is Top View, Upper-Right is Side View, and the Lower One is Front View. Grid Spacing Outside of the Fracture is Uniform.

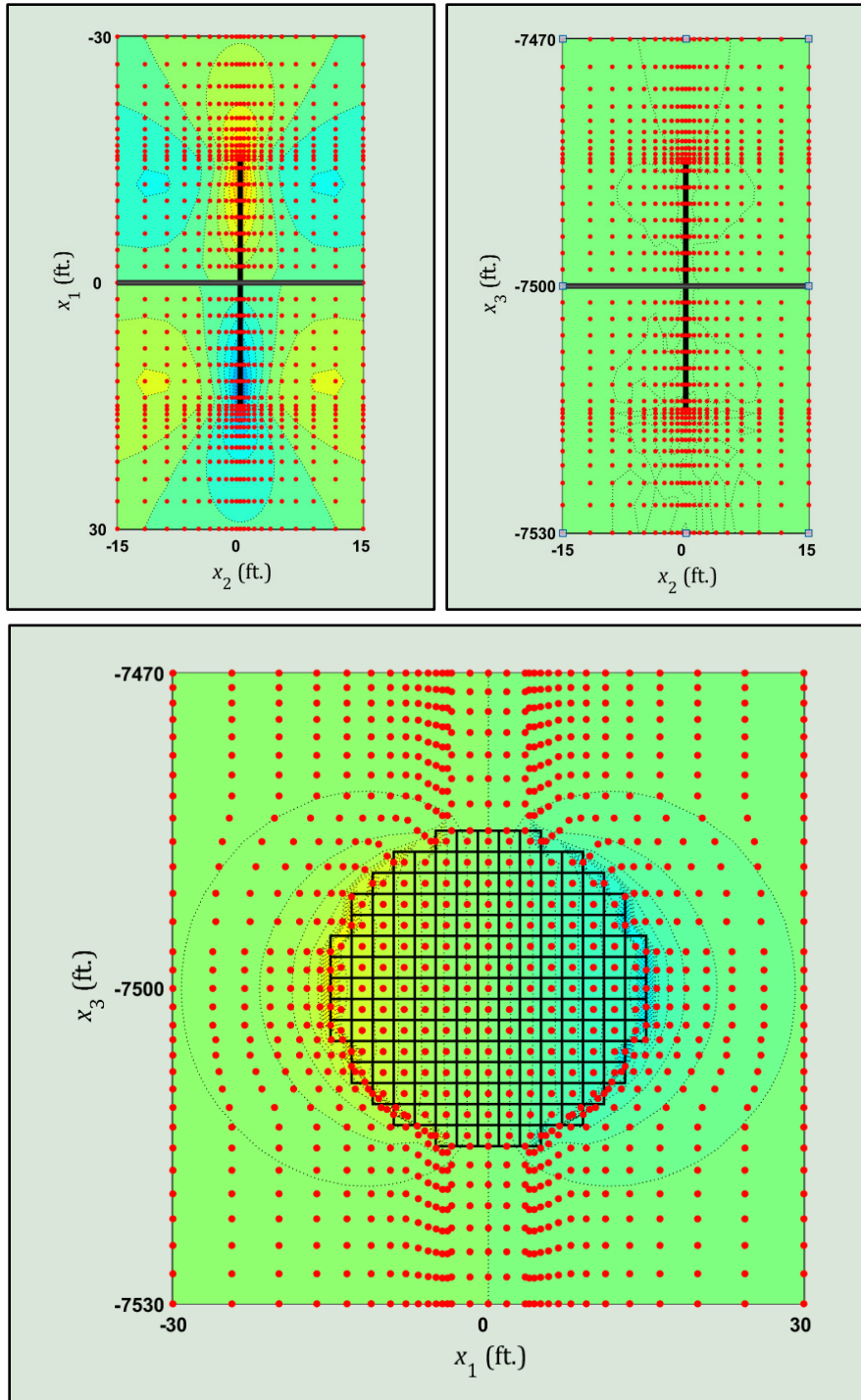


Figure 4.4—The Same  $15 \times 15$  Penny-Shaped Fracture and its corresponding grid of field-points. Grid Spacing Outside of the Fracture Varies Exponential/Logarithmic.

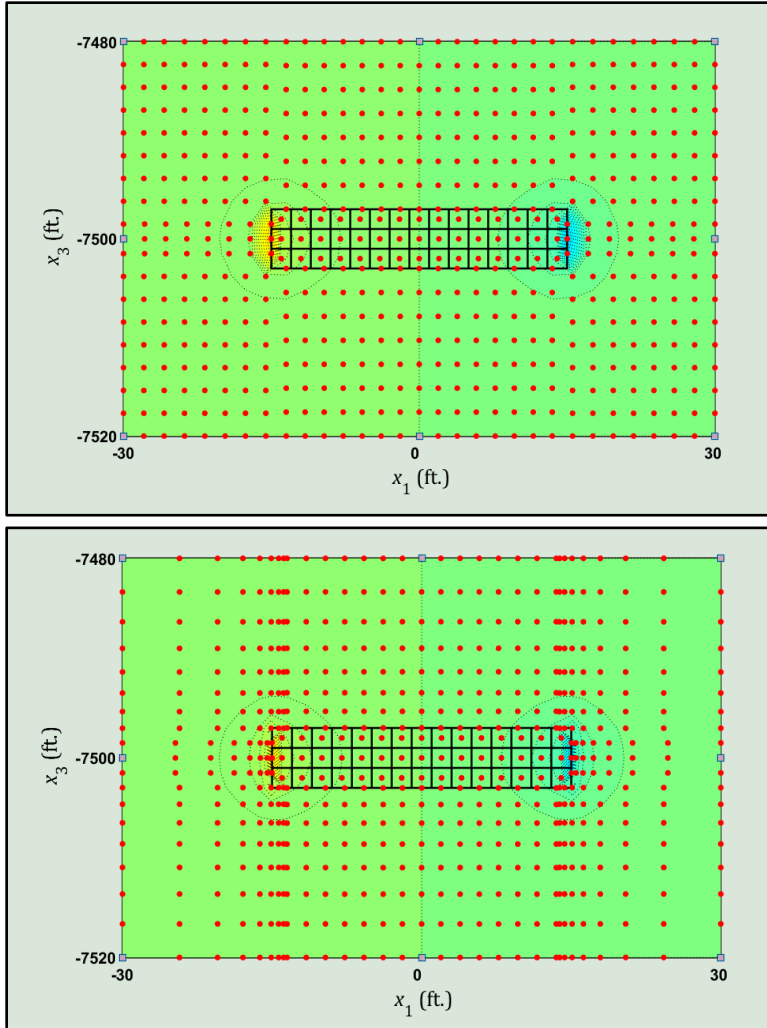


Figure 4.5—A  $15 \times 3$  Rectangular Fracture and its corresponding grid of field-points. Grid Spacing Outside of the Fracture is uniform for Top Figure and Exponential/Logarithmic for Bottom Figure. and Validation of the Method

In previous chapter we implemented our proposed method to a simulator and named our simulator HiFrac 3D. Moreover, we discussed about its capabilities and, also, showed its overall performance by modeling two hydraulic fracturing examples, one single-frac and one two-stage multi-frac problem. However, we did not discuss about its performance in detail. Now, in this chapter, we try to explain the performance of our method more

precisely. Moreover, we try to model several well-known problems and compare our results with those published data.

### 4.3. Comparison of the Method and Finite Element Method

One of the Fundamentals of FEM is to constrain all-but-one available degrees of freedoms either in discretized domain or discretized boundary, and then apply unit displacements or rotations to the open DOF. All equivalent nodal forces/stresses can, then, be obtained by integrating throughout each finite element and assembling them to a global frame to obtain the system of equilibrium equations. Since all DOFs in both analysis domain and boundary are constrained, equivalent nodal forces/stresses won't be transferred to nodes that well away from current DOF. Therefore, coefficient matrix of the equilibrium equation (say stiffness matrix) won't be filled completely by non-zero values. In other words, stiffness matrix will be banded. All non-zero components of the stiffness matrix will be concentrated around diagonal of it. Any component beyond that zone will be zero. In addition, according to Maxwell-Betti's reciprocal Work Identity, stiffness matrix obtained by FEM will always be symmetric. These characteristics can significantly increase numerical performance of the solution. On the other hand, our method which is a specific type of BEM, is based on discretization of just boundary of the domain. Therefore, constraining of a DOF won't completely block force/stress transformation to other DOFs, since the domain is completely free to move. This characteristic will lead to a stiffness matrix, totally filled by non-zero components. In addition, in some special cases, it was noticed that the stiffness matrix is not perfectly symmetric. These characteristics can negatively impact numerical performance of our proposed method. For better comparison between two methods, Figure 4.6 is provided below.

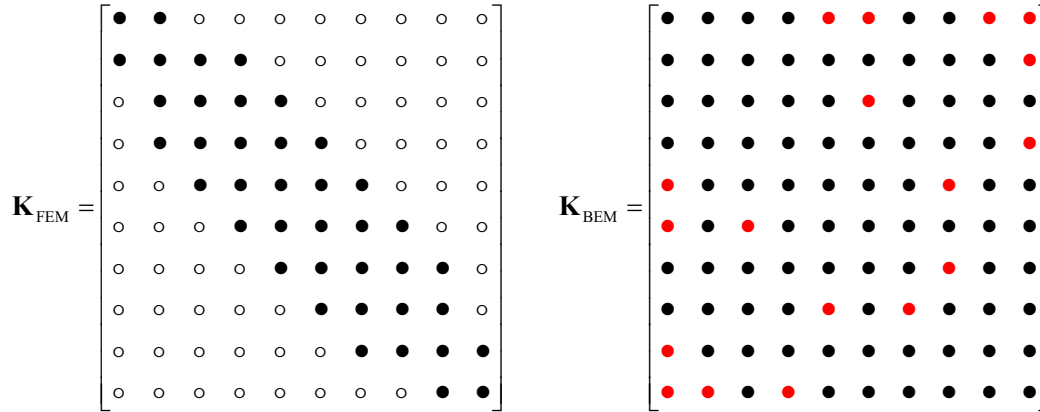


Figure 4.6—A Schematic of Stiffness Matrices Obtained from FEM and BEM.

#### 4.4. Verification of the Method

All black dots in Figure 4.6 represent symmetric non-zero values. Red dots represent non-symmetric values. Although a fully non-zero matrix is not a serious numerical issue according to available computers in the market, non-symmetrical characteristic is, indeed, a serious problem. Most numerical algorithms to solve a system of linear equations are developed for the case of symmetric coefficient matrix. This issue occurred in the example of two-stage multi-fracture in **Appendix B**, section 9. However, it never happened for the case of single fracture in section **Appendix B**, section 8. Non-symmetrical case is so evident when the dimensions of RABEs are significantly large. Also, it happened again when RABE sizes were small but aspect ratio of them in neighboring fractures were different. Numerous tries and errors were carried out and it was realized that when aspect ratio of RABEs (longer edge to shorter edge) were less than 2.00, the stiffness matrix was perfectly symmetric up to 5 decimal digits. For aspect ratio of less than 1.50 it was symmetric up to 9 decimal digits. Moreover, if the ratio of longer edges of RABEs in different fractures were less than 1.20, stiffness matrix was symmetric.



*It is recommended that aspect ratio of RABEs not to exceed 2.00.* Also, if the size of the longer edge of RABE is less than half of fracture spacing, the stiffness matrix will be perfectly symmetric even though the ratio of longer edges in different fractures exceed 1.20. *The best recommendation is to keep the size of longer edge of RABEs less than 0.45 times the smallest spacing between fractures.* In our research process, it was also realized that if boundary elements are well farther from each other, components of the stiffness matrix will be so close to zero. In other words, the farther from matrix diagonal, the smaller the component. By adding a condition to the computer code, we can make most of the stiffness matrix components zero. But, in practice, we did not apply this condition and left all the components unchanged.

Now that we overcame some shortcomings of our method, it would be a good idea to validate our method. We have selected several well-known problems to compare our results with.

#### **4.5. Comparison with Okada Example (Okada 1992)**

This example deals with a field measurement on a fault with tiltmeter. The paper does not mention real magnitude of dislocations but provides graphs based on magnitude of 50 cm for three separate dislocation types. It, also, approximates the real fault with a rectangular shape. A DDDv analysis is carried out with the model by just one RABE and initial specifications as Table 4.1. Since based on the published paper, the fault is assumed rectangular, using one RABE makes sense. Both measurement data and our analytical results are depicted in Figure 4.7. Curves corresponding to analytical and measured data are solid and dashed lines respectively.

Table 4.1—Fault Specification in Okada (1992)

Assumed Material Properties	$\lambda = \mu$ and $\nu = 0.25$
Fault Size	$L = 12$ km and $W = 8$ km
Depth of the Fault Origin	$c = 50$ km
Fault Dip Angle	$\delta = 40^\circ$
Coordinates of the Observation Point	$x_1 = 25$ km and $x_2 = 15$ km
Slip	$U = 50$ cm

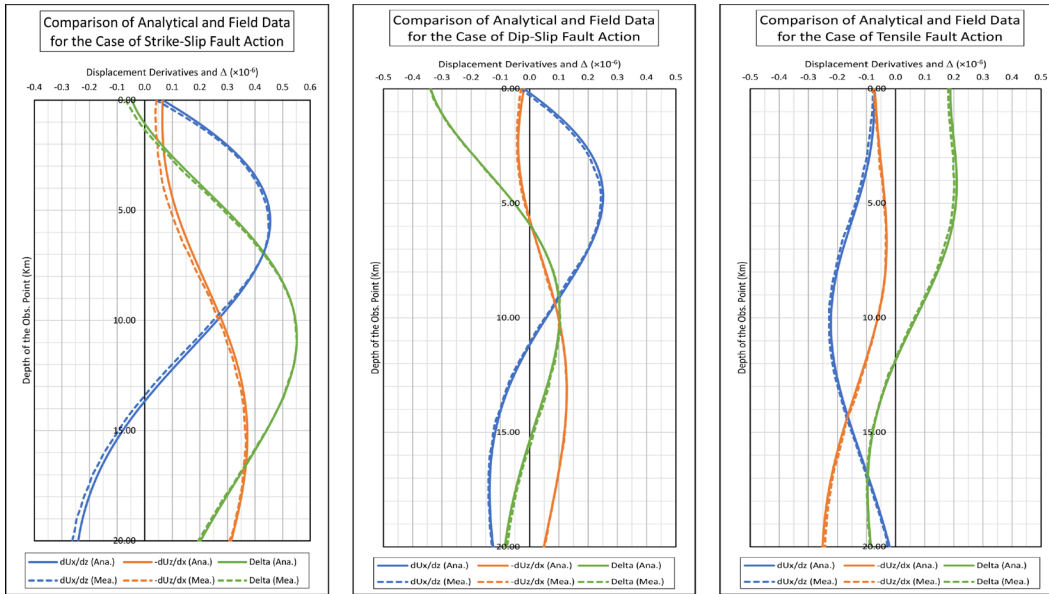


Figure 4.7—Comparison of Field Measurements and Model Results

Figure 4.7 shows a very good agreement between both data. Parameter  $\Delta$  In Figure 4.7 is defined as,  $\Delta = \partial u_x / \partial x + \partial u_y / \partial y$ . Other measured parameters are,  $\partial u_x / \partial z$  and  $\partial u_z / \partial x$ . This comparison validates that HiFrac 3D computes DDDv's reliably and accurately. But this validation is just based on one RABE. In next sections, we try to validate our simulator for different cases.

#### 4.6. Verification by Fialko's Solution

Fialko et al., 2001 provided the exact expressions to solve a problem of horizontal circular crack due to intrusion of magma. They assume the domain is an elastic half-space and pressure inside the crack is constant. Although our simulator is currently developed based on constant pressure at both walls of the fracture, but it is easily capable to be developed for variable fluid injection pressure as well. Fialko solution gives horizontal and vertical displacements at any point in the domain and free surface. However, graphs in their published paper just illustrates these field variables at free surface. In this problem,  $R$  and  $H$  are radius and depth of the circular fracture respectively. Moreover,  $h$  is normalized depth with respect to  $R$ . Figure 4.8 illustrates a schematic view of a horizontal crack in Fialko problem.

In first step, we try to compare horizontal displacement field results from HiFrac 3D to those of Fialko model. Figure 4.9-Left depicts our numerical fracture model for the case of  $H/R = 1.20$ . The Black curve represents Fialko et. Al. results. Red and green curves are our results for the cases of  $5 \times 5$  and  $15 \times 15$  mesh sizes respectively.

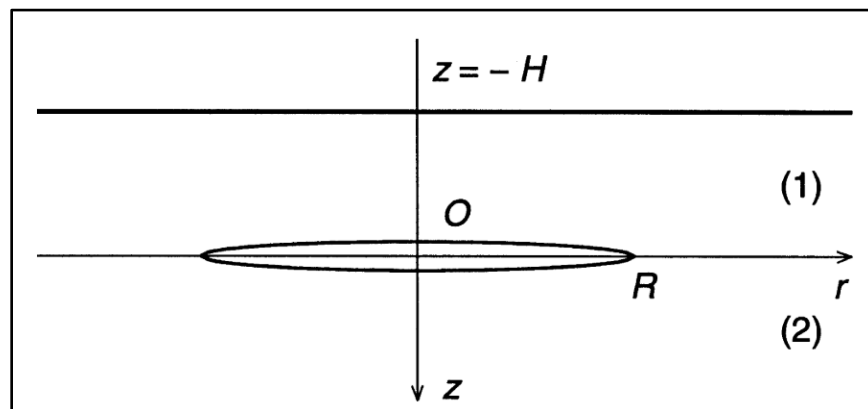


Figure 4.8—A Cross-Sectional View of a Penney-Shaped Horizontal Fracture in an Elastic Half-Space (Fialko et al. 2001)

As evident, there is a great agreement between our study and Fialko et. Al. closed-form research. During simulation, we intended to include a numerical result based on  $25 \times 25$  mesh size but since we reached a good match with the case of  $15 \times 15$  mesh size, we preferred not to include it. The mesh size of  $15 \times 15$  is adequate to obtain acceptable results.

In the next step, we try to validate vertical displacement field. Results from both Fialko model and our simulation are found in Figure 4.10. Like Figure 4.9, black curves represent Fialko results and red and green curves come from the model. It is clear that black curve has almost been covered by red and green ones which, again, is a proof of accuracy of our simulator. Now, we can be confident that our procedure produces great results for displacement field components resulting from a single penny-shaped fracture.

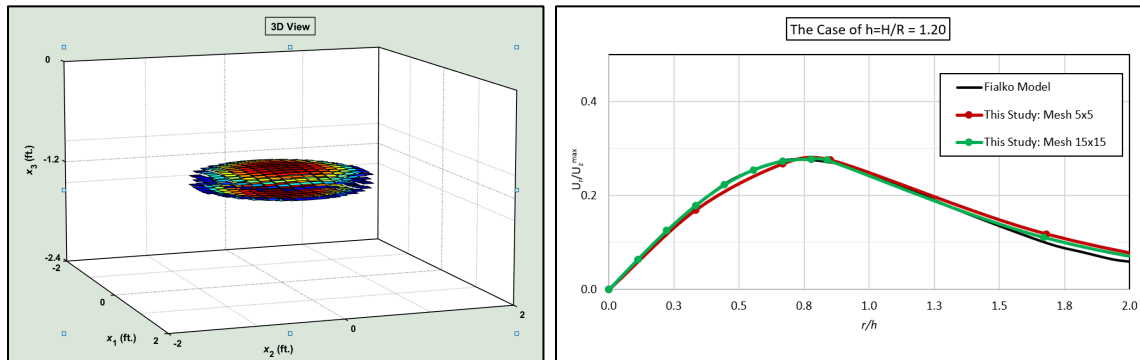


Figure 4.9—Left side shows our horizontal circular fracture at depth 1.2 and radius 1.0. Right side shows Horizontal Displacement Field at Free Surface of an Elastic Half-space

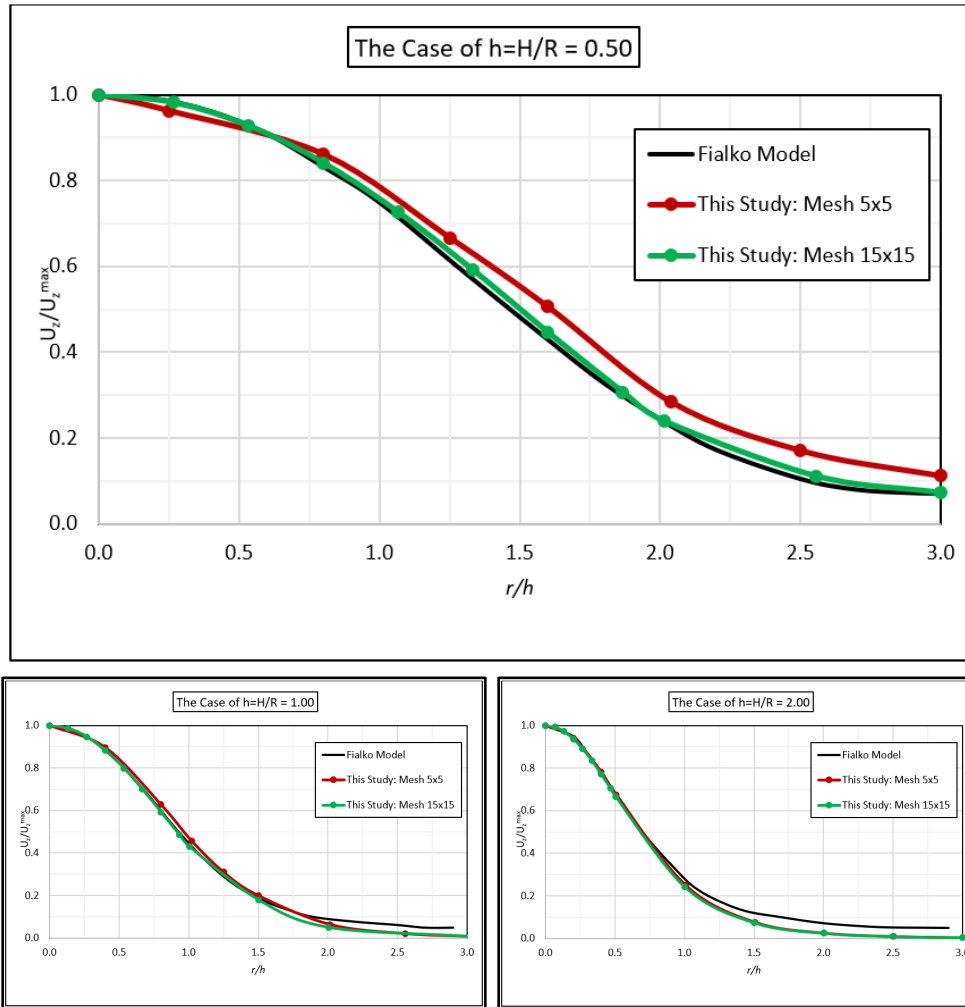


Figure 4.10—Vertical Displacement Field at Free Surface of an Elastic Half-space

#### 4.7. Verification by Pollard Solution

The problem is a closed-form analytical solution to find interaction between earth's horizontal free surface and a uniformly pressurized rectangular fracture in a linear elastic half-space (Pollard and Holzhausen 1979). According to Figure 4.11, it is assumed that the model follows 2D Plane-Strain behavior and the fracture may have any inclination (dip angle  $\beta$ ). In addition to deformation of horizontal free surface, the solution, also, gives set of equations to analyze stress components in the model domain and Mode I / Mode II

Stress Intensity Factors  $K_I$  and  $K_{II}$  which is useful to model fracture propagation due to increase in fluid injection pressure.

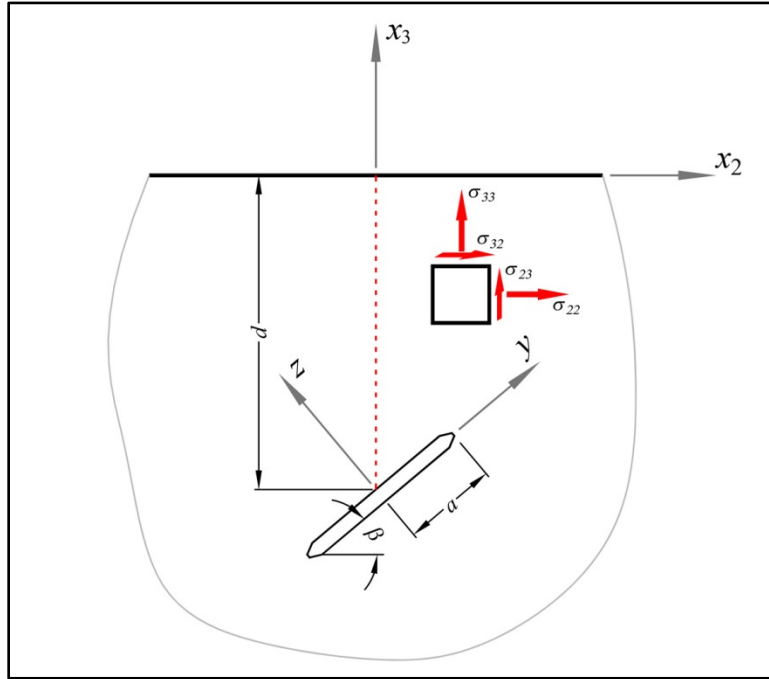


Figure 4.11—A Rectangular Fracture in a Linear Elastic Half-Space. Axes  $x_1$  and  $x_2$  Are Perpendicular to Figure Surface. Fracture Length along  $x_2$  – Axis Is Long Enough to Simulate a 2D Plane-Strain Problem.

Stress Intensity Factor analysis is currently outside of scope of our research, although it can be easily added in future developments to our simulator. The same problem has, also, been modeled numerically by FEM (Fu 2014). Although Fu’s FEM model is 3D, he defined the fracture length along  $x_2$  – axis 3 times the width of it (i.e.  $a$ ) and constrained displacements in  $x_1$  – direction to approximate a 2D case. It is easy to realize that constraining displacement field  $u_1$  makes strain components  $\epsilon_{11}$ ,  $\epsilon_{12}$ , and  $\epsilon_{13}$  equal to zero and converts a general 3D model to a 2D plane-strain. However, since our method is a boundary element method, we have no control over model domain. Therefore, we choose

half-length along  $x$  – axis 8 times that of  $y$  – axis in HiFrac 3D. All model specifications are given in Table 4.2.

Table 4.2— Initial Values and Properties Simulate Pollard-Fu Problem

Parameter or Property	Value	Unit
Elastic Modulus	$E = 1.00 \times 10^6$	psi
Poisson's Ratio	$\nu = 0.25$	Unitless
Min./Max. Hor. In-Situ Stress	$S_{\min}^H = S_{\max}^H = 0$	psi
Depth of Injection Point	$d = 4.10$	ft.
Dip Angle	$\beta = 0^\circ$ or $90^\circ$	
Half-Lengths of HF	$hfL_x \times hfL_y = 25.00 \times 3.28$	ft. $\times$ ft.
RABE Mesh Size in Case 1	$35 \times 5$	
RABE Mesh Size in Case 2	$105 \times 15$	
Extent of the Model Domain	$60 \times 25 \times 15$	ft.
No. of Grid Spacing Outside Fracs.	20	
Injection Pressure at Depth	$\Delta p = 1$	Psi

It needs to be mentioned that the ratio of depth to half-width, according to Pollard problem, is 1.25 (i.e.,  $d/a = 1.25$ ).

Figure 4.12 and Figure 4.13 depict the geometry of the model after exerting pressure into the fracture for dip angle  $\beta = 0^\circ$ . Mesh sizes for Case 1 and Case 2 are  $35 \times 5$  and  $105 \times 15$  respectively. Furthermore, Figure 4.14 and Figure 4.15 depict the model geometry except that dip angle  $\beta = 90^\circ$ .

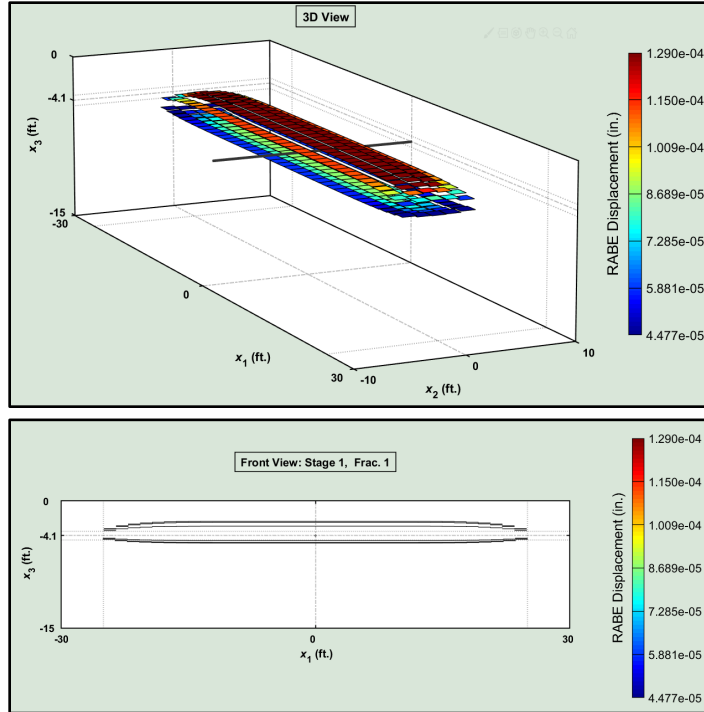


Figure 4.12—Geometry of the Simulation Model for Case 1.  
 Mesh Size is  $35 \times 5$  and  $\beta = 0^\circ$

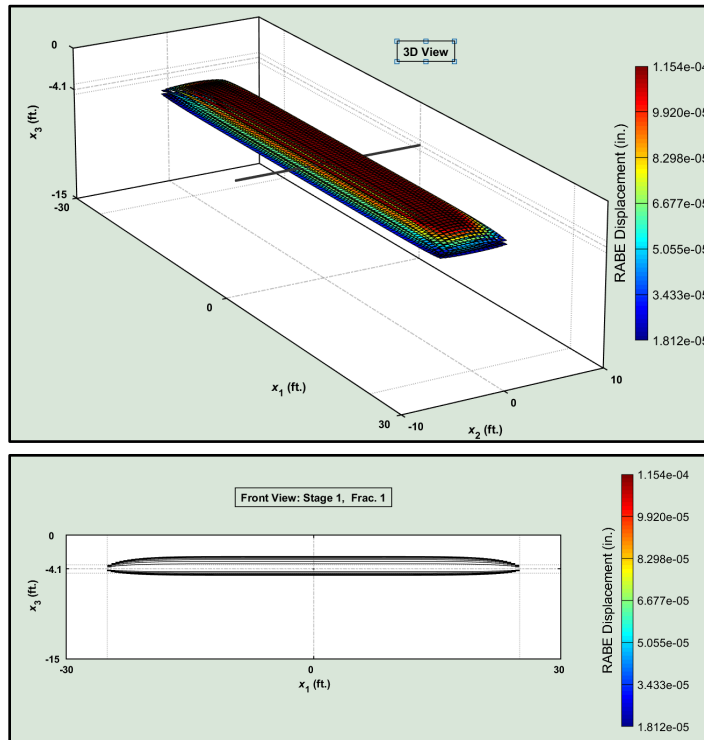


Figure 4.13—Geometry of the Simulation Model for Case 2.  
 Mesh Size is  $105 \times 15$  and  $\beta = 0^\circ$



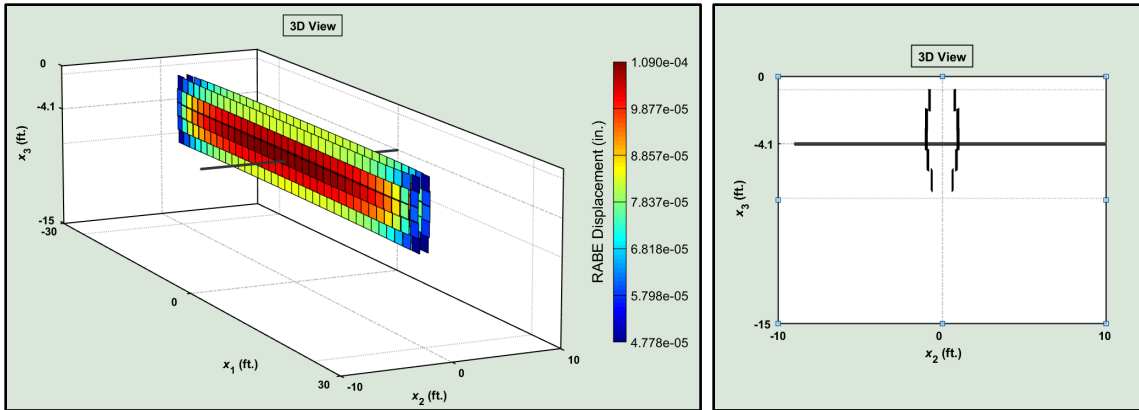


Figure 4.14—Geometry of the Simulation Model for Case 1.

Mesh Size is  $35 \times 5$  and  $\beta = 90^\circ$

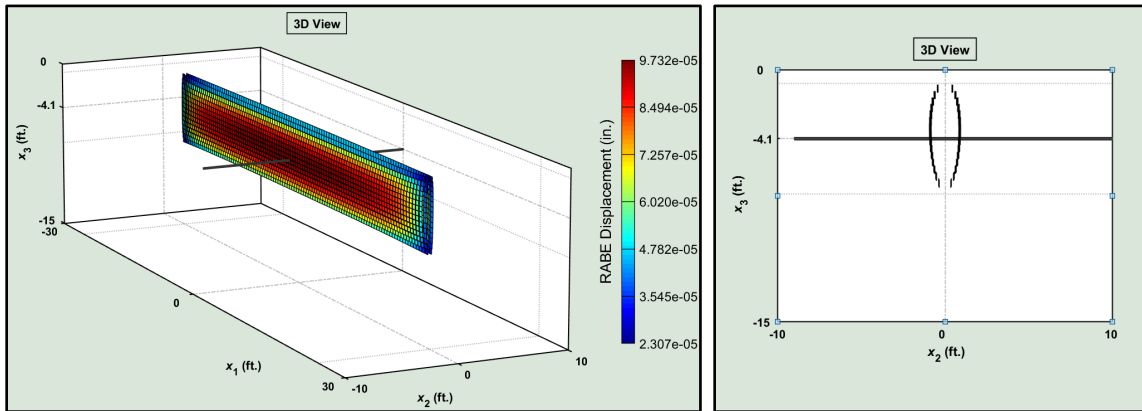


Figure 4.15—Geometry of the Simulation Model for Case 2.

Mesh Size is  $105 \times 15$  and  $\beta = 90^\circ$

Huang, also, verified his finite element formulation (Huang 2015). His model comprises about 127'000 3D EPM elements which certainly has a very high number of degrees of freedom.

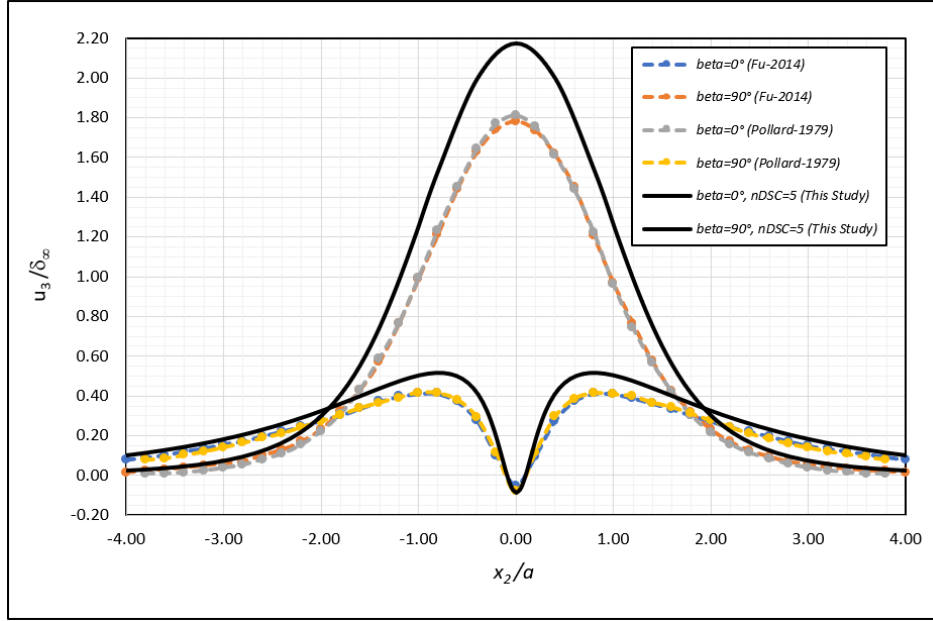


Figure 4.16—Comparison of Normalized Vertical Displacement  $u_3$  Results at Horizontal Free Surface, Obtained from HiFrac 3D to Those of Fu-2014 and Pollard-1979. Black Curves Are Corresponding to Case 1 with the Mesh size of  $35 \times 5$ .

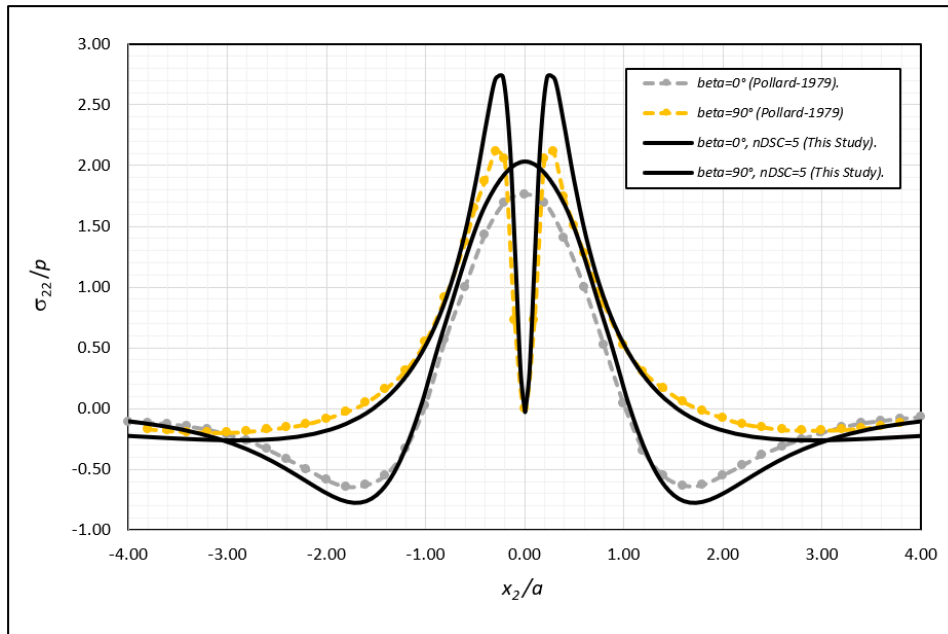


Figure 4.17—Comparison of Normalized Horizontal Stress  $\sigma_{22}$  Results Near Horizontal Free Surface, Obtained from HiFrac 3D to Those of Pollard-1979. Black Curves Are Corresponding to Case 1 with the Mesh size of  $35 \times 5$ .

Figure 4.16 compares the results of normalized vertical displacement  $u_3$  at free horizontal surface with respect to normalized distance  $x_2$ . Vertical displacement and distance are normalized with respect to maximum field displacement  $\delta_\infty$  and fracture half-width  $a = 3.28$  ft. respectively. The parameter  $\delta_\infty$  is calculated by the following equation.

$$\delta_\infty = \Delta p \cdot a(1-\nu) / \mu \quad (5.1)$$

In this model,  $\delta_\infty = 7.74900 \times 10^{-5}$  in.. Mesh size in Figure 4.16 is  $35 \times 5$ . Further, in Figure 4.17, the results of normalized horizontal stress  $\sigma_{22}$  from HiFrac 3D and Pollard-1979 are compared. Horizontal stresses are normalized with respect to injection pressure  $\Delta p$  which is 1.00 psi.

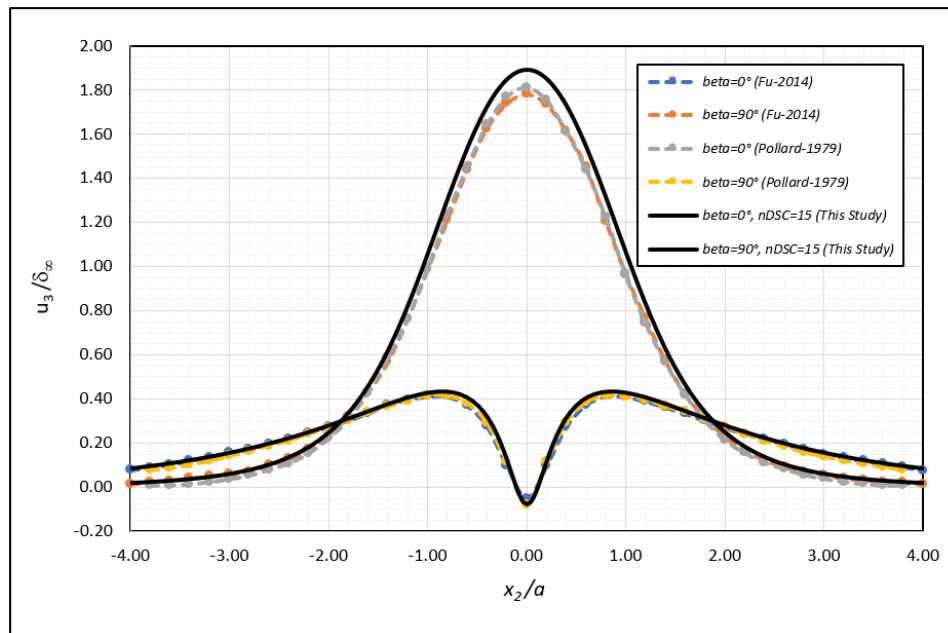


Figure 4.18—Comparison of Normalized Vertical Displacement  $u_3$  Results at Horizontal Free Surface, Obtained from HiFrac 3D to Those of Fu-2014 and Pollard-1979. Black Curves Are Corresponding to Case 2 with the Mesh size of  $105 \times 15$ .

In case 2, which mesh size is  $105 \times 15$  the same comparisons are carried out. Graphical comparisons are showed in Figure 4.18 and Figure 4.19.

According to Figure 4.16 and Figure 4.17, it is inferred that the mesh size of  $35 \times 5$  does not result a good agreement. However, Figure 4.18 and Figure 4.19 represent a very good agreement between HiFrac 3D and other results with the mesh size of  $105 \times 15$ . In other words, the model becomes less sensitive to mesh size if greater than  $105 \times 15$ . In terms of performance, general simulation data are provided in Table 4.3 and Table 4.4. The analysis time for the Case 2, which is highly accurate, is more than one hour.

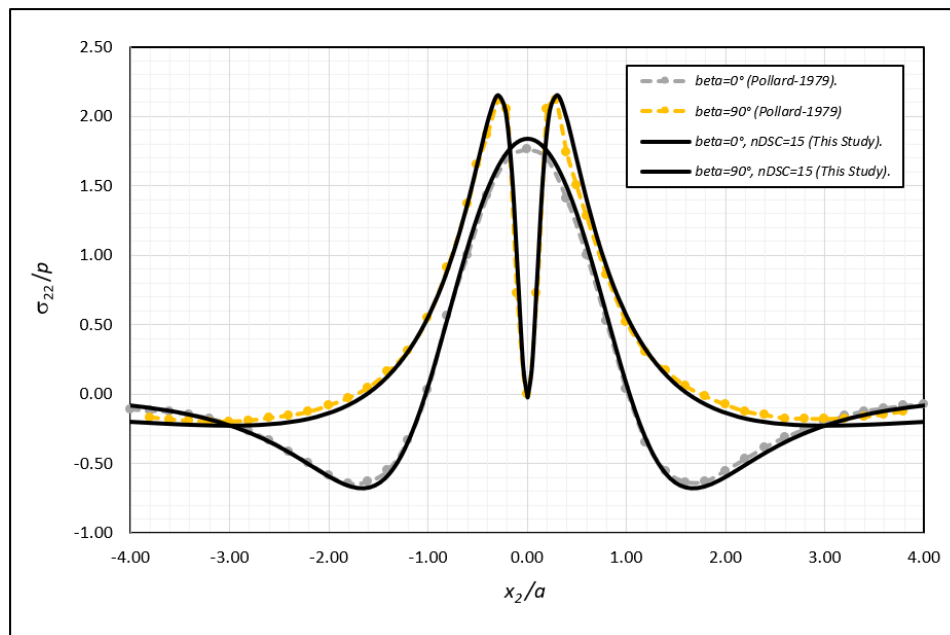


Figure 4.19—Comparison of Normalized Horizontal Stress  $\sigma_{22}$  Results Near Horizontal Free Surface, Obtained from HiFrac 3D to Those of Pollard-1979. Black Curves Are Corresponding to Case 2 with the Mesh size of  $105 \times 15$ .

Table 4.3— General Information About a Single-Fracture  
Pollard’s Solution Model - Case 1: Mesh Size  $35 \times 5$ .

<b>Parameter or Property</b>	<b>Value</b>
Total No. of RABEs	175
Total No. of Grid Nodes	80’934
Total No. of Degrees of Freedom	525
Dislocation Analysis Time ( $\mathbf{KU} = \Delta\mathbf{P}$ )	0.021 min.
DDDv Analysis Time (Okada’s Formulation)	1.198 min.
Strain/Stress Analysis in Stage 1	$\approx 0.000$ min.
Total Analysis Time	1.228 min.

Table 4.4— General Information About a Single-Fracture  
Pollard-Fu Model - Case 2: Mesh Size  $105 \times 15$ .

<b>Parameter or Property</b>	<b>Value</b>
Total No. of RABEs	1’575
Total No. of Grid Nodes	265’734
Total No. of Degrees of Freedom	4’725
Dislocation Analysis Time in Stage 1 ( $\mathbf{KU} = \Delta\mathbf{P}$ )	6.006 min.
DDDv Analysis Time (Okada’s Formulation)	60.024 min.
Strain/Stress Analysis in Stage 1	0.027 min.
Total Analysis Time	66.278 min.

Fu-2014 and Pollard-1979 did not provide data such and displacement field or stress contours. To compare our results, we use illustrations in Huang-2015 dissertation. We only compare results from Case 2 which seems very accurate and don’t illustrate results from Case 1.

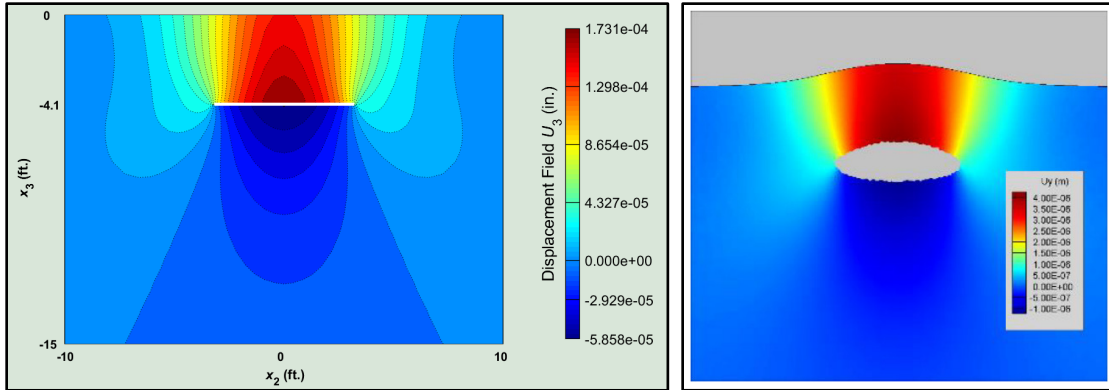


Figure 4.20—Comparison of Vertical Displacement  $u_3$  Results at Horizontal Free Surface, Obtained from HiFrac 3D (Left) to That of Huang-2015 (Right). Dip Angle is  $0^\circ$  and Mesh size is  $105 \times 15$ .

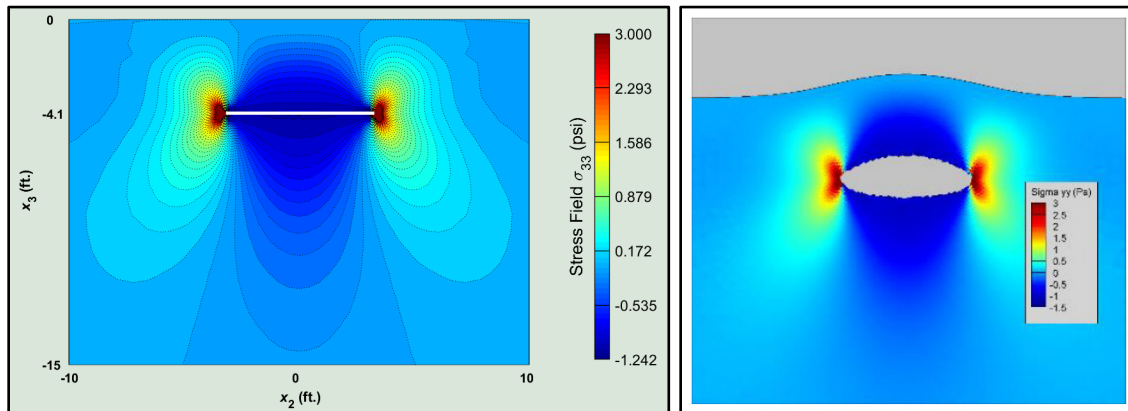


Figure 4.21—Comparison of Vertical Stress  $\sigma_{33}$  Results Near Horizontal Free Surface, Obtained from HiFrac 3D (Left) to That of Huang-2015 (Right). Dip Angle is  $0^\circ$  and Mesh size is  $105 \times 15$ .

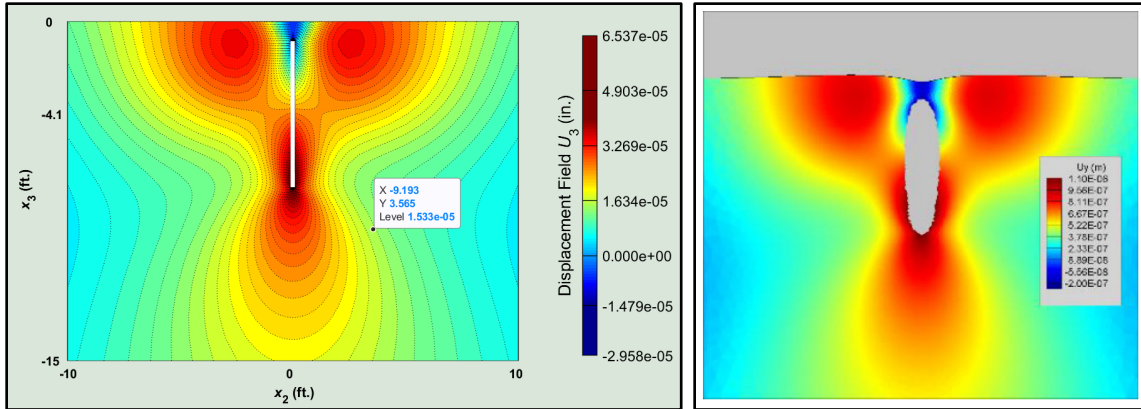


Figure 4.22—Comparison of Vertical Displacement  $u_3$  Results at Horizontal Free Surface, Obtained from HiFrac 3D (Left) to That of Huang-2015 (Right). Dip Angle is  $90^\circ$  and Mesh size is  $105 \times 15$ .

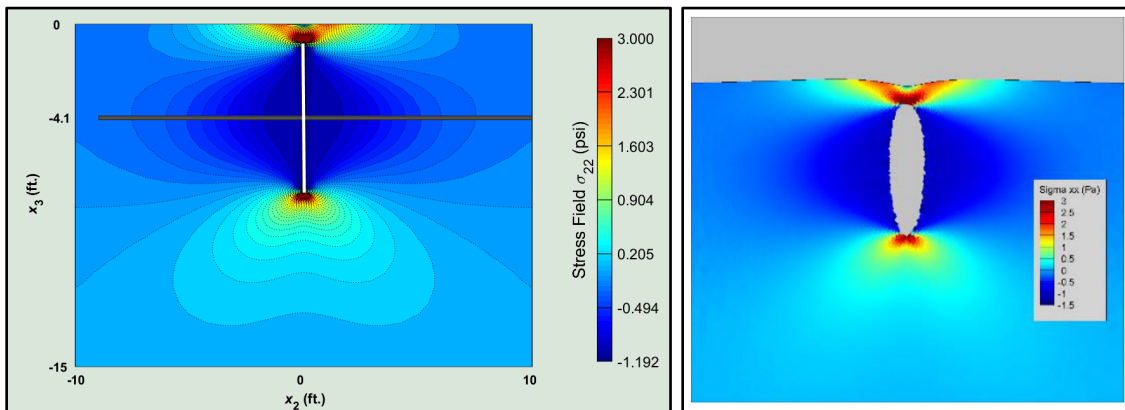


Figure 4.23—Comparison of Vertical Stress  $\sigma_{33}$  Results Near Horizontal Free Surface, Obtained from HiFrac 3D (Left) to That of Huang-2015 (Right). Dip Angle is  $90^\circ$  and Mesh size is  $105 \times 15$ .

As mentioned above, Huang used roughly 127'000 3D EPM elements to model Pollard's problem. Analysis of a model with 127'000 elements with regular PC can take days or weeks. Using a super-computer can reduce analysis time down to a few hours which is still too long.

#### 4.8. Verification of Displacement Derivatives

Since a well-known multiple cluster penny-shaped or rectangular hydraulic fracturing was not found in published research articles, we take another way to validate HiFrac 3D for this case. According to sections 4.5. to 4.7. , We are certain that displacement field analysis and simulation is valid; however, to carry out strain and stress analysis, we need reliable values for displacement field derivatives. Okada formulation, which is the foundation of our BEM, is able to give us derivatives of displacement field components by set of functions that were discussed in Chapter 2. The other way to obtain displacement derivatives is to use Finite Difference Method which is a pure numerical method. Since we trust displacement field analysis of our simulator, we can trust numerical derivation of those components as well. Therefore, we try to illustrate derivatives obtained from two totally different methods. The best way to illustrate is to use gradient of every single displacement component. Displacement components are our scalar properties. Gradient of any scalar function will give a vector function as the following equation.

$$\vec{\nabla}U_i = \frac{\partial U_i}{\partial x_1}\mathbf{e}_1 + \frac{\partial U_i}{\partial x_2}\mathbf{e}_2 + \frac{\partial U_i}{\partial x_3}\mathbf{e}_3 = U_{i,j}\mathbf{e}_j \quad (5.2)$$



By obtaining scalar components  $U_{i,j}$  from both our simulator and FDM, we can establish and illustrate those vectors simultaneously. If set of vectors from two methods match reasonably, we can claim that our simulator is able to analyze reliable displacement derivatives for the case of Multi-Cluster fracture stage. To reach this goal we define an arbitrary stage with 3 fractures. Then we apply an arbitrary injection pressure. To make the model asymmetric, we also exert arbitrary frictions to fracture walls. Initial values to define a single-stage multi-cluster fracture are outlined in Table 4.5.

Table 4.5— Initial Values and Properties for a Single-Stage Multi-HF Model

Parameter or Property	Value	Unit
Elastic Modulus	$E = 7.4404 \times 10^6$	psi
Poisson's Ratio	$\nu = 0.26$	Unitless
Min. Hor. In-Situ Stress	$S_{\min}^H = -1000.00$	psi
Max. Hor. In-Situ Stress	$S_{\max}^H = -2000.00$	psi
Average Specific Density of Rock	$\gamma = 0.00$	pcf
Depth of Injection Point	$D = 7500.00$	ft.
Radius of HFs	$R_f = 15.00$	ft.
RABE Mesh Size	$15 \times 15$	
Frac. Spacing	$s = 20.00$	ft.
Number of HFs	$n = 3$	
Extent of the Model Domain	$50 \times 60 \times 50$	ft.
Fracture Orientation	Vertical ( $\delta = 90^\circ$ )	
No. of Grid Spacing Outside Fracs.	5	
Injection Pressure at Depth	2100 ( $\Delta p = 1100.00$ )	psi
Friction at Frac Walls (Strike and Dip)	$f = 110.00$	psi

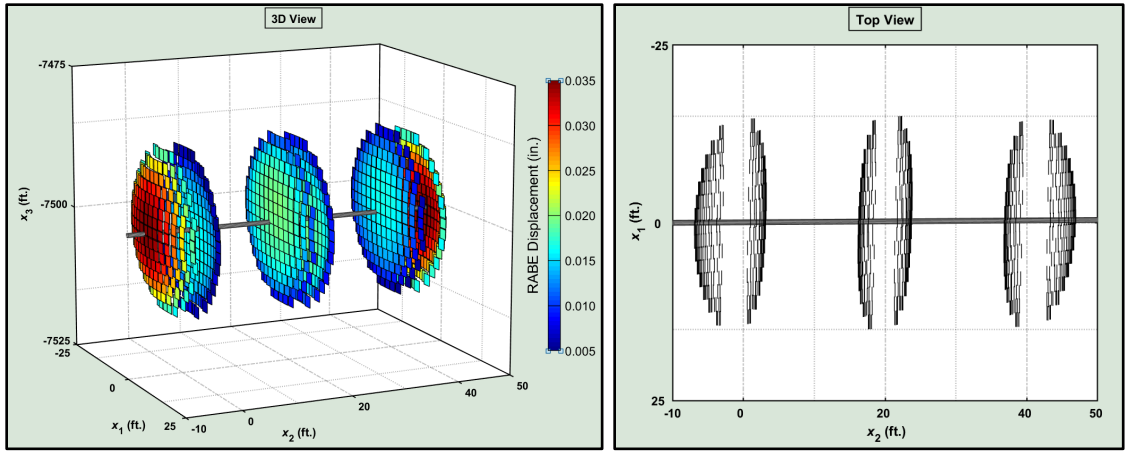


Figure 4.24— 3D (Left) and Top (Right) View Geometries of an Arbitrary Multi-Cluster Hydraulic Fracture After Fluid Injection.

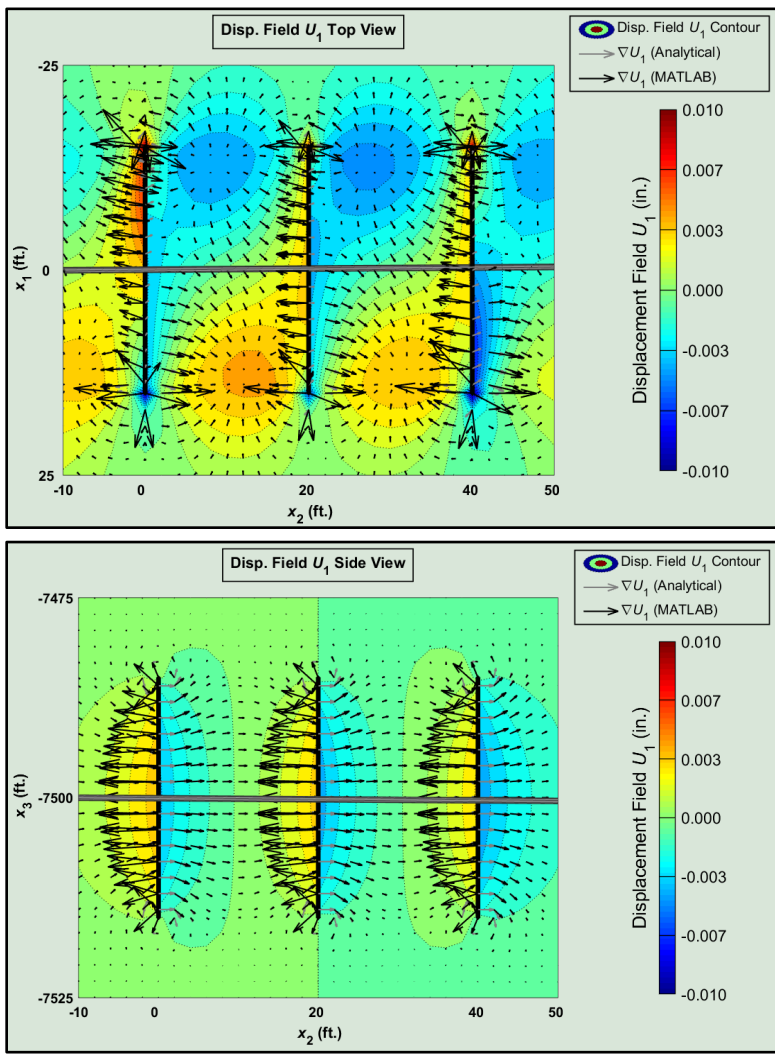


Figure 4.25— Gradient Vectors of Displacement Field Component  $u_1$

Figure 4.24 shows deformed shape of the model. Distortion is so evident in top view due to exertion of frictions (tangential forces). In Figure 4.25 to Figure 4.27, displacement gradient vectors are illustrated for scalar components  $u_1$ ,  $u_2$ , and  $u_3$ . Gray vectors are computed based on our semi-analytical procedure. Black vectors are based on FDM computations. FDM computation was carried out by MATLAB.

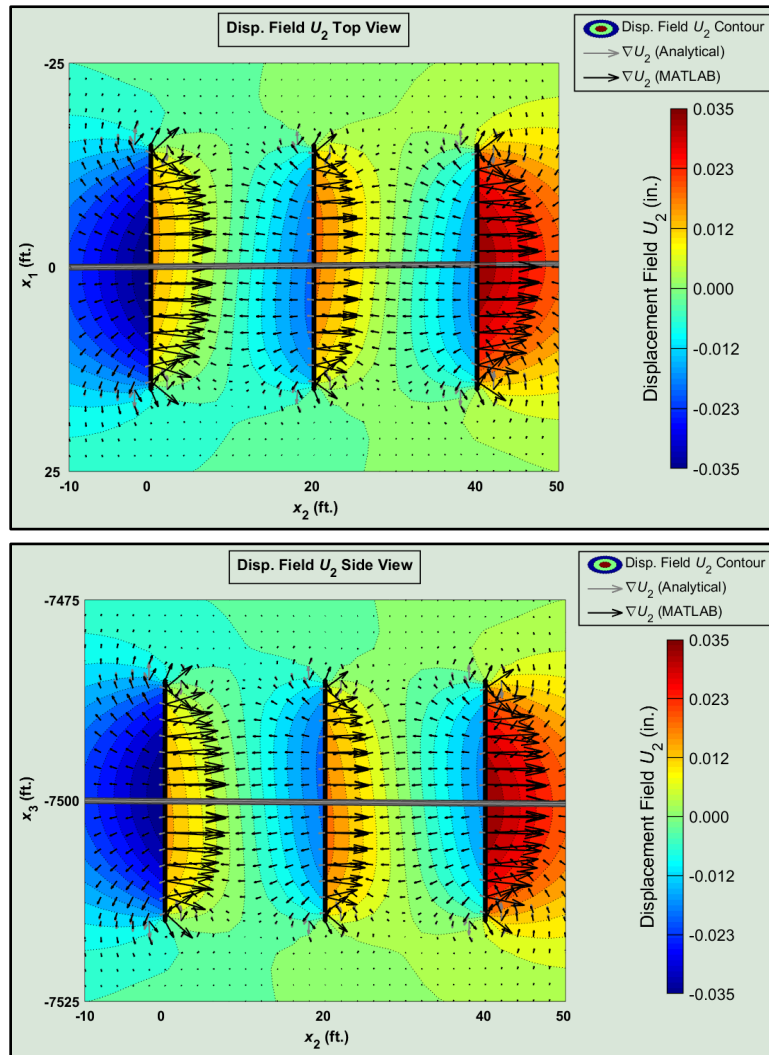


Figure 4.26— Gradient Vectors of Displacement Field Component  $u_2$

MATLAB gradient computation is limited to uniformly spaced grid of field points. We tried to make the domain grid as uniform as possible. But the generated grid is not

perfectly uniform especially near fracture tips. In all mentioned figures, displacement field components are shown by contours. To save space, just top and sides views are shown. Our simulator is able to show any arbitrary cross-section of the model. A great agreement is crystal clear between black and grey vectors in most grid-nodes. Grey vectors have been covered by black vectors in most of grid-nodes which is an evidence of validity of semi-analytical procedure. In a very limited number of points, a slight discrepancy is noticed, especially near fracture tips which is obvious.

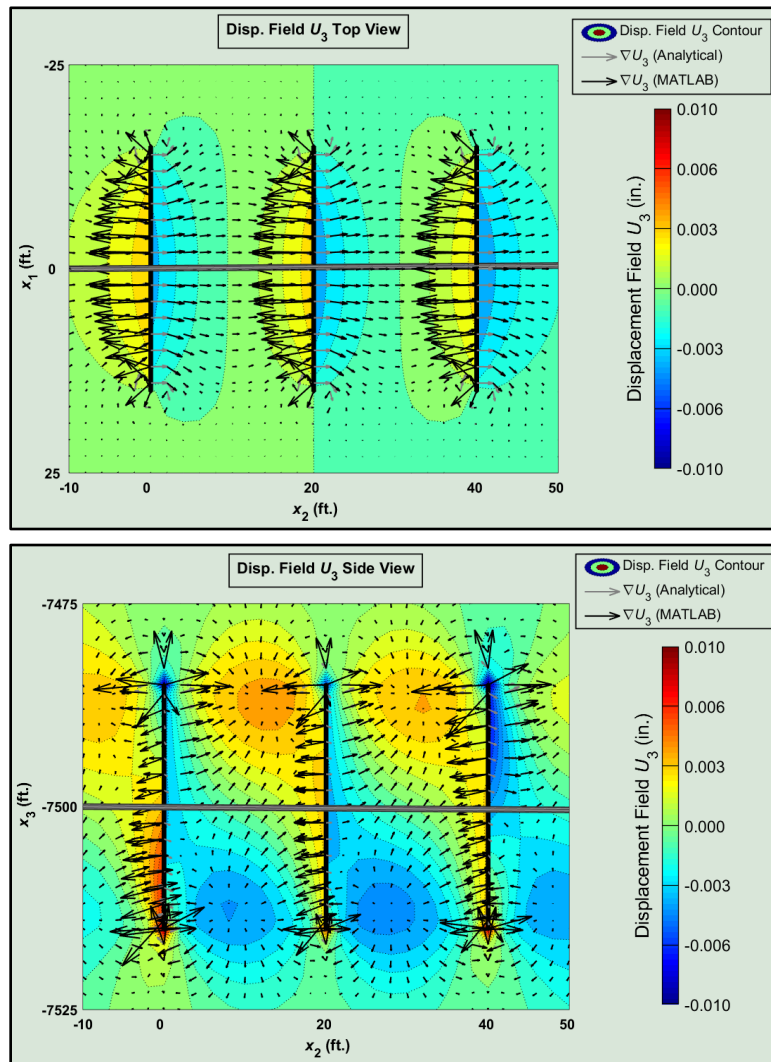


Figure 4.27— Gradient Vectors of Displacement Field Component  $u_3$

Since variation rate of displacement components are too high near fracture tips, a smaller and finer grid spacing is required to approximate derivatives by means of FDM. FDM usually has less tendency to approach exact results. However, direction of grey and black vectors is in an acceptable agreement. The great match between grey and black vectors, indeed, validates our simulator to model multi-cluster fracture stages.

If displacement derivatives are valid, strain analysis and, hence, stress analysis will also be valid. Now, we can trust our simulator for both single-cluster and multi-cluster hydraulic fracture modeling and analysis.

## CHAPTER 5. Conclusion and Recommendations

### 5.1. Conclusion

In modern era, analysis and simulation of displacement field is perhaps the first and most important step to model, simulate and, finally, design a good hydraulic fracturing system to plan and develop an unconventional hydrocarbon reservoir or even geothermal reservoir. Displacement field analysis helps engineers to know the geometry of a hydraulic fracture such as shape and aperture. Fracture aperture, along with the shape, is also important to estimate productivity of a fractured well. Lack of understanding about fracture geometry may be source of some problems such as frac hit and production interaction especially in the case of narrow and dense well spacings. And knowing hydraulic fracturing geometry is required to figure out Stimulated Volume of the reservoir (SRV). Effective permeability of a fractured well is a function of fracture geometry. The second most vital step to modern and sophisticated analysis and design of a hydraulic fracturing treatment is Stress analysis. Understanding state of stress is a key to include reservoir rock failure and, hence, estimate fracture growth and propagation as a function of fluid injection pressure and many other parameters. In this study, we used a semi-analytical boundary element method to deal with displacement field and stress analysis. A classical BEM, as a full numerical method, was briefly described to understand basics of the method. Full closed analytical methods are applicable to just very simple cases such as penny-shaped, elliptical-shaped, and rectangular-shaped fractures. For some of these cases, fracture must be either horizontal or vertical. Moreover, for the case of multi-cluster

fractures when there are interactions between clusters, analytical methods come short. Our method, on the other hand, is not fully numerical as well since it does not need numerical integrations to establish a system of equilibrium equations. We used Okada Dislocation formulation which is a closed-form analytical solution for a finite rectangular source. We approximated the geometry of fracture(s) by discretization of it/them into finite number of RABEs. Since we use closed-form analytical equations we don't need a very fine mesh to approximate fracture geometry. However, the method has some drawbacks too. The proposed boundary element must be rectangular, but in classical BEM, the element may have more flexible shapes such as tetragon or triangle. So, there should be some trade-offs between analytical performance and approximation of fracture geometry. As illustrated in previous chapters, discretized fracture geometry looks coarse, however, displacement and stress field analyses have fantastic accuracy which are so important. To propose our procedure, Okada's dislocation theory and formulation was discussed to understand its advantages and disadvantages. Its advantage is accuracy, but equations are so complicated which makes it so difficult to find and fix possible errors during computer code development. Moreover, there is no equation to compute the average stresses throughout rectangular element faces. This made computer code development very difficult and time-consuming. To analyze displacement, strain, and stress fields components, if a field point (say grid-node) is close to a rectangular source (say boundary element) it must be placed near the middle point of the element since equilibrium equation is established on that point not the whole element. Establishing equilibrium equation for whole element needs analysis of average stresses which is so laborious and makes the formulation worthless. Another shortcoming of our method emerges when dealing with

multiple fractures. The aspect ratios of elements should not exceed 1.20. Moreover, ratio of longer edge of a boundary element in fracture  $i$  to the same edge in fracture  $j$  should not exceed 1.1. And if fractures are too close to each other, the longest edge of boundary elements should be less than half of smallest fracture spacing. Our recommendation is maximum 40% of minimum fracture spacing. If these ratios are not followed, the stiffness matrix becomes asymmetric which impacts numerical performance of our procedure. As mentioned, asymmetric stiffness matrix is a sign of lack of equilibrium in the model and should be avoided. These conditions make computer programming so difficult. But the silver bullet in our proposed method is having high accuracy in a very short amount of time. Finally, the numerical method was used to solve some examples and was verified using some well-known problems.

## 5.2. Findings During Simulator Development

At least two phenomena were discovered during procedure and computer code developments

- **Displacement Field Interaction:** in the example of 2-Stage multi-cluster fracture, it was discovered that fractures push each other during pressurization. Mid-planes of fractures don't remain straight especially when cluster spacing is relatively low. Moreover, fractures in the middle of the stage experience significantly less aperture (opening) comparing to outer fractures. This phenomenon has been pointed out in numerous research papers.
- **Stress Shadowing Effect:** It was also found out that pressurization of multi-stage multi-cluster fractures can significantly disturb reservoir stress field by deviating



direction of minimum and maximum in-situ stresses. This was carried out by eigenpair analysis and finding direction and magnitude of principal stress vectors. Since fracture is propagated along with two maximum principal stresses, this interaction can significantly impact direction and shape of fractures if they are within stress shadow window.

### 5.3. Some Recommendations for Future Developments

Here, we itemize some recommendations for future work:

1. Initial shape of fracture(s) is either horizontal or vertical. An improvement is required to model and simulate inclined fractures. It is crucial to deal with natural fractures and faults.
2. Local  $z$ -axis of fractures is parallel to global  $x_2$ -axis. To deal with natural fractures and faults an improvement is inevitable.
3. Implement non-uniform pressure using fluid flow equation
4. All reservoirs have very complicated natural fracture and fault networks. Interaction of hydraulic and natural fractures has significant effects on fracture design and well productivity.

## Nomenclature (English)

$B.C.^E$  = Essential, or Geometrical Boundary Condition

$B.C.^N$  = Natural, or Forced Boundary Condition

$c$  = Depth of a Reference Point in a Boundary Element

$d\Sigma$  = Differential Element in a Boundary Element Surface

$\mathbf{e}_i$  = Unit Vectors corresponding to Cartesian Frame Axes

$E$  = Normal Elastic Modulus

$F$  = Magnitude of Force Vector  $\mathbf{F}$

$F_i^{bc}$  = Body Force Equivalent Concentrated Force

$\mathbf{F}$  = Force Vector

$\mathbf{F}^b$  = Vector Representing Body Force

$G$  = Shear Elastic Modulus

$\mathbf{G}$  = Loading Matrix

$f_{i,j} = \frac{\partial f_i}{\partial x_j}$  ( $i, j=1, 2, 3$ )

$f_{i,i} = \sum_{i=1}^3 \frac{\partial f_i}{\partial x_i}$

$\mathbf{K}$  and  $\hat{\mathbf{K}}$  = Stiffness Matrix

$L$  = Length of a Rectangular Discontinuous Source

$\mathbf{n}$  and  $n_i$  = Normal Vector of a Surface Element

$NBE$  = Total Number of BE's in the model

$p_j$  =  $j$ th component of Traction at RABE Surface

$\mathbf{r}$  = Position Vector

$R$  = Radial Distance

$t_i$  = Traction Component  $i$

$\mathbf{t}_i$  = Traction Vector of BE  $i$

$\mathbf{T}$  = Traction Vector

$\mathbf{T}^k$	= Traction Vector due to a unit force along $x_k$ direction
$\mathbf{u}$	= Displacement Field Vector
$\mathbf{U}$	= Dislocation Vector
$U_i^m$	= Dislocation value in RABE $m$ , in $DOF_i$ ( $i=1, 2, \text{ and } 3$ )
$U_i$	= Dislocation value in $DOF_i$ ( $i=1, 2, \dots, nDOF$ )
$u_k$	= $k$ th component of displacement field ( $k=1, 2, 3$ )
$u_i^k$	= $u_i$ due to $k$ th component of Force Vector $\mathbf{F}$
$\mathbf{u}_i$	= Displacement Vector of BE $i$
$v_p$ and $v_s$	= P-Wave and S-Wave Velocities of the Medium
$V$	= Potential Function
$w$ and $w_i$	= Width of a Rectangular Discontinuous Source
$x_i$	= Cartesian Coordinates of a point in a domain

### Nomenclature (Greek)

$\alpha$	= Medium Constant
$\delta$	= Dip Angle of a Discontinuous Plane
$\delta_{ij}$	= Kronecker Delta
$\Delta\mathbf{u}$	= Displacement Discontinuity Vector
$\boldsymbol{\varepsilon}$ and $\varepsilon_{ij}$	= Strain Tensor
$\Phi_i$	= Scalar Components of Galerkin Vector
$\Phi$	= Galerkin Vector
$\gamma_{Max}$	= Maximum Shearing Strain
$\Gamma = \partial\Omega$	= Boundary of the Model Domain $\Omega$
$\mu$ and $\lambda$	= Lamé Constants
$\nu$	= Poisson's Ratio
$\pi$	= Pi number (= 3.14159462...)
$\Omega$	= Model Domain

$\Omega$	= Dislocation Matrix
$\mathbf{v}$ and $v_i$	= Normal Vector of a Surface Element
$\boldsymbol{\sigma}$ and $\sigma_{ij}$	= Stress Tensor
$\sigma_{ij}^k$	= $\sigma_{ij}$ due to $k$ th component of Force Vector $\mathbf{F}$
$(\sigma_{in-situ})_j$	= $j$ th component of In-Situ Stress
$\Sigma$	= Boundary Element Surface
$\tau_{Max}$	= Maximum Shearing Stress
$\xi_i$	= Cartesian Coordinates of a point in a fracture plane/surface
$\Psi_i$	= Scalar Components of Galerkin Vector
$\Psi$	= Galerkin Vector

## Abbreviations

BE	= Boundary Element
BEM	= Boundary Element Method
DD	= Displacement Discontinuity
DDDv	= Displacement/Displacement Derivative
DDM	= Displacement Discontinuity Method
DOF	= Degree of Freedom
DOF <sub><math>i</math></sub>	= $i$ th Degree of Freedom ( $i=1, 2, \text{ and } 3$ )
DSL	= Dip-Slip-Like
$i$ DOF	= $i$ th Degree of Freedom in the model ( $i=1, 2, \dots, n$ DOF)
$j$ DOF	= $j$ th Degree of Freedom in the model ( $j=1, 2, \dots, n$ DOF)
$n$ DOF	= Number of available DOFs in the model
EGS	= Enhanced Geothermal System
FDM	= Finite Difference Method
FEM	= Finite Element Method
FSM	= Fictitious Stress Method
KGD	= Khristianovich-Geertsma-de Klerk Model
RABE	= Rectangular Boundary Element

*RSOLE* = *Real System of Linear Equations*  
*XFEM* = *Extended Finite Element Method*  
*HF* = *Hydraulic Fracturing*  
*Obs.* = *Observation*  
*Obs. P.* = *Observation Point (Same as PoI)*  
*PDE* = *Partial Differential Equation*  
*PKN* = *Perkins-Kern-Nordgren Model*  
*PoI* = *Point of Interest (Same as Obs. P.)*  
*RABE* = *Rectangular Boundary Element*  
*SER* = *Strain Energy Release*  
*SIF* = *Stress Intensity Factor*  
*SSL* = *Strike-Slip-Like*  
*TL* = *Tensile-Like*

## References

- Abbas, S., Gordeliy, E., Peirce, A., Lecampion, B., Chuprakov, D., and Prioul, R. (2014). “Limited Height Growth and Reduced Opening of Hydraulic Fractures due to Fracture Offsets: An XFEM Application.” *SPE Hydraulic Fracturing Technology Conference*, Society of Petroleum Engineers, 13.
- Bonafede, M., Dragoni, M., and Quarenì, F. (1986). “Displacement and stress fields produced by a centre of dilation and by a pressure source in a viscoelastic half-space: application to the study of ground deformation and seismic activity at Campi Flegrei, Italy.” *Geophysical Journal International*, 87(2), 455–485.
- Brebbia, C. A. (2017). “The Birth of the Boundary Element Method from Conception to Application.” *Engineering Analysis with Boundary Elements*, 77(December 2016), iii–x.
- Chinnery, M. A. (1961). “The deformation of the ground around surface faults.” *Bulletin of the Seismological Society of America*, 51(3), 355–372.
- Economides Michael J., and Nolte, K. G. (2000). *Reservoir Stimulation*. Wiley.
- Fialko, Y., Khazan, Y., and Simons, M. (2001). “Deformation due to a pressurized horizontal circular crack in an elastic half-space, with applications to volcano geodesy.” *Geophysical Journal International*, 146(1), 181–190.
- Fu, P. (2014). *Surface Deformation from a Pressurized Subsurface Fracture: Problem Description*.
- Gale, J. F. W., Laubach, S. E., Olson, J. E., Eichhubl, P., and Fall, A. (2014). “Natural fractures in shale: A review and new observations.” *AAPG Bulletin*, 98(11), 2165–2216.
- Ghassemi, A., and Zhou, X. (2011). “A three-dimensional thermo-poroelastic model for fracture response to injection/extraction in enhanced geothermal systems.” *Geothermics*, CNR-Istituto di Geoscienze e Georisorse, 40(1), 39–49.

- Ghassemi, A., Zhou, X. X., and Rawal, C. (2013). “A three-dimensional poroelastic analysis of rock failure around a hydraulic fracture.” *Journal of Petroleum Science and Engineering*, Elsevier, 108, 118–127.
- Guo, T., Gong, F., Wang, X., Lin, Q., Qu, Z., and Zhang, W. (2019). “Performance of enhanced geothermal system (EGS) in fractured geothermal reservoirs with CO<sub>2</sub> as working fluid.” *Applied Thermal Engineering*, Elsevier, 152(July 2018), 215–230.
- Gupta, K. K., and Meek, J. L. (1996). “A BRIEF HISTORY OF THE BEGINNING OF THE FINITE ELEMENT METHOD.” *International Journal for Numerical Methods in Engineering*, 39(22), 3761–3774.
- He, Q., Suorineni, F. T., Ma, T., and Oh, J. (2017). “Effect of discontinuity stress shadows on hydraulic fracture re-orientation.” *International Journal of Rock Mechanics and Mining Sciences*, Elsevier, 91(November 2016), 179–194.
- Huang, K. (2015). “NUMERICAL SIMULATIONS OF FRACTURE PROPAGATION APPLIED TO PETROLEUM AND GEOTHERMAL RESERVOIR USING FINITE ELEMENT METHOD.” *A Dissertation*, University of Oklahoma.
- Huang, K., Zhang, Z., and Ghassemi, A. (2013). “Modeling Three-Dimensional Hydraulic Fracture Propagation Using Virtual Multidimensional Internal Bonds.” *International Journal for Numerical and Analytical Methods in Geomechanics*, 37(13), 2021–2038.
- Hussain, T., Memon, A., Lashari, Z. A., Hussain, T., Memon, A., and Lashari, Z. A. (2017). “ENVIRONMENTAL IMPACTS OF SHALE GAS EXPLOITATION.” *Australian Journal of Engineering and Technology Research*, 2(April), 4–2017.
- Katsikadelis, J. T. (2016). *The Boundary Element Method for Engineers and Scientists*. Academic Press.
- Kumar, D., and Ghassemi, A. (2016). “A three-dimensional analysis of simultaneous and sequential fracturing of horizontal wells.” *Journal of Petroleum Science and Engineering*, Elsevier, 146, 1006–1025.
- Mindlin, R. D. (1936). “Force at a Point in the Interior of a Semi-Infinite Solid.” *Physics*, 7(5), 195–202.

- Moës, N., Dolbow, J., and Belytschko, T. (1999). “A finite element method for crack growth without remeshing.” *International Journal for Numerical Methods in Engineering*, 46(1), 131–150.
- Okada, Y. (1985). “Surface deformation due to shear and tensile faults in a half-space.” *Bulletin of the Seismological Society of America*, 75(4), 1135–1154.
- Okada, Y. (1992). “Internal deformation due to shear and tensile faults in a half space.” *Bulletin of the Seismological Society of America*, 82(2), 1018–1040.
- Ouchi, H., Katiyar, A., Foster, J., and Sharma, M. M. (2015). “A Peridynamics Model for the Propagation of Hydraulic Fractures in Heterogeneous, Naturally Fractured Reservoirs.” *SPE Hydraulic Fracturing Technology Conference*, Society of Petroleum Engineers.
- Pollard, D. D., and Holzhausen, G. (1979). “On the Mechanical Interaction Between a Fluid-Filled Fracture and the Earth’s Surface.” *Tectonophysics*, 53(1–2), 27–57.
- Rainbolt, M. F., and Esco, J. (2018). “Frac Hit Induced Production Losses: Evaluating Root Causes, Damage Location, Possible Prevention Methods and Success of Remediation Treatments, Part II.” *SPE Hydraulic Fracturing Technology Conference*, Society of Petroleum Engineers.
- Sesetty, V., and Ghassemi, A. (2015). “A numerical study of sequential and simultaneous hydraulic fracturing in single and multi-lateral horizontal wells.” *Journal of Petroleum Science and Engineering*, Elsevier, 132, 65–76.
- Steketee, J. A. (1958). “ON VOLTERRA’S DISLOCATIONS IN A SEMI-INFINITE ELASTIC MEDIUM.” *Canadian Journal of Physics*, 36(2), 192–205.
- Valkó, P., and Economides, M. J. (1996). “Hydraulic fracture mechanics.” *Strain*, 32(4), 147–148.
- Verde, A., and Ghassemi, A. (2015). “Modeling injection/extraction in a fracture network with mechanically interacting fractures using an efficient displacement discontinuity method.” *International Journal of Rock Mechanics and Mining Sciences*, Elsevier, 77, 278–286.
- Volterra, V. (1907). “Sur l’équilibre des corps élastiques multiplément connexes.” *Annales scientifiques de l’École normale supérieure*, 24, 401–517.



- Wang, X. (2014). “THREE-DIMENSIONAL FEM MODELING OF GEOTHERMAL RESERVOIR STIMULATION USING STOCHASTIC FRACTURE NETWORKS AND CONTINUUM DAMAGE MECHANICS.” *A Dissertation*, University of Oklahoma.
- Wu, R., Kresse, O., Weng, X., Cohen, C.-E., and Gu, H. (2013). “Modeling of Interaction of Hydraulic Fractures in Complex Fracture Networks.” *SPE Hydraulic Fracturing Technology Conference*, (1995).
- Xiang, J. (2011). “A PKN hydraulic fracture model study and formation permeability determination.” *A Thesis*, Texas A&M University.
- Youn, S. (1993). “Application of Displacement and Traction Boundary Integral Equations for Fracture Mechanics Analysis.” Iowa State University.
- Zhang, F., and Mack, M. (2017). “Integrating fully coupled geomechanical modeling with microseismicity for the analysis of refracturing treatment.” *Journal of Natural Gas Science and Engineering*, Elsevier B.V, 46, 16–25.

**Appendix A: Explanation of Parameters and Variables Involved in Equations Which Are Given in Table 2.3 to Table 2.6**

For better understanding of all parameters and variables that are included in equations, Figure A. 1 is illustrated. It shows a side view of a rectangular source with its image pair. It needs to be mentioned that axis  $\xi$  is perpendicular to the page at observation point and it is inward.

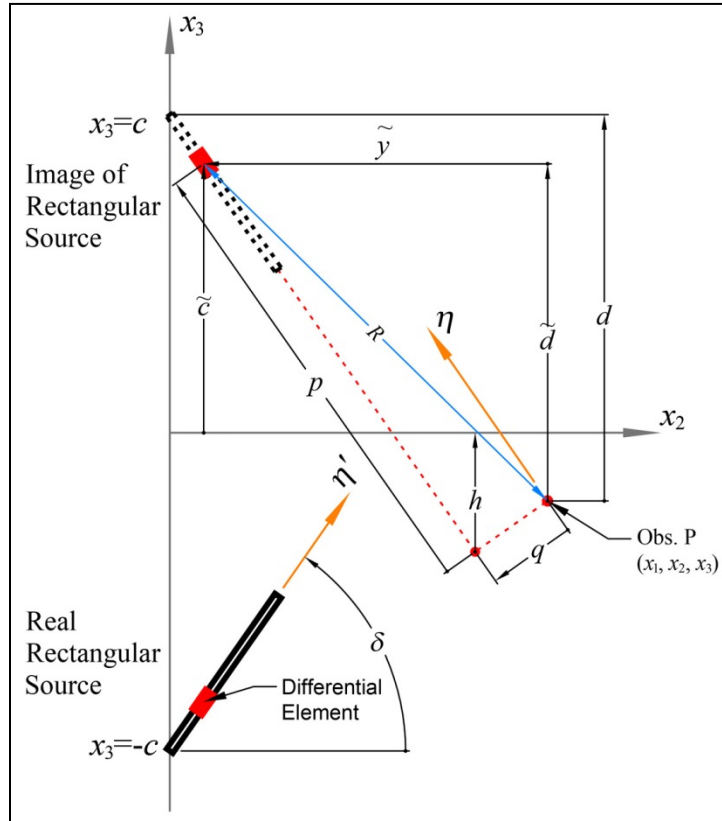


Figure A. 1—Side view of A finite rectangular source with its image pair. Axes  $x_1$ ,  $\xi$ , and  $\xi'$  are perpendicular to the page. Axes  $x_1$  and  $\xi'$  are outward, but axis  $\xi$  at observation point is inward.

However, axis  $\xi'$  is perpendicular at  $x_3 = -c$ . Axis  $x_1$  is perpendicular at origin of global coordinate system  $Ox_1x_2x_3$ . Both  $\xi'$  and  $x_1$  are outward. To find the influence of rectangular source at observation point, the influence of a differential source has to be integrated along the rectangular source. Namely,

$$\left\{ \begin{array}{l} F_{\Sigma}(x_1, x_2, x_3) = \int_0^L \int_0^W f(\xi', \eta') d\xi' d\eta' = \int_{x_1}^{x_1-L} \int_p^{p-W} f(\xi, \eta) d\xi d\eta \\ \xi = x_1 - \xi' \\ \eta = p - \eta' \\ p = x_2 \cos \delta + d \sin \delta \\ q = x_2 \sin \delta - d \cos \delta \\ d = c - x_3, \text{ Note: } c = \text{Depth} \geq 0 \text{ and } x_3 \leq 0 \end{array} \right. \quad (\text{A.1})$$

In Figure A. 1, and Table 2.3 to Table 2.6 we have,

$$\left\{ \begin{array}{l} x_1, x_2, \text{ and } x_3 : \text{Coordinates of Observation Point} \\ d = c - x_3 \\ p = x_2 \cos \delta + d \sin \delta \\ q = x_2 \sin \delta - d \cos \delta \\ h = q \cos \delta - x_3 \\ \tilde{y} = x_2 - (p - \eta) \cos \delta = \eta \cos \delta + q \sin \delta \\ \tilde{d} = d - (p - \eta) \sin \delta = \eta \sin \delta - q \cos \delta \\ \tilde{c} = \tilde{d} + x_3 = \eta \sin \delta - h \\ R = \sqrt{\xi^2 + \eta^2 + q^2} = \sqrt{\xi^2 + \tilde{y}^2 + \tilde{d}^2} \end{array} \right. \quad (\text{A.2})$$

Variables in (A.2) are Cartesian-Coordinate related. They are derived to convert Cartesian frame from Global  $Ox_1x_2x_3$  to Local  $P\xi\eta$  which is attached to point of interest (say observation point) and parallel to discontinuous rectangular image source. This conversion simplifies the analysis significantly and eliminates most of the negative signs.

To condensate long equations in above-mentioned tables, some other parameters are introduced below which are either material-related or Geometry-related. All the variables and parameters in Equations (A.1) and (A.2) are required in all tables. Moreover, To compute functions in all tables, parameters  $X_i, Y_i, Z_i, X_{mn}, Y_{mn},$  and  $Z_{mn}$  need to be calculated from Equation (A.3).

$$\begin{aligned}
\alpha &= \frac{\lambda + \mu}{\lambda + 2\mu} = 1 - \left( \frac{v_s}{v_p} \right)^2 & ; & \quad \Theta = \tan^{-1} \left( \frac{\xi \eta}{qR} \right) \\
\hline
X_{11} &= \frac{1}{R(R + \xi)} & ; & \quad X_{32} = \frac{2R + \xi}{R^3(R + \xi)^2} & ; & \quad X_{53} = \frac{8R^2 + 9R\xi + 3\xi^2}{R^5(R + \xi)^3} \\
Y_{11} &= \frac{1}{R(R + \eta)} & ; & \quad Y_{32} = \frac{2R + \eta}{R^3(R + \eta)^2} & ; & \quad Y_{53} = \frac{8R^2 + 9R\xi + 3\xi^2}{R^5(R + \xi)^3} \\
Z_{11} &= 1 \text{ (Omitted)} & ; & \quad Z_{32} = \frac{\sin \delta}{R^3 - hY_{32}} & ; & \quad Z_{53} = \frac{8R^2 + 9R\eta + 3\eta^2}{R^5(R + \eta)^3} \\
\hline
X &= \sqrt{\xi^2 + q^2} & ; & \quad Y_0 = Y_{11} - \xi^2 Y_{32} & ; & \quad Z_0 = Z_{32} - \xi^2 Y_{53}
\end{aligned} \tag{A.3}$$

To compute parameters  $I_i$  in Table 2.3, Equations in (A.4) are required.

$$\begin{cases}
I_1 = \frac{\sin \delta}{\cos \delta} \frac{\xi}{R + \tilde{d}} + \frac{2}{\cos^2 \delta} \tan^{-1} \left[ \frac{\eta(X + q \cos \delta) + X(R + X) \sin \delta}{\xi(R + X) \cos \delta} \right] \\
\text{Note: for } \delta = \frac{\pi}{2} \text{ or } \frac{3\pi}{2}: I_1 = \frac{1}{2} \frac{\xi \tilde{y}}{(R + \tilde{d})^2}
\end{cases} \tag{A.4}$$

$$\begin{cases}
I_2 = \frac{1}{\cos \delta} \frac{\xi}{R + \tilde{d}} - \frac{1}{\cos^2 \delta} \left[ \ln(R + \eta) - \sin \delta \cdot \ln(R + \tilde{d}) \right] \\
\text{Note: for } \delta = \frac{\pi}{2} \text{ or } \frac{3\pi}{2}: I_2 = \frac{1}{2(R + \tilde{d})} \left[ \eta + \frac{\tilde{y}q}{R + \tilde{d}} - \ln(R + \eta) \right]
\end{cases}$$

$$\begin{cases} I_3 = \ln(R + \tilde{d}) + I_2 \sin \delta \\ I_4 = -\frac{\xi}{R + \tilde{d}} \cos \delta - I_1 \sin \delta \end{cases} \quad (\text{A.4-Continued})$$

Before computing parameters  $J_i$ ,  $K_i$ , and  $L_i$ , some intermediate parameters are necessary to be calculated. These are:

$$\begin{aligned} D_1 &= \frac{1}{R(R + \tilde{d})} \quad ; \quad D_2 = qY_{11} - \tilde{y}D_1 \quad ; \quad D_3 = \tilde{d} + \frac{\tilde{y}^2}{R + \tilde{d}} \\ D_4 &= \frac{\xi\tilde{y}}{R + \tilde{d}} \quad ; \quad D_5 = D_1 - Y_{11} \sin \delta \quad ; \quad D_6 = Y_{11} - D_1 \sin \delta \end{aligned} \quad (\text{A.5})$$

Parameters  $J_i$  in Equations (A.6) have to be calculated and, then, be substituted in Table 2.4.

$$\begin{aligned} J_1 &= -\frac{\sin \delta}{\cos^2 \delta} D_2 - \frac{1}{\cos \delta} D_3 \quad ; \quad J_2 = D_1 D_4 \quad ; \quad J_3 = -\frac{\sin \delta}{\cos \delta} J_2 + \frac{\xi}{\cos^2 \delta} D_5 \\ J_4 &= -\frac{1}{\cos \delta} D_4 - \frac{\xi}{\cos^2 \delta} D_6 \quad ; \quad J_5 = -D_1 D_3 \quad ; \quad J_6 = \frac{\sin \delta}{\cos \delta} J_5 + \frac{1}{\cos^2 \delta} D_2 \end{aligned} \quad (\text{A.6})$$

Moreover, parameters  $E$  to  $Q$ , and  $K_i$ , can be calculated by means of Equations (A.7) to use in Table 2.5.

$$\begin{aligned} E &= \frac{\sin \delta}{R} - \frac{\tilde{y}q}{R^3} \quad ; \quad F = \frac{\tilde{d}}{R^3} + \xi^2 Y_{32} \sin \delta \quad ; \quad G = 2X_{11} \sin \delta - \tilde{y}qX_{32} \\ H &= \tilde{d}qX_{32} + \xi qY_{32} \sin \delta \quad ; \quad P = \frac{\cos \delta}{R^3} + qY_{32} \sin \delta \quad ; \quad Q = \frac{3\tilde{c}\tilde{d}}{R^5} - (x_3 Y_{32} + Z_{32} + Z_0) \sin \delta \\ \hline K_1 &= J_4 + \xi Y_{11} \quad ; \quad K_2 = J_5 + \frac{1}{R} \quad ; \quad K_3 = -J_6 + qY_{11} \\ K_4 &= J_1 \quad ; \quad K_5 = J_2 \quad ; \quad K_6 = J_3 \end{aligned} \quad (\text{A.7})$$

And finally, before computing equations in Table 2.6, parameters  $E'_i$  to  $H'_i$  along with  $L_i$  have to be obtained from Equations (A.8).

$$\begin{aligned}
 E' &= \frac{\cos \delta}{R} + \frac{\tilde{d}q}{R^3} & ; & \quad F' = \frac{\tilde{y}}{R^3} + \xi^2 Y_{32} \cos \delta & ; & \quad G' = 2X_{11} \cos \delta + \tilde{d}qX_{32} \\
 H' &= \tilde{y}qX_{32} + \xi qY_{32} \cos \delta & ; & \quad P' = \frac{\sin \delta}{R^3} - qY_{32} \cos \delta & ; & \quad Q' = \frac{3\tilde{c}\tilde{y}}{R^5} + qY_{32} - \begin{pmatrix} x_3 Y_{32} \\ + Z_{32} \\ + Z_0 \end{pmatrix} \cos \delta
 \end{aligned}
 \tag{A.8}$$


---


$$\begin{aligned}
 L_1 &= \frac{\xi}{\cos \delta} D_5 & ; & \quad L_2 = \tilde{y}D_1 & ; & \quad L_3 = \frac{1}{R} + \frac{\sin \delta}{\cos \delta} D_2 \\
 L_4 &= \frac{1}{\cos \delta} D_2 & ; & \quad L_5 = \xi D_1 & ; & \quad L_6 = \frac{\xi}{\cos \delta} D_6
 \end{aligned}$$

## **Appendix B: Capabilities of HiFrac 3D**

### **B.1. Discretization of Fracture(s)**

Since Okada solution is valid for just rectangular element, fractures of arbitrary shapes have to be discretized into Rectangular Boundary Elements (RABEs). In other words, a mesh of BEs at fracture surfaces is required to be generated. Along the thesis, Mesh Generation means Fracture Discretization or, shortly, Discretization. To define an agreeable discretization, some assumptions ought to be made.

- Fracture(s) is/are circular (penny-shaped) or Rectangular shapes. However, it is not an inherent shortcoming and they can be of any shape. Penny-shaped or Rectangular fracture(s) are just our case studies for verification and validation purposes.
- Fracture plane is either horizontal or vertical, but it is not a theoretical mandate. By conducting some simple improvements in our tools, oblique fractures can be modeled.
- Pressure due to fluid injection throughout each individual fracture is constant, however it is not a theoretical limit. Variable pressure profile can be applied by some simple improvements in our research tools.
- There is no limit for number of individual fractures or group of fractures (Frac Stages). Furthermore, Fractures may have any arrangements (such as sequential-frac or zipper-frac). However, their initial planes must be parallel.

## **B.2. Grid Generation in the Model Domain**

Since our method does not need domain discretization it, indeed, needs a domain grid to obtain all geometrical parameters (such as displacements) and mechanical parameters (such as stresses) at points. For simplicity, these points are located at intersection of gridlines which are called Grid-Points or Grid-Nodes. Grids are independent from discretizations, but for better graphical illustrations it is preferred that the grids become conformable with BE Meshes in the vicinity of fracture surfaces.

## **B.3. Analysis of Dislocations**

The term dislocation is defined as magnitude of relative displacements between two separate fracture surfaces. It can, also, be called Fracture Aperture. All dislocation components have to be analyzed in order to carry out displacement and displacement derivative (DDDv) fields computations at grid-nodes by means of Okada formulation. They are required to obtain fracture geometry during pressurizing and next upcoming steps. Because of mesh and grid independency, the grid can be altered without need to perform new analysis. Nevertheless, any change in BE mesh will mandate a fresh analysis.

## **B.4. Analysis of Displacement/Displacement**

### **Derivative Fields**

Analysis of displacement and displacement derivative fields is fundamental part of our method in that we need to monitor geometry and morphology of fracture(s) during fluid injection to detect possible fracture hit in the case of multiple fracture process. Moreover, fracture geometry, i.e. dimensions and aperture, is necessary to analyze and estimate productivity and performance of a fractured well. In addition, according to Equation



(2.11), derivative of displacement field components are required to compute strain and stress components. HiFrac 3D is able to compute all the required DDDv components at each and every grid-node. It needs to be reminded that all partial derivatives are computed based on closed-form analytical functions discussed in CHAPTER 2. Hence, we don't need to compute them numerically by using Finite Difference Method or similar methods. The only numerical step of our method is discretization of the fracture(s) to approximate its/their geometry.

### **B.5. Strain and Stress Analysis**

By all displacement derivative field components on hand that obtained from above step, all the Cauchy Strain components are computed. These components along with material properties of the domain (reservoir rock) give all the Cauchy Stress components.

### **B.6. Principal Strains, Principal Stresses, and Maximum Shear Strain/Stress**

The next step is to analyze and obtain values of principal strains and stresses and their corresponding directions. The values and directions of principal strain/stress are resulted to Maximum Shear Strain/Stress. They are very useful to analyze and locate rock failure as a preliminary assessment. For more accurate rock failure analysis, more advanced and comprehensive failure criteria need to be utilized.

### **B.7. Use of Tools**

A computer code to implement the proposed formula is discussed. For the sake of honesty and copyright laws all the utilized tools, codes and softwares are introduced here.

First part of the computer code, which is called “HiFrac 3D” was developed in PGI FORTRAN 18.5 which supports “New Generation FORTRAN” standards. Due to end of support for integration with Microsoft Visual Studio, the code was transferred to “Intel Parallel Studio XE 2018 and 19” for compilation. Its programming standards are slightly different from PGI FORTRAN. To solve a Real System of Linear Equations (RSOLE), LAPACK package was used which consists of hundreds of useful sub-programs for numerical analysis. LAPACK, which stands for Linear Algebra PACKage was developed in C, C++, and FORTRAN languages by “The University of Tennessee”, “The University of California, Berkeley”, “The University of Colorado, Denver”, and “Numerical Algorithms Group (NAG) Ltd.”. Moreover, to carry out Eigenpair Analysis (Eigenvalues and Eigenvectors), Jacobi method was used. The computer code for Eigenpair analysis was developed by John Burkardt at Florida State University. And finally, Okada, has developed a code for his formulation which computes components of displacement and displacement derivatives fields for one single finite rectangular source. His code was developed in FORTRAN 77 language. For the sake of consistency and compatibility, it is converted to new generation FORTRAN (FORTRAN 90-2013) in our code.

Second part of HiFrac3D, is developed in MATLAB for the purpose of Data Visualization. MATLAB, which is a comprehensive package for analysis, visualization and simulation, has thousands of sub-programs and toolboxes. It is widely used by researchers and companies.

The formulation and computer codes are new-of-a-kind, so further developments will be necessary to overcome limitations and create more sophisticated models.

## B.8. An Example of a Single-Fracture Model

To show the capabilities of HiFrac 3D, a few examples are provided here. First, we assume input values according to Table B. 1. It needs to be mentioned that the values in Table B. 1 do not belong to a real field data but they were picked so that do not violate basics of rock properties. For instance, in-situ stresses and average rock specific density (to calculate overburden stress) are selected carefully.

Table B. 1— Initial Values and Properties for a Single HF Model

Parameter or Property	Value	Unit
Elastic Modulus	$E = 0.3404 \times 10^6$	psi
Poisson's Ratio	$\nu = 0.26$	Unitless
Min. Hor. In-Situ Stress	$S_{\min}^H = -2600$	psi
Max. Hor. In-Situ Stress	$S_{\max}^H = -2725$	psi
Average Specific Density of Rock	$\gamma = 85$	pcf
Depth of Injection Point	$D = 4760$	ft.
Radius of Hydraulic Fractures	$R = 60$	ft.
Extent of the Model Domain	$240 \times 240 \times 240$	ft.
Fracture Orientation	Vertical ( $\delta = 90^\circ$ )	
RABE Mesh Size	$15 \times 15$	
No. of Grid Spacing Outside Frac.	9	
Injection Pressure at Depth	$2720 (\Delta p = 120)$	psi

All the graphical results are illustrated in Figure B. 1 to Figure B. 13.

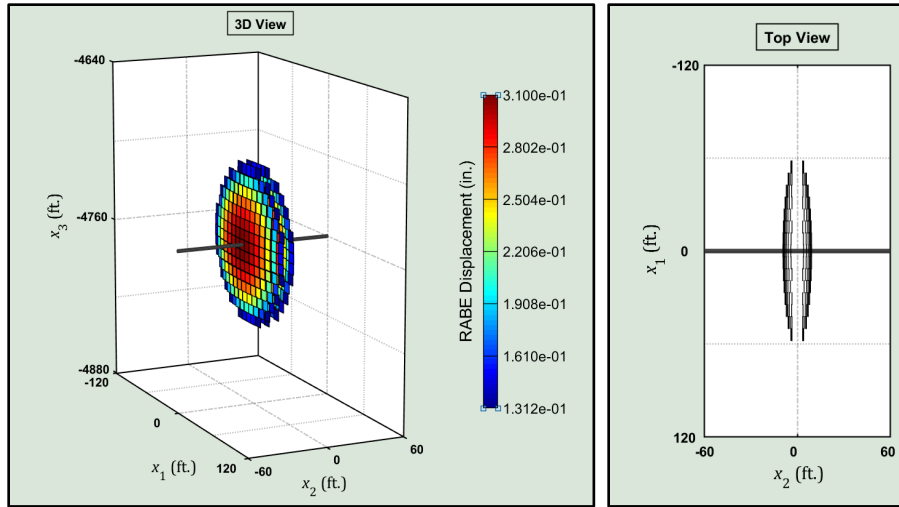


Figure B. 1—Geometry of the Fracture After Fluid Injection

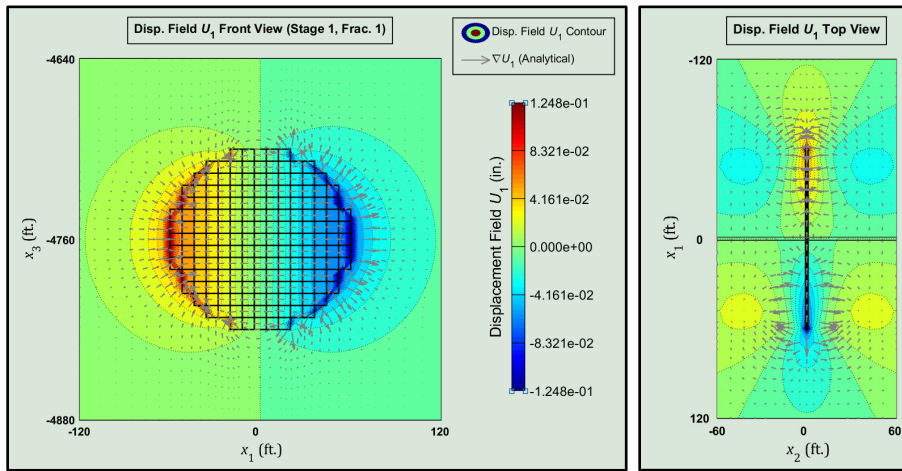


Figure B. 2—Displacement Field  $u_1$  in Model Domain and Its Gradient

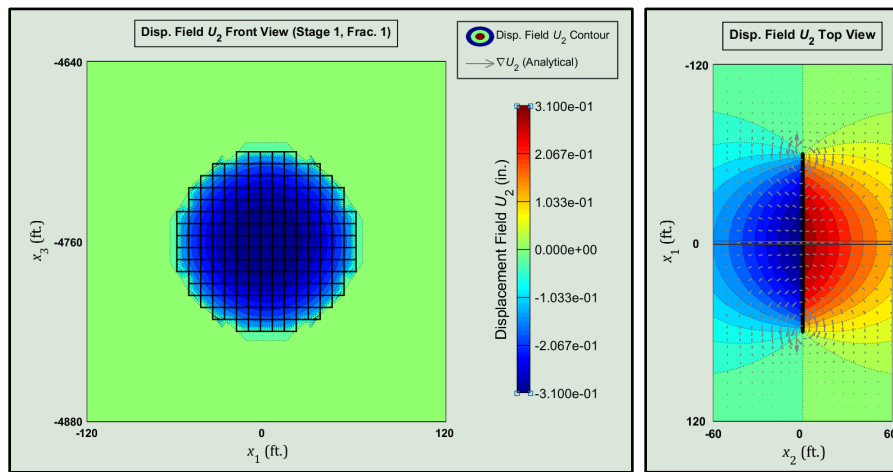


Figure B. 3—Displacement Field  $u_2$  in Model Domain and Its Gradient

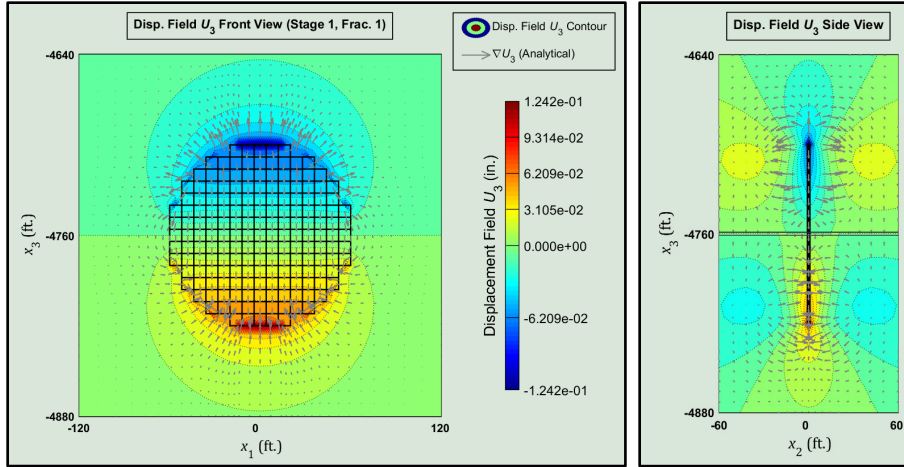


Figure B. 4—Displacement Field  $u_3$  in Model Domain and Its Gradient

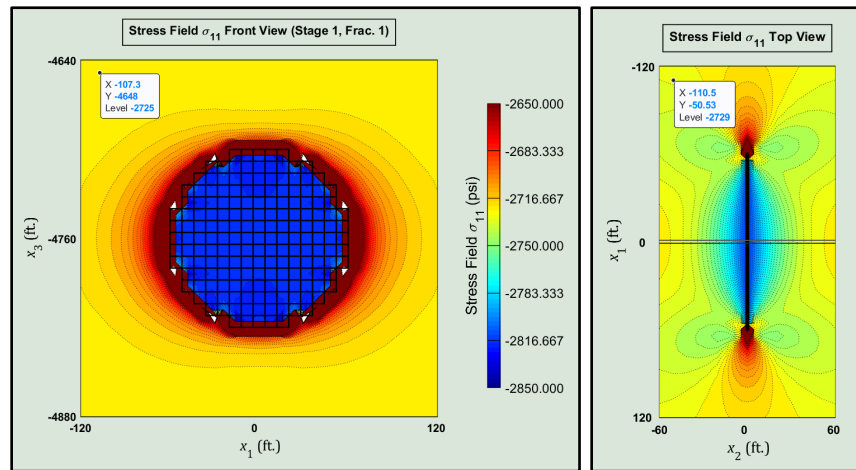


Figure B. 5— Normal Stress Field  $\sigma_{11}$  in Model Domain

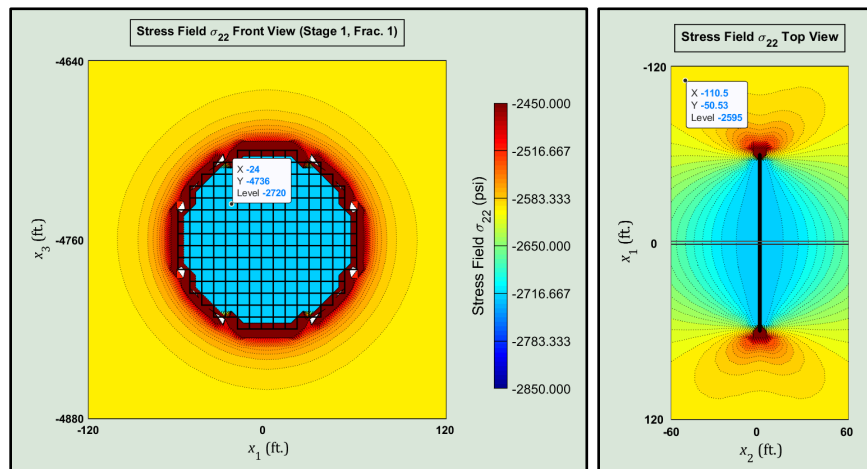


Figure B. 6— Normal Stress Field  $\sigma_{22}$  in Model Domain

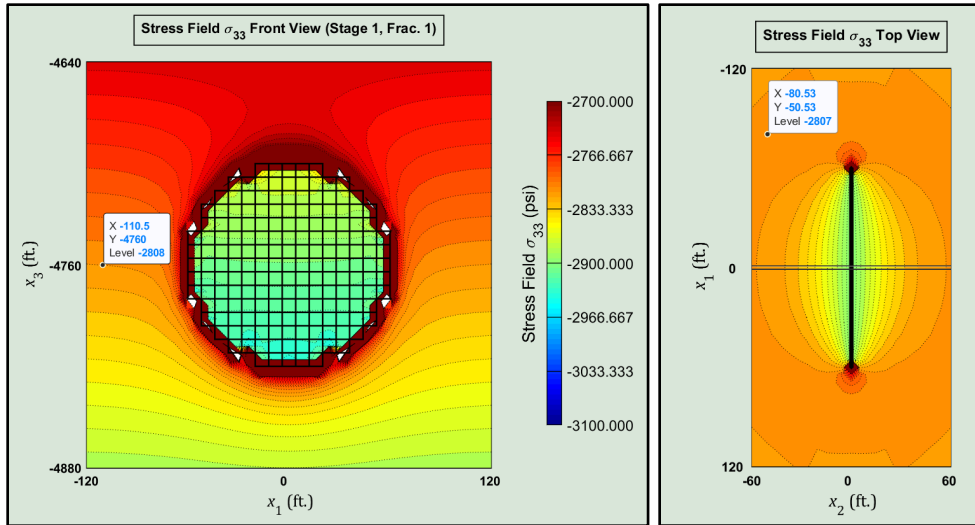


Figure B. 7—Normal Stress Field  $\sigma_{33}$  in Model Domain

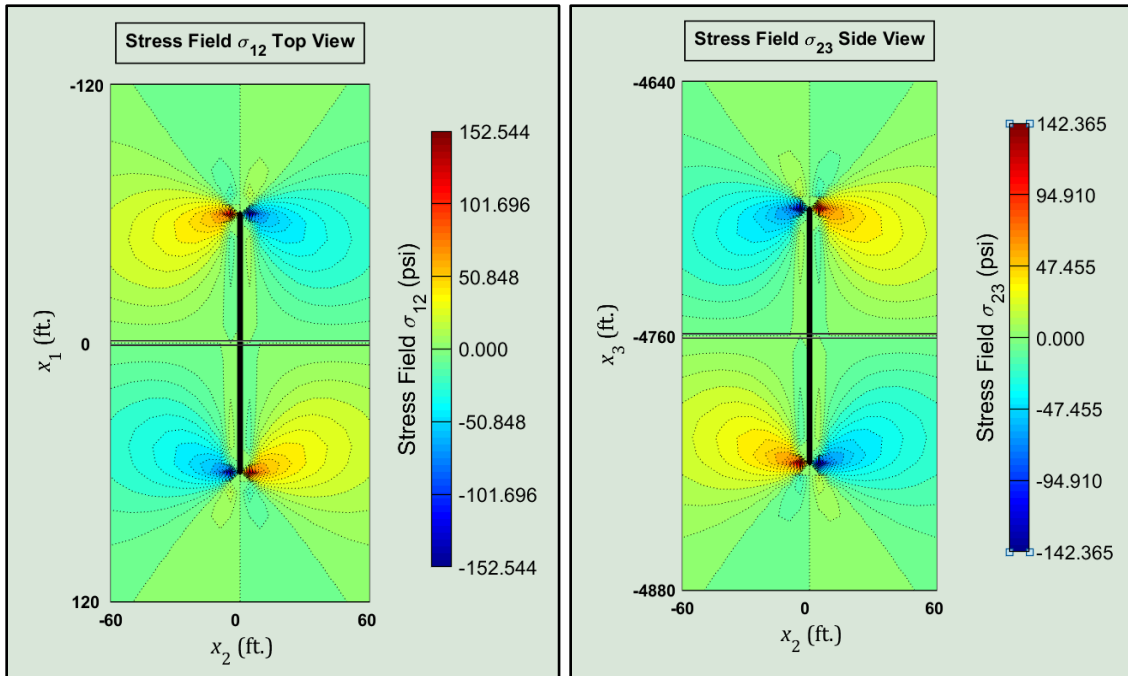


Figure B. 8—Shear Stress Fields  $\sigma_{12}$ ,  $\sigma_{23}$  in Model Domain

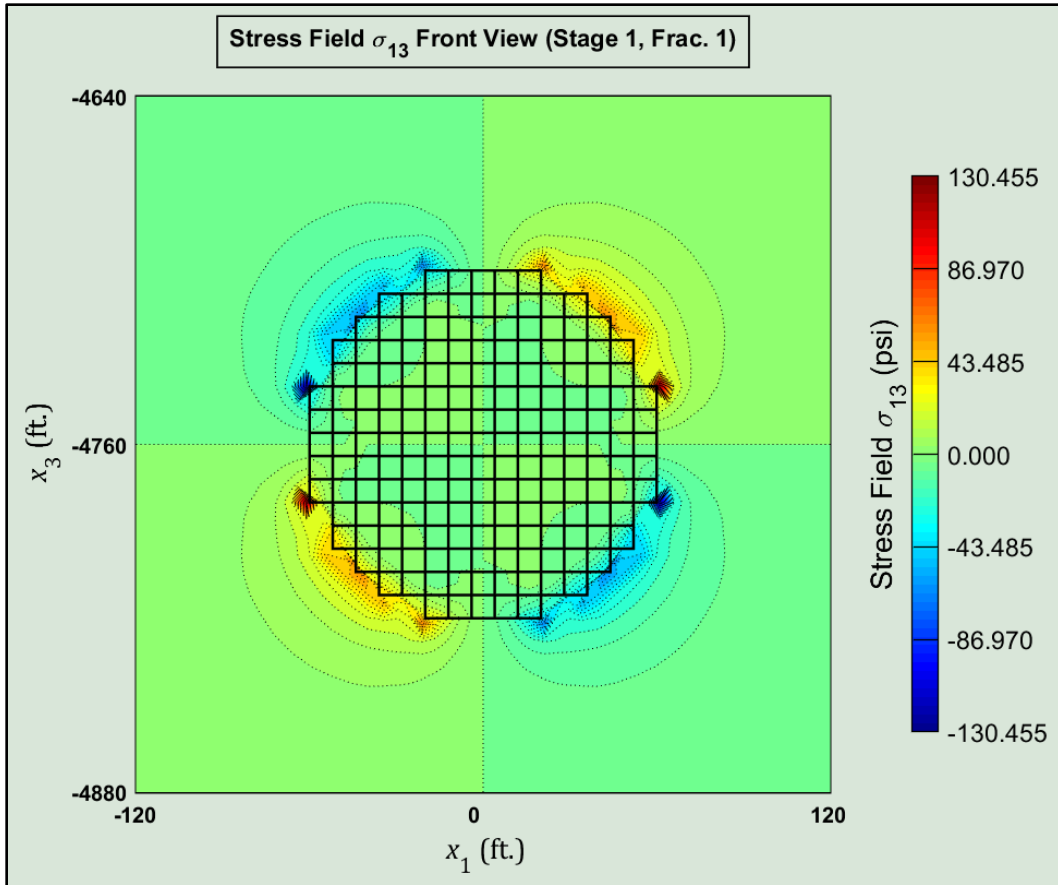


Figure B. 9—Shear Stress Fields  $\sigma_{13}$  in Model Domain

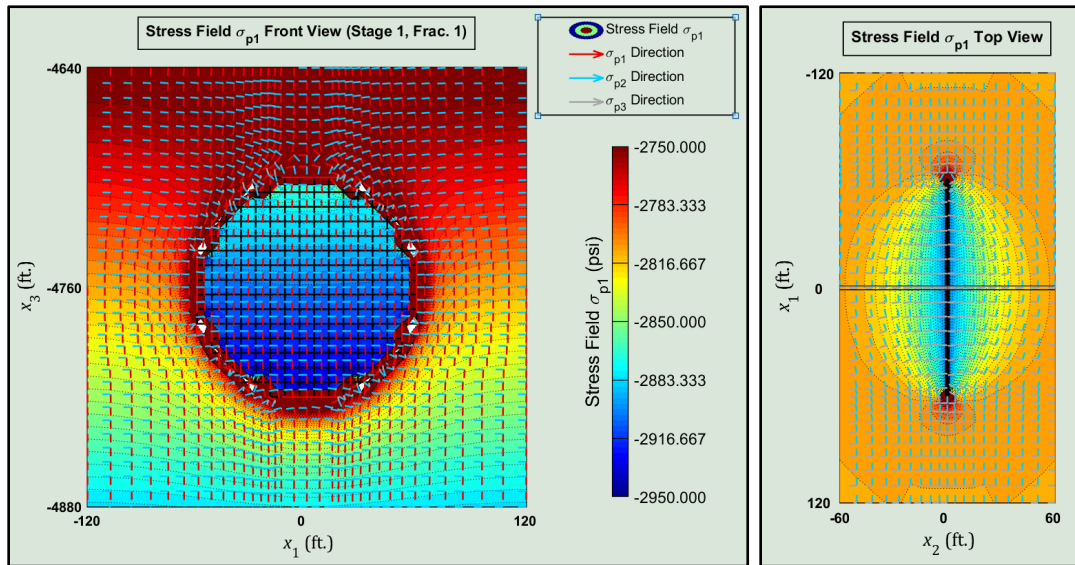


Figure B. 10—Principal Stress Field  $\sigma_{p1}$  in Model Domain

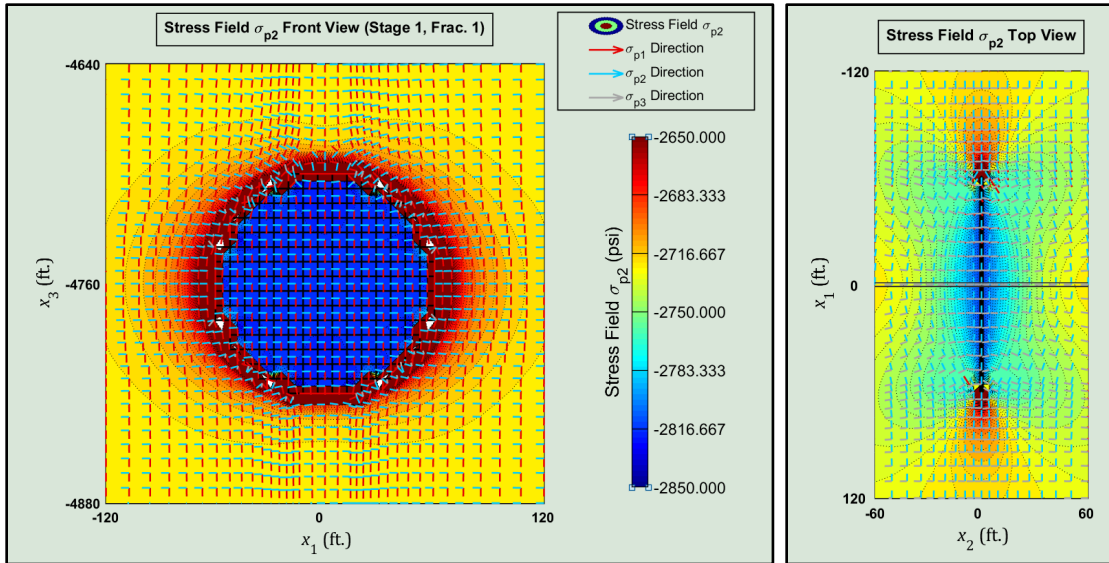


Figure B. 11—Principal Stress Field  $\sigma_{p2}$  in Model Domain

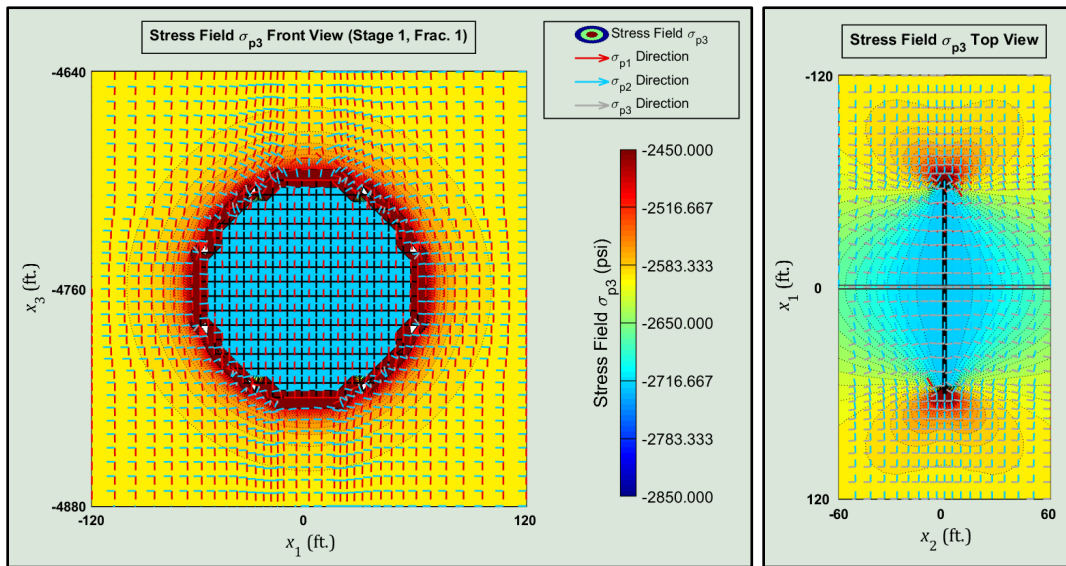


Figure B. 12—Principal Stress Field  $\sigma_{p3}$  in Model Domain



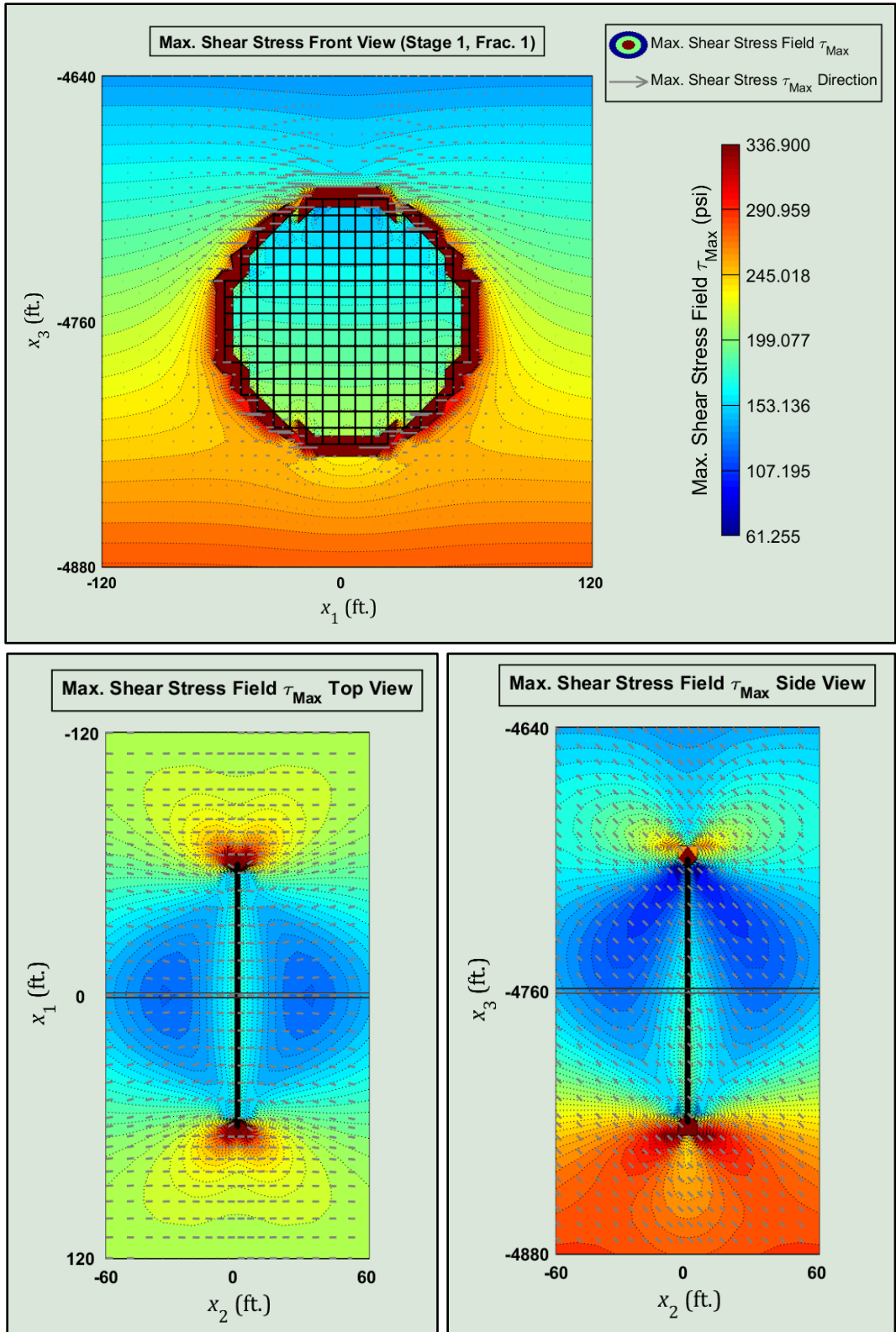


Figure B. 13—Maximum Shearing Stress Field  $\tau_{Max}$  in Model Domain and Its Orientation

It needs to be mentioned that, in Figure B. 5, Figure B. 6, and Figure B. 7, which illustrate stress field components  $\sigma_{11}$ ,  $\sigma_{22}$ , and  $\sigma_{33}$  respectively, some grid-nodes are selected either at fracture face or well further from it for verification purposes. For instance,  $\sigma_{11}$  in Figure B. 5 which is aligned with maximum in-situ stress, the value well matches with it. Or take a look at Figure B. 6 to see stress field component,  $\sigma_{22}$ . The value at fracture face is exactly equal to fluid injection pressure; however, the other grid-node outside of fracture is in a great match with minimum in-situ stress in Table B. 1. In addition, all the principal stress vectors have, also, been illustrated in Figure B. 10 to Figure B. 12. They are all the same for these figures. However, the contour is different and corresponds to labels mentioned on top of them. Some of the general information is given about the model simulation in Table B. 2.

Table B. 2— General Information About a Single-Fracture Model

<b>Parameter or Property</b>	<b>Value</b>
Total No. of RABEs	177
Total No. of Grid Nodes	24'500
Total No. of Degrees of Freedom	531
Dislocation Analysis Time in Stage 1 ( <b>KU = ΔP</b> )	0.199 min.
DDDv Analysis Time (Okada's Formulation)	0.501 min.
Strain/Stress Analysis in Stage 1	0.002 min.
Total Analysis Time	0.528 min.

## B.9. An Example of a Multiple Hydraulic Fractures in Two Separate Stages

If fractures are far apart their interactions need not be considered. But often fractures do interact, for example in a hydraulic fracture stage. Currently, according to Figure B. 14, Stage 1 and Stage 2 can be simulated sequentially because of no interactions between them. However, it cannot simulate Stage 1 and Stage 3 sequentially, because they are so close and might interact to each other. For the case of zipper-frac, fractures in Stage 1 and stage 2, have to be outside of stress-shadow margin to be simulated perfectly. If fractures are within stress-shadow, our simulation might not be accurate enough.

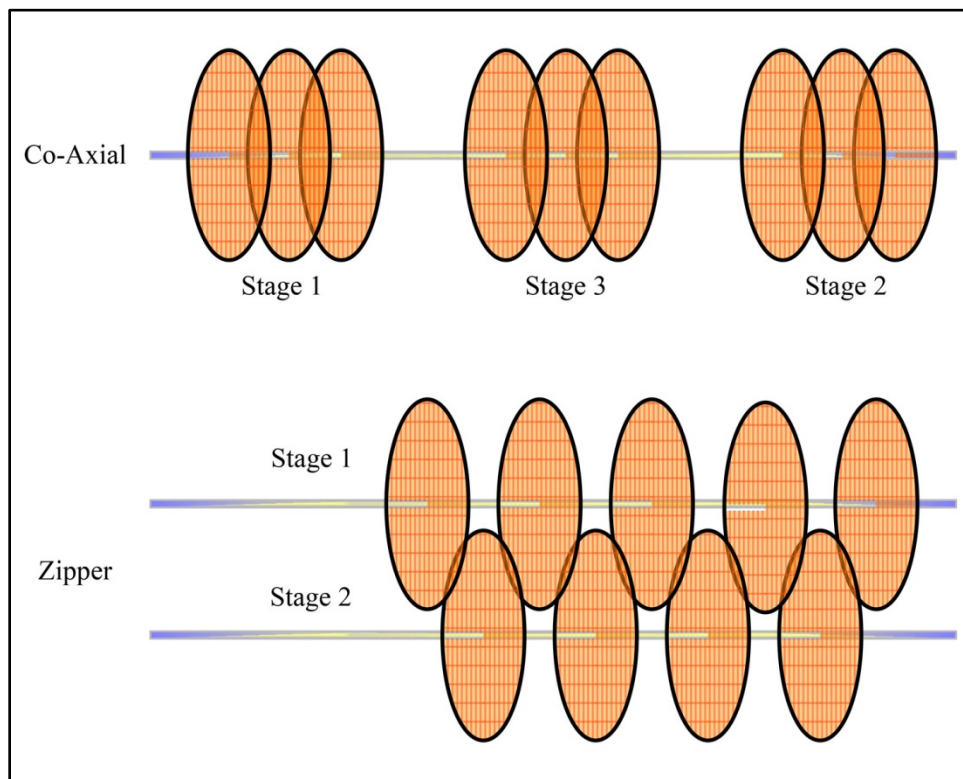


Figure B. 14—A Schematic to Two Types of Hydraulic Fracture Configurations.

Now, we are going to simulate a two-stage multi-fracture project to show the capabilities of our simulator. Fractures are assumed to be rectangular. Initial data to define the model are based on Table B. 3.

Table B. 3— Initial Values and Properties for a Two-Stage Multi-HF Model

Parameter or Property	Value	Unit
Elastic Modulus	$E = 0.3404 \times 10^6$	psi
Poisson's Ratio	$\nu = 0.26$	Unitless
Min. Hor. In-Situ Stress	$S_{\min}^H = -2600$	psi
Max. Hor. In-Situ Stress	$S_{\max}^H = -2725$	psi
Average Specific Density of Rock	$\gamma = 85$	pcf
Depth of Injection Point	$D = 4760$	ft.
Half-Lengths of HFs in Stage 1	$hfL_x \times hfL_y = 60 \times 15$	ft. $\times$ ft.
RABE Mesh Size in Stage 1	$17 \times 5$	
Frac. Spacing in Stage 1	$s = 20$	ft.
Number of HFs in Stage 1	$n = 4$	
Half-Lengths of HFs in Stage 2	$hfL_x \times hfL_y = 70 \times 17$	ft. $\times$ ft.
RABE Mesh Size in Stage 2	$19 \times 7$	
Frac. Spacing in Stage 2	$s = 25$	ft.
Number of HFs in Stage 2	$n = 3$	
Distance Between Stages	65	ft.
Extent of the Model Domain	$280 \times 315 \times 80$	ft.
Fracture Orientation	Vertical ( $\delta = 90^\circ$ )	
No. of Grid Spacing Outside Fracs.	9	
Injection Pressure at Depth in Stage 1	2720 ( $\Delta p = 120$ )	psi
Injection Pressure at Depth in Stage 2	2735 ( $\Delta p = 135$ )	psi

Figure B. 15 and Figure B. 16 both illustrate the geometry of the model after fluid injection. Top and left figures in abovementioned figures show the geometry based on

dislocation components obtained by analysis of system of equilibrium equations. In addition, bottom and right figures show deformed shape of the fractures by applying displacement field components near boundary element faces. Because of interaction between fractures in each stage, the results are different. Moreover, middle fractures have less apertures than those of side fractures. Some researchers have addressed this phenomenon in literatures (Abbas et al. 2014). It is obvious that deformed shape based on displacement field components is more accurate and applying analyzed dislocations to boundary elements is not a good idea.

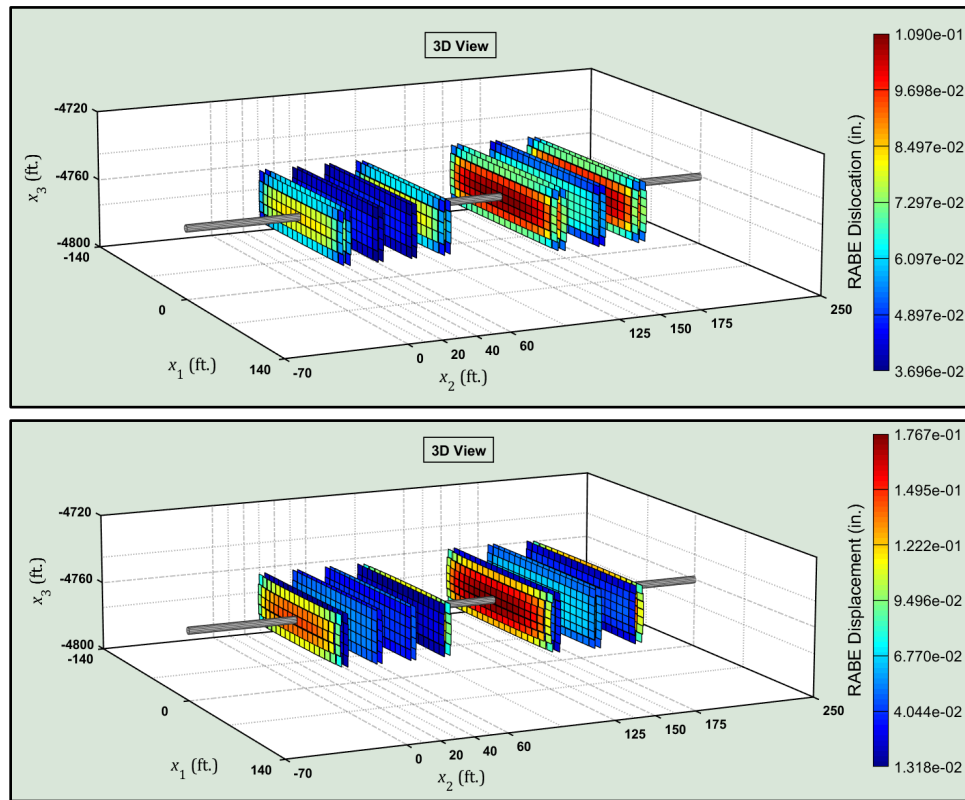


Figure B. 15— 3D View Geometry of Two-Stage Multi-Fracture Problem After Fluid Injection. Top Figure is Based on BE Dislocations. Bottom Figure is Based on Displacement Field Near BE Faces.

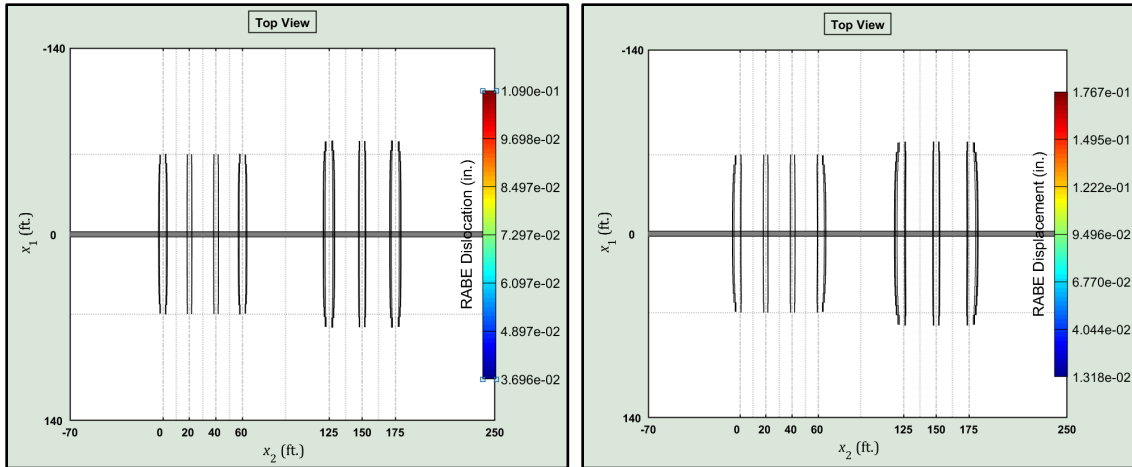


Figure B. 16— Top View Geometry of Two-Stage Multi-Fracture Problem After Fluid Injection. Left Figure is Based on BE Dislocations. Right Figure is Based on Displacement Field Near BE Faces.

Now that there are interactions between fractures in each stage, it is better to investigate mid-planes of the fractures after fluid injection.

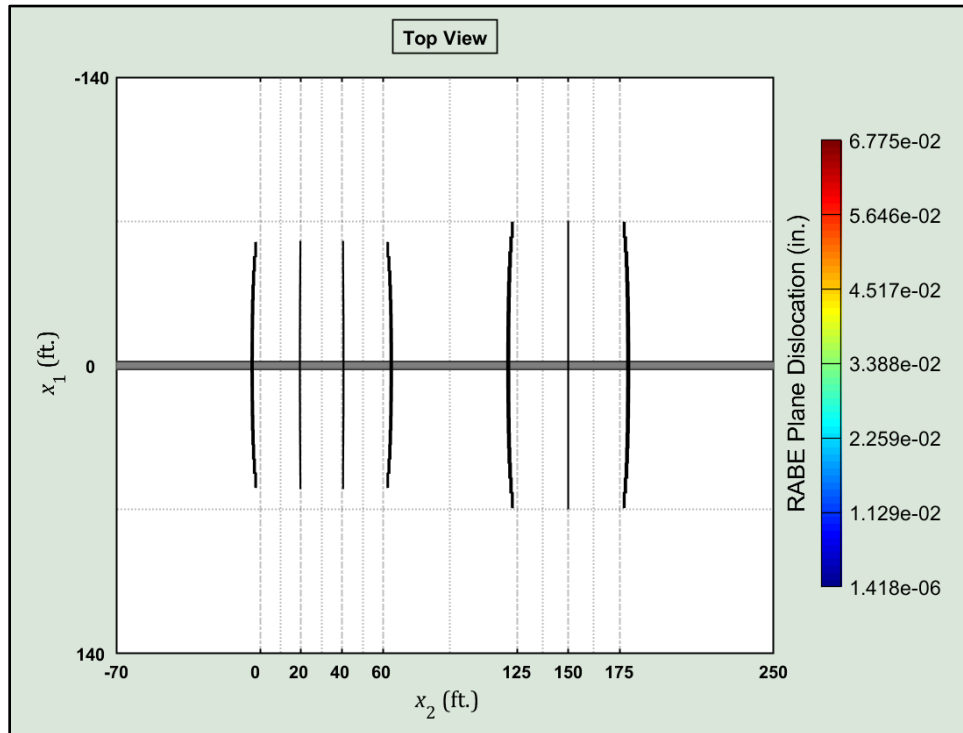


Figure B. 17—Mid-Planes of fractures after Deformation

As it is seen in Figure B. 17, mid-planes of the fractures have been deviated from straight surface prior to pressurization. For relatively long fractures, frac hit is likely. These two issues, may have negative impact on productivity of fractured wells (King et al. 2017; Rainbolt and Esco 2018).

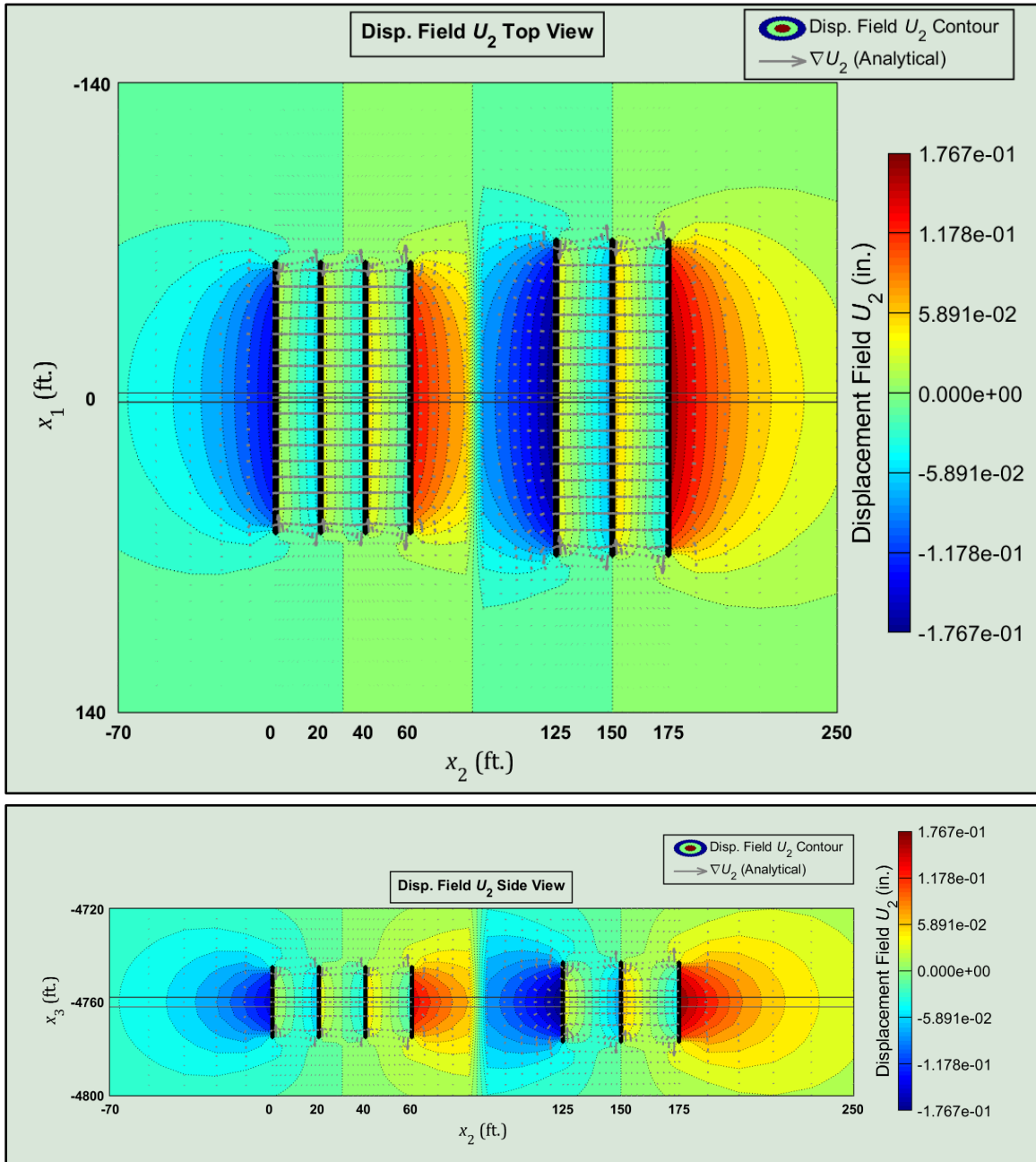


Figure B. 18—Displacement Field  $u_2$  and its gradient

Like the case of single fracture problem in section B.8, we illustrate displacement field and its gradient for better understanding of the state of displacement. Here, we just show displacement component  $u_2$  which can be found in Figure B. 18. Stress components  $\sigma_{11}$ , and  $\sigma_{22}$  are illustrated in Figure B. 19. The values shown in sample grid-nodes at or outside fracture faces are in perfect match with in-situ stress and injection pressure values mentioned in Table B. 3.

And finally, state of principal stresses and maximum shearing stress including their corresponding orientations are depicted in Figure B. 20 and Figure B. 21.

As a result, in this specific problem, it is clear that maximum shearing stress below hydraulic fracture zone is high due to increasing overburden stress. Therefore, existence of natural fractures is more likely below fractures than other zones.

Now that the analysis and simulation is complete, it is a good idea to take a look at general information in Table B. 4. Total number of degrees of freedom in this model is 2'217 and the analysis took about 5.748 min. Total number of grid-nodes is 57'798. If we were to simulate the same problem with FEM or any similar method, it would have about 173'400 degrees of freedom.



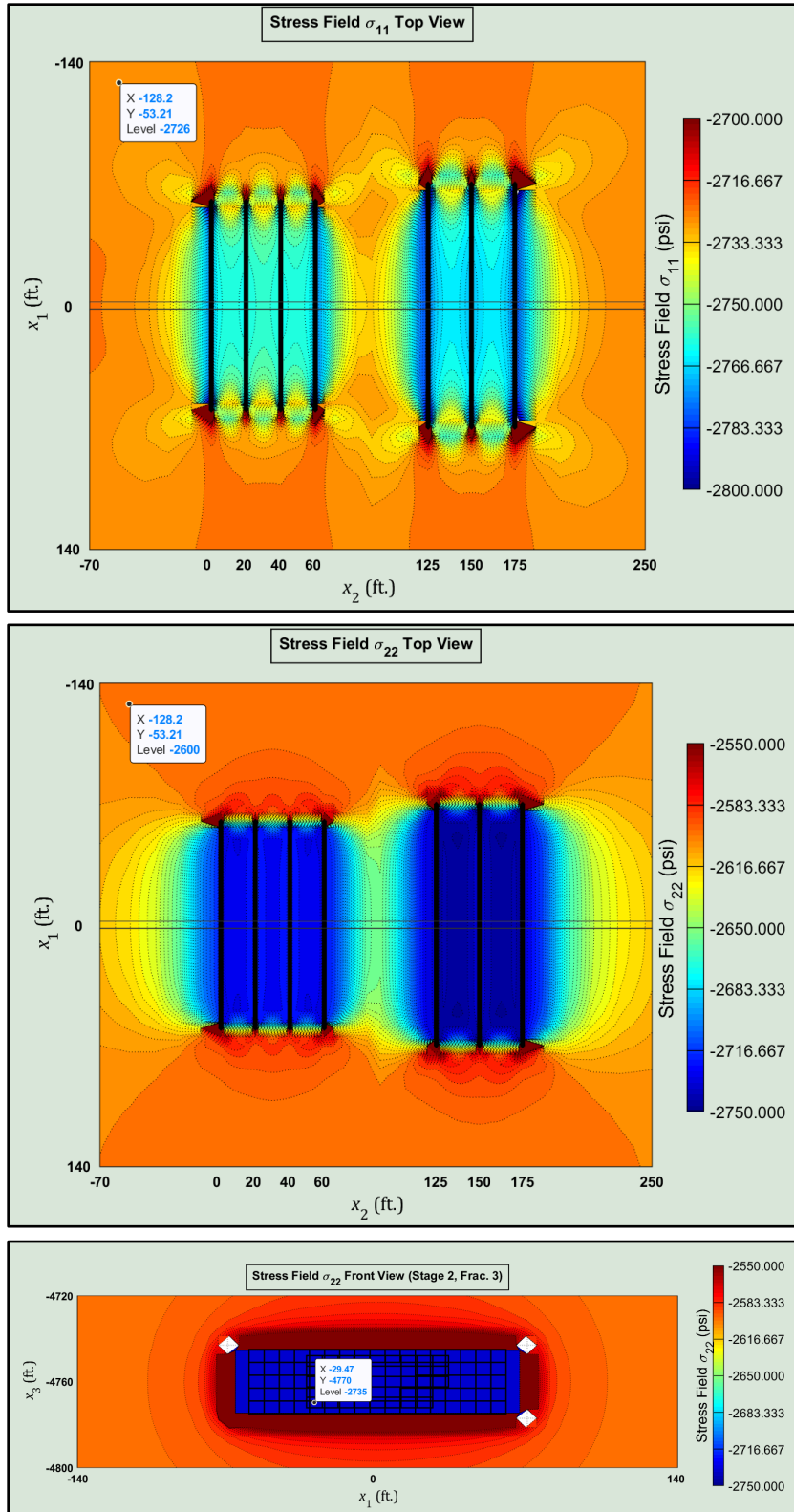


Figure B. 19—Stress Field Components  $\sigma_{11}$ , and  $\sigma_{22}$ . Sample grid-nodes are selected for verification purposes.

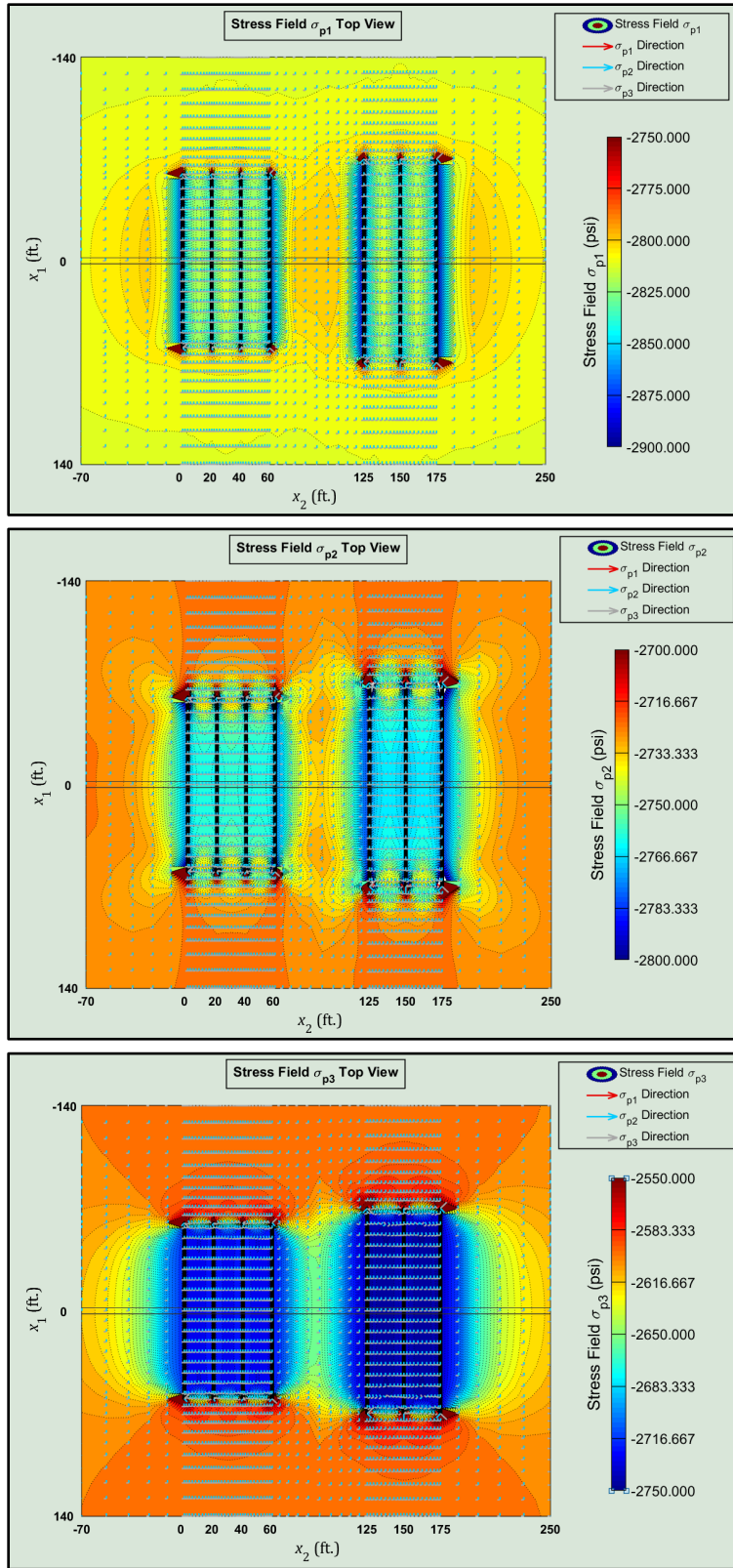


Figure B. 20—Principal Stress Components and Their Corresponding Vectors Around Fractures.

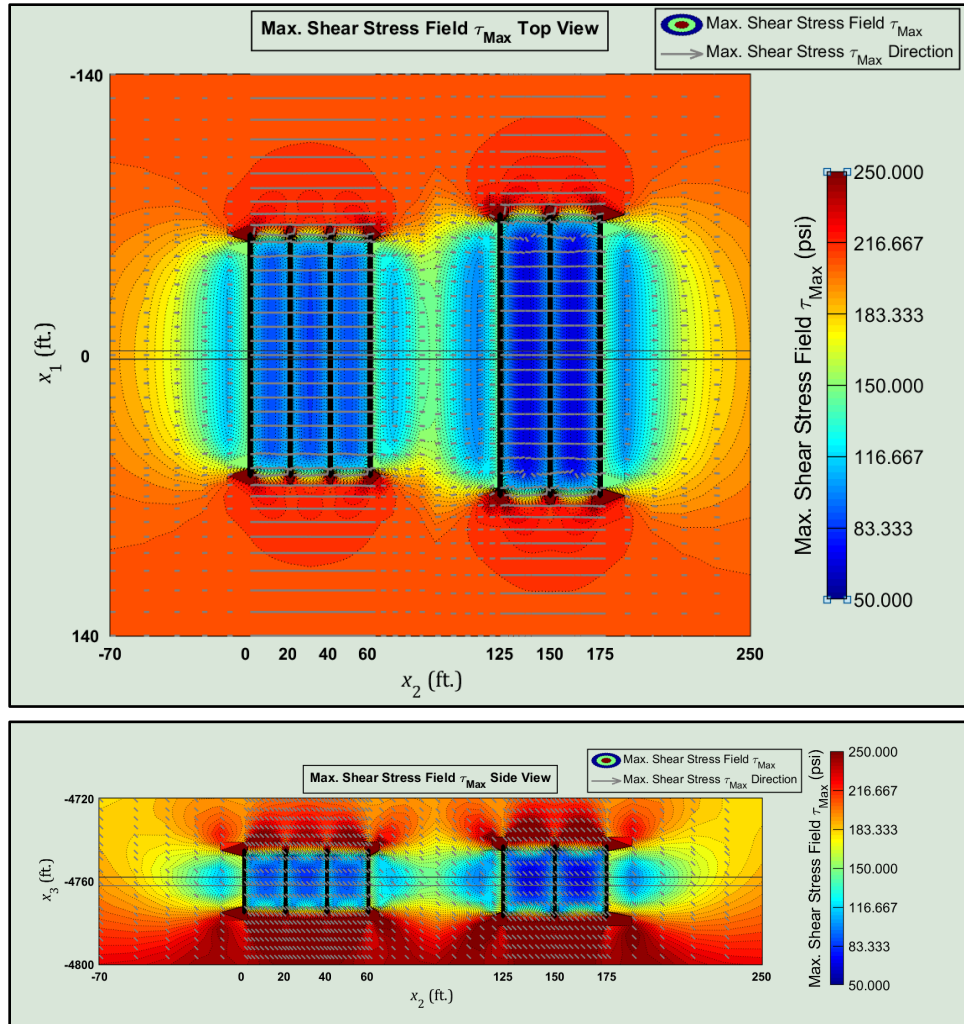


Figure B. 21—Maximum Shearing Stress Field and Its Orientation.

Therefore, a system of 173'400 equilibrium equations must be solved to obtain all unknowns. Dealing with that system would require us to use supercomputers. Without using supercomputers, the solution could take days or even weeks by regular PCs or laptops. But in our method, we just need to deal with a system of 2'217 equilibrium equations. Our proposed method can save a lot of time and money. We will verify and validate our model in next chapter. During verification and validation, the accuracy of our methods will be cleared.

Table B. 4— General Information About a Two-Stage Multi-Fracture Model

<b>Parameter or Property</b>	<b>Value</b>
Total No. of RABEs	739
Total No. of Grid Nodes	57'798
Total No. of Degrees of Freedom in Stage 1	1'020
Dislocation Analysis Time in Stage 1 ( $\mathbf{KU} = \Delta\mathbf{P}$ )	0.766 min.
DDDv Analysis Time (Okada's Formulation)	3.033 min.
Strain/Stress Analysis in Stage 1	$\approx 0.000$ min.
Total No. of Degrees of Freedom in Stage 2	1197
Dislocation Analysis Time in Stage 2( $\mathbf{KU} = \Delta\mathbf{P}$ )	0.121 min.
DDDv Analysis Time (Okada's Formulation)	2.248 min.
Strain/Stress Analysis in Stage 2	$\approx 0.000$ min.
Total No. of Degrees of Freedom in the Model	2'217
Dislocation Analysis Time in the Model ( $\mathbf{KU} = \Delta\mathbf{P}$ )	0.197 min.
DDDv Analysis Time (Okada's Formulation)	5.508 min.
Strain/Stress Analysis in the Model	$\approx 0.000$ min.
Total Analysis Time	5.748 min.